HIGH TEMPERATURE GASEOUS DESULFURIZATION USING CERIUM OXIDES AND BASTNAESITE CONCENTRATES

By

VALERIE VERONICA MARIE MENG, B.Sc.

A Thesis

Submitted to the Faculty of Graduate Studies

in Partial Fulfillment of the Requirements

for the Degree

Doctor of Philosophy

McMaster University

DESULFURIZATION USING CERIUM OXIDES AND BASTNAESITE CONCENTRATES

DOCTOR OF PHILOSOPHY (1985)
(Chemical Engineering)

McMaster University
Hamilton, Ontario

TITLE: High Temperature Gaseous Desulfurization Using Cerium Oxides and Bastnaesite Concentrates

AUTHOR: Valerie Veronica Marie Meng, B.Sc. (McMaster University)

SUPERVISOR: Professor D.A.R. Kay

NUMBER of PAGES: xviii, 198

ABSTRACT

The high temperature gaseous desulphurization characteristics of calcined bastnaesite concentrates and cerium oxides have been investigated. The former is a solid solution of rare earth oxyfluorides (RE = La, Nd, Pr) and CeO_2, and has a fluorite type structure. The presence of dissolved CeO_2 in these concentrates is believed to be responsible for the reduction, desulfurization and regeneration characteristics of this mineral.

The chemistry of the desulfurization and regeneration process has been elucidated using a fixed bed of cerium oxide at high temperatures (800-1000°C). Coal gases, similar in composition to those generated by a Koppers-Totzek gasification unit, were desulfurized from 1.0% H_2S by volume to less than 4 ng S/mL (3 ppm) in a laboratory scale reactor. This represents a desulfurization efficiency of 99.98%. Desulfurization takes place through a non-catalytic gas-solid reaction where the reactant is in the form of a non-stoichiometric oxide, CeO_{2-x}.

$$2\,CeO_{2-x}(s) + H_2S(g) + (1-2x)H_2(g) = Ce_2O_2S(s) + 2(1-x)H_2O(g)$$

Adsorption of sulfur is facilitated by the presence of oxygen vacancies in the reduced sorbents. An interactive computing system was used in conjunction with the Ce-O-S phase stability diagram to predict the compositions of reactants and products in terms of the sulfur and oxygen potentials of the gas phase.

Regeneration of spent sorbents occurs readily in air, with the evolution of sulfur dioxide:

$$Ce_2O_2S(s) + O_2(g) = 2\,CeO_2(s) + SO_2(g)$$

Desulfurization efficiencies of cerium oxides compared favourably with those of similar high temperature technologies using iron oxide, limestone or dolomite.

ACKNOWLEDGEMENTS

The author wishes to express her sincere gratitude to those who have contributed, in various ways, to the work embodied in this thesis. She is particularly indebted to:

Her research director, Dr. D.A.R. Kay, for his suggestions, guidance and encouragement throughout this project. His support and understanding through a difficult period near the completion of this thesis were invaluable.

Her family, for encouraging her to pursue graduate studies.

Ralph Harris, for his patience and constant encouragement throughout the preparation of this manuscript.

Ute Smith, Karen Hagel, Lynne Thomas and Frank Gibbs, for their assistance with this project.

Dominica Misale for proof reading and assisting with this manuscript.

The Engineering Word Processing Centre, for typing the manuscript.

Her student counsellors, Pauline and Bill, for their helpful discussions.

McMaster University, for financial assistance.

Prasad Apte and Eldorado Resources, for the use of their facilities for part of the work embodied in this thesis.

TABLE OF CONTENTS

TABLE OF CONTENTS (continued)

TABLE OF CONTENTS (continued)

APPENDICES

LIST OF FIGURES

LIST OF FIGURES (continued)

LIST OF FIGURES (continued)

LIST OF TABLES

LIST OF TABLES (continued)

LIST OF TABLES (continued)

NOMENCLATURE

A_g	external surface area of the grain
A_p	external surface area of the pellet
C	outlet concentration of H_2S
C_i	initial concentration of H_2S in the EDF
C_o	inlet concentration of H_2S
C_A	concentration of gaseous species, A
D_e	effective diffusivity
D_f	molecular diffusivity
d_p	particle diameter
E_a	activation energy
F_g	shape factor for the grain
F_p	shape factor for the pellet
k	modified rate constant = $k[A_g/F_g V_g](1-\varepsilon_p)$
k	intrinsic kinetic rate constant
k_f, k_m	external mass transfer coefficients
K_T	equilibrium constant at absolute temperature T
p_i	partial pressure of component i in atm.
P	absolute pressure
Q	volumetric flow rate
R	radial coordinate of pellet
R_p	radius of pellet
R_A	rate of reaction of species A (Chapter 4)
r_c	radius to the reaction interface in grain
r_g	radius of grain

NOMENCLATURE (continued)

t	time
t^*	dimensionless time
T	Temperature (K or °C)
v, v_0	superficial velocity
$\hat{V}$	molar volume of solid
V_g	volume of grain
V_p	volume of pellet
X_s	solid conversion
x	deviation from stoichiometry in CeO_{2-x} or Ce_2O_{3+x}, 2 or 3 in SO_x
y	distance of bed from reactor inlet
y^*	dimensionless length of fixed bed from reactor inlet
y_b	total bed length
$\Delta G°$	standard free energy change
$\Delta S°$	standard entropy change
$\Delta H°$	standard enthalpy change
β	effectiveness factor
ε_p	porosity
ε_v	bed void fraction
η	length coordinate $A_p R/F_p V_p$ (Appendix 13)
$\bar{\eta}$	maximum conversion (Appendix 6)
θ	C/C_0 dimensionless concentration
κ	$k/\bar{k}$ dimensionless rate constant which is a function of position in the bed
ξ	dimensionless position of reaction front in the grain
ρ_s	$\rho'_s(1-\varepsilon_p)$ molar density, including internal void fraction

NOMENCLATURE (continued)

ρ'_s	true molar density of the solid reactant
$\hat{\sigma}$	reaction modulus
τ	throughput parameter
ψ	C_A/C_{A_0} dimensionless concentration within pellet

Abbreviations

CCM	Crackling Core Model
CVM	Changing Voidage Model
DTA	Differential Thermal Analysis
EDAX	energy dispersive X-ray Analysis
EDF	exponential dilution flask
F*A*C*T	Facility for the Analysis of Chemical Thermodynamics
FGD	flue gas desulfurization
FPD	Flame photometric detector
g.c.	gas chromatograph
GPM	Grainy Pellet Model
GHVS	Gas Hourly Space Velocity
K-T	Koppers-Totzek Coal Gasifier
Pe	Peclet number
RE	Used as an abbreviation for a lanthanide or Rare Earth Element
SNG	Synthetic natural gas
SCM	Shrinking Core Model
SEM	Scanning electron microscopy
Sh	Sherwood number
TDM	Thermal Decomposition Model

NOMENCLATURE (continued)

TGA	Thermogravimetric Analysis
UCM	Uniform Conversion Model

Chapter I

INTRODUCTION

If coal is to find widespread use as an alternative energy source to oil and gas, adequate methods of controlling sulfur emissions must be developed. Most existing and proposed gasification plants use low temperature acid gas removal processes ($<300°C$). High temperature processes utilizing iron oxides, dolomite or molten metals yield higher energy efficiencies but are only in the early stages of development (1).

Although the use of rare earth oxides for gaseous desulfurization has been patented (2-8), the chemistry, chemical thermodynamics and reaction kinetics are not well understood, making process control and optimization difficult. Studies of liquid iron desulfurization by Ghosh and Kay (9), using rare earth oxides and bastnaesite concentrates, indicated that similar principles may be applicable to the desulfurization of hot gases. Subsequent work by Kay (10,11), using bastnaesite concentrates for the desulfurization of a simulated coal gas, typical of a Koppers-Totzek coal gasifier, confirmed the viability of the latter application. However, the desulfurization and regeneration processes required further investigation.

The complete research program, diagrammatically represented in Figure 1.1, involves the investigation of the chemistry and thermodynamics of the various rare earth compounds associated with hot gaseous desulfurization. This information, often inadequate or simply unavailable, is usually the most important in determining plant operation and economics. The problem is one of describing the chemical reactions taking place both with respect to the mechanism and kinetic rate constants. Experimental data, essential to the interpretation of the desulfurization and regeneration behaviour of rare earth oxides and

bastnaesite concentrates, and generated concurrently with the present investigation by other investigators, are summarized in Table 1.1.

Table 1.1: Summary of work of other investigators used in the interpretation of this work

Investigator	Type of work
C. Hagopian	T.G.A. and microscopic analysis of sintered, reduced, desulfurized and regenerated pellets of bastnaesite concentrates 4000 C and 4100 (12).
V. Scepanovic D.A.R. Kay	Pelletization, determination of sintering conditions, and preliminary desulfurization studies (13).
G.F. Giacomelli	Kinetics of the reaction of steam with bastnaesite concentrates 4000 C and 4100 were studied (14).
Y. Hong	Free energies of formation of various rare earth oxyfluorides were determined by solid electrolyte cells (15).
R. Dwivedi	The La-O-S phase stability diagram and the partial Ce-O-S phase stability diagram were determined and positions of boundaries were verified (16).

Data generated using a fixed bed reactor containing cerium oxides were used to propose the most efficient way of proceeding with a pilot scale desulfurization unit.

1.1 Objectives

The objectives of this thesis were as follows:

(i) Completion of the thermodynamic phase stability diagram for the Ce-O-S system in the temperature range 800-1000°C from available thermodynamic data in the literature.

(ii) Confirmation of the thermodynamically predicted chemical reactions during desulfurization and regeneration, by chemical analysis of the gaseous and solid products of reaction.

(iii) Determination of the qualitative effects of particle size, gas flow rate, temperature and initial gas composition for a cerium oxide sorbent and to propose a chemical reaction mechanism.

(iv) Determination of the conditions for the regeneration of the spent cerium oxide sorbent.

(v) Consolidation of the scientific data generated in this work for the Ce-O-S system, with data generated by other investigators, to provide a technological base in the use of bastnäesite concentrates in hot gaseous desulfurization.

In order to attain these objectives, desulfurization was studied in a packed bed integral reactor containing cerium oxide for the range of operating conditions given in Table 1.2.

Table 1.2: Table of Operating Conditions for Fixed Bed Reactor

Temperature (K) 1073 - 1296

Mean particle size (mm) +0.210/-0.297 to +0.595/-0.841

Superficial linear gas velocity (cm/s) 0.47 - 3.51

Inlet H_2S concentration (ngS/mL) 2,000 - 13,000

The effect of these process variables on the desulfurization efficiency and sorbent capacity were analysed. Similar conditions were used to study regeneration of the spent sorbent in air and 5% hydrogen in nitrogen.

Thermogravimetric and differential thermal analytical methods were used to supplement the fixed bed studies for the verification of thermodynamic predictions.

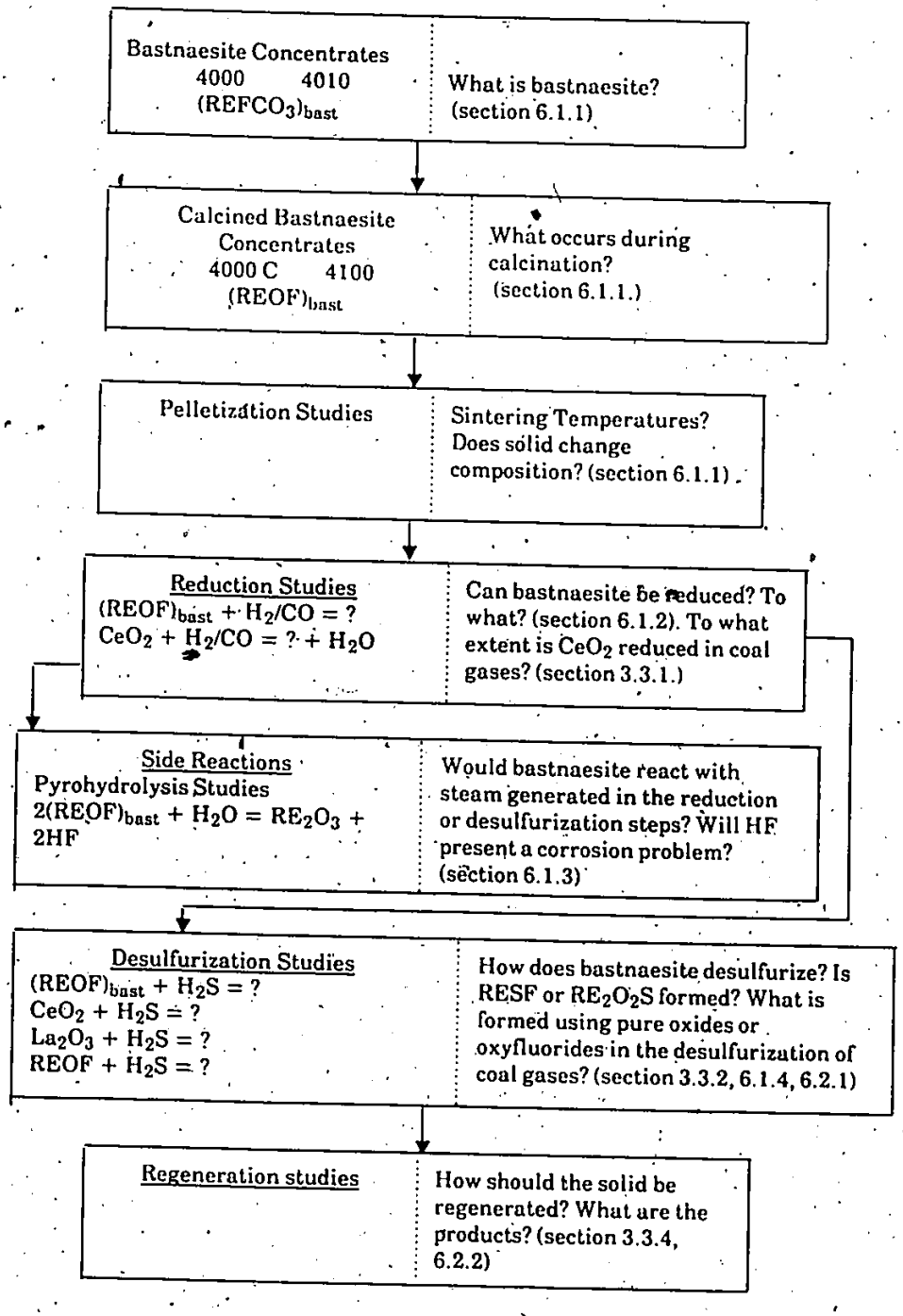

Figure 1.1: Program for the Study of the Desulfurization of Coal Gases using Bastnaesite Concentrates

Chapter II

LITERATURE REVIEW

This chapter briefly reviews coal gasification, its potential uses and the environmental impact of developing North America's coal resources using current desulfurization technology. High temperature desulfurization processes, with emphasis on those based on rare earth compounds, iron oxide and calcium oxide sorbents, are summarized. Product distributions from three established coal gasifiers (see Section 2.1) are used in Chapter III for thermodynamic predictions of desulfurization chemistry using cerium oxide sorbents at high temperatures (1073-1273 K).

2.1 Coal Gasification and Its Environmental Impact

Typical product distributions from three well established commercial gasification processes are given in Table 2.1. Historically, the Koppers-Totzek entrained gasification process has been used for the production of ammonia and other chemicals. A variety of feedstocks may be used: coal, char, coke, tar, heavy residuals and light to heavy oils. Because of high gasification temperatures, no tars, phenols or other condensible hydrocarbons are produced, thus simplifying gas purification (17).

The Lurgi fixed bed gasifier is best known for its use in the Sasol plant in South Africa in the production of feedstock for the Fischer-Tropsch synthesis. This type of gasifier is also used in the production of town gas, synthesis gases for chemicals and SNG (18).

The Winkler fluidized bed gasification process tolerates a wide variation in quality of fuel. However, it is unsuitable for low reactivity fuels or for fuels with low ash fusion temperatures. It is used for the production of ammonia, methanol and liquid hydrocarbons (18).

Table 2.1: Typical Gasification Product Distribution (19) - % by volume

	Gasifier Type		
Product	K-T	Lurgi	Winkler
CO	53.2	16.2	34.7
CO_2	10.0	30.6	19.4
H_2	34.5	42.9	41.7
H_2S+COS	1.1	0.6	0.14
CH_4	-	9.2	3.1
N_2	1.2	0.5	1.0
Exit Temperature (°C)	1000-1300	570	800-1000
Pressure (kPa)	101.3	1013-3039	101.3
Calorific Value†	11.2 MJ/m^3 (300 Btu/scf)	16.8 MJ/m^3 (450 Btu/scf)	10.2 MJ/m^3 (275 Btu/scf)
P_{O_2}†† (atm)	2.2×10^{-19}	3.2×10^{-25}	5.4×10^{-19}
P_{S_2}†† (atm)	9.1×10^{-7}	1.9×10^{-11}	9.3×10^{-9}

† For oxygen-steam-coal gasification

†† Calculated by F*A*C*T at 872°C, 101.3 kPa (K-T, Winkler) and at 570°C, 1013 kPa (Lurgi). See sections 3.2, 3.3.2 and Appendix 2.

The environmental impact of a typical gasification plant, based on current desulfurization technology as reviewed by Jahnig and Bertrand (20), is illustrated in Figure 2.1. It would take eighty of these large plants, each burning 13,600 Metric tons of coal per day

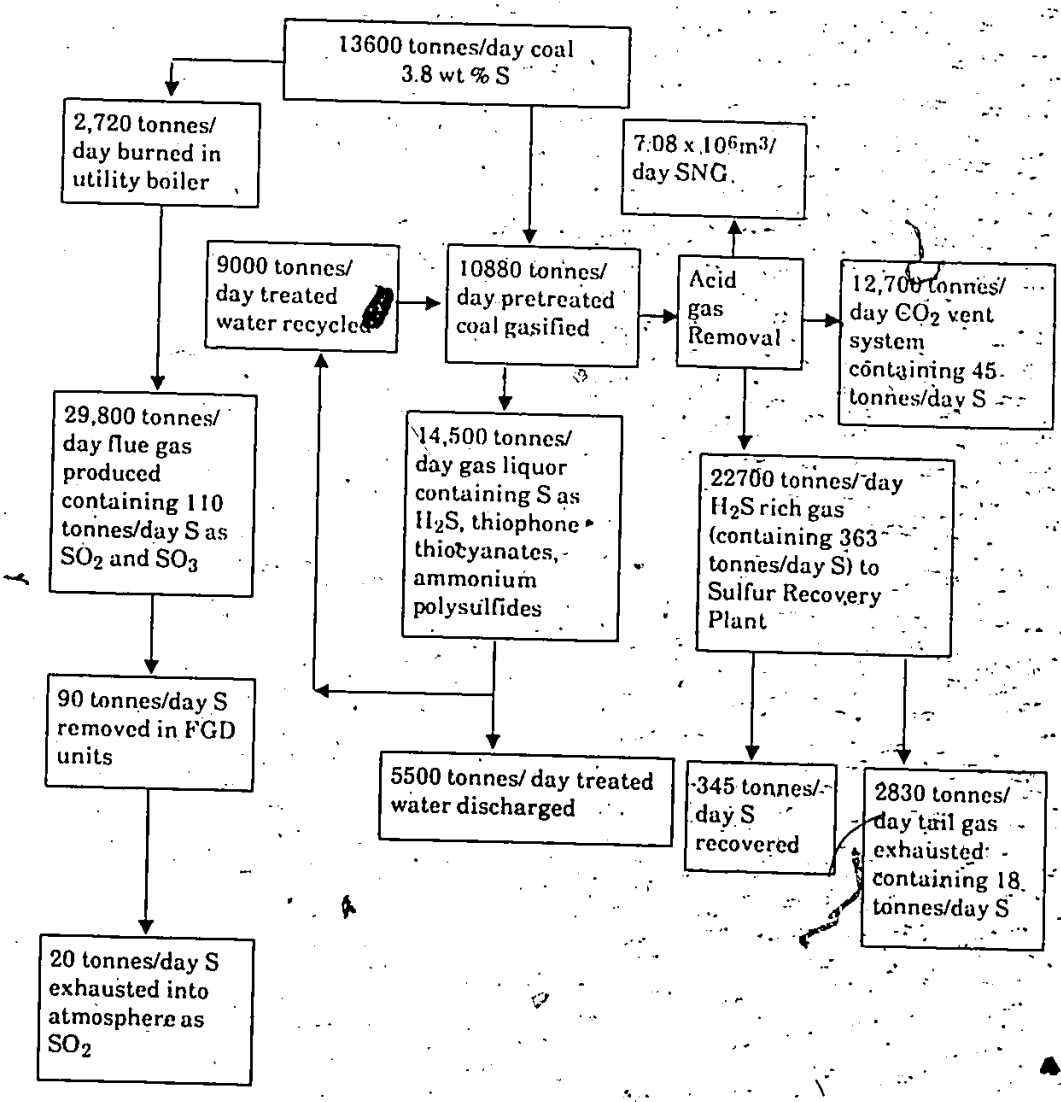

Figure 2.1: Sources of Sulfur from a Typical Gasification Plant Producing 7.08 x 10 ^{6}m^{3}/day Synthetic Natural Gas using High Quality Eastern Coal. (based on reference 20)

(15,000 tons/day), to provide fuel equivalent to 20% of the 1976 U.S. oil consumption. Projections, based on data gathered from this review, indicate that each plant releases approximately 80 metric tons per day of sulfur into the atmosphere. Sulfur compounds are present in the CO_2 vent stream, the tail gases from the sulfur plant, and the flue gases leaving the coal fired boilers.

Potential applications of low/medium grade coal gases (5.6-13.0 MJ/m^3 or 150-350 Btu/scf), as recently reviewed by Timmins (21), are summarized in Table 2.2. Because of low world prices for natural gas, only the production of chemicals like ammonia, methanol, and gasoline have achieved commercial viability. About 30% of world ammonia production (55×10^6 Metric tons/yr) and 50% of world methanol production (30×10^6 Metric tons/yr) are made from synthesis gas. However, natural gas steam reforming is still the major route (21). Many of these chemical works contain their own boiler facility and power plant fired on natural gas. Coal gases may be used as alternative fuels in high temperature gas turbines of combined cycle electric power generation (21,22) (See Figure 2.2). The production of SNG has been fully demonstrated on a commercial scale by the conventional Lurgi process route, although it is not yet economically viable.

In iron and steelmaking, the injection of a reducing gas (composition, temperature and pressure requirements given in Table 2.2) into the blast furnace bosh can reduce the amount of expensive metallurgical coke used by about 26%. Tuyere injection of coal gases is not economical at the present time.

2.2 High Temperature Desulfurization Processes

During gasification, the sulfur in coal is converted to H_2S, COS, CS_2, thiophenes, and mercaptans; H_2S and COS are the major components. Gas purification of the coal gas

Table 2.2: Potential Uses of Coal Gas (21,23)

1. For combined cycle power generation or as fuel for on-site steam generation.

2. In the iron and steel industry for tuyere injection of reducing gases to reduce coke rates.

   Amount of CO and H_2 should be as high as possible, i.e.
   (Percentage of component is on a molar basis)

$$\frac{\%CO_2 + \%H_2O}{\%CO_2 + \%H_2O + \%H_2 + \%CO} \times 100 < 5$$

   For injection P > 800 kPa
   T ≈ 900-1000°C

3. Production of synthetic natural gas:

$$CO(g) + 3H_2(g) = CH_4(g) + H_2O(g) \quad (1)$$ P > 101.3 kPa, 260 < T < 540°C

$$2CO(g) + 2H_2(g) = CH_4(g) + CO_2(g) \quad (2)$$

   If molar ratio $H_2/CO > 3$, reaction (1) predominates

   If molar ratio $H_2/CO < 3$, both reactions occur

4. Production of hydrogen, ammonia, methanol and liquid hydrocarbons (eg. gasoline) via Fischer-Tropsch.

$$CO(g) + 2H_2(g) = CH_3OH(\ell)$$ low-med P with Co catalyst, med P with Fe catalyst

$$nCO(g) + 2nH_2(g) = (CH_2)_n(\ell) + nH_2O(g)$$

$$2nCO(g) + nH_2(g) = (CH_2)_n(\ell) + nCO_2(g)$$

molar ratio H_2/CO = 2-8 for most Fe catalysts

$$N_2(g) + 3H_2(g) = 2NH_3(\ell)$$ T = 500°C, Fe catalyst, P = 37300 kPa

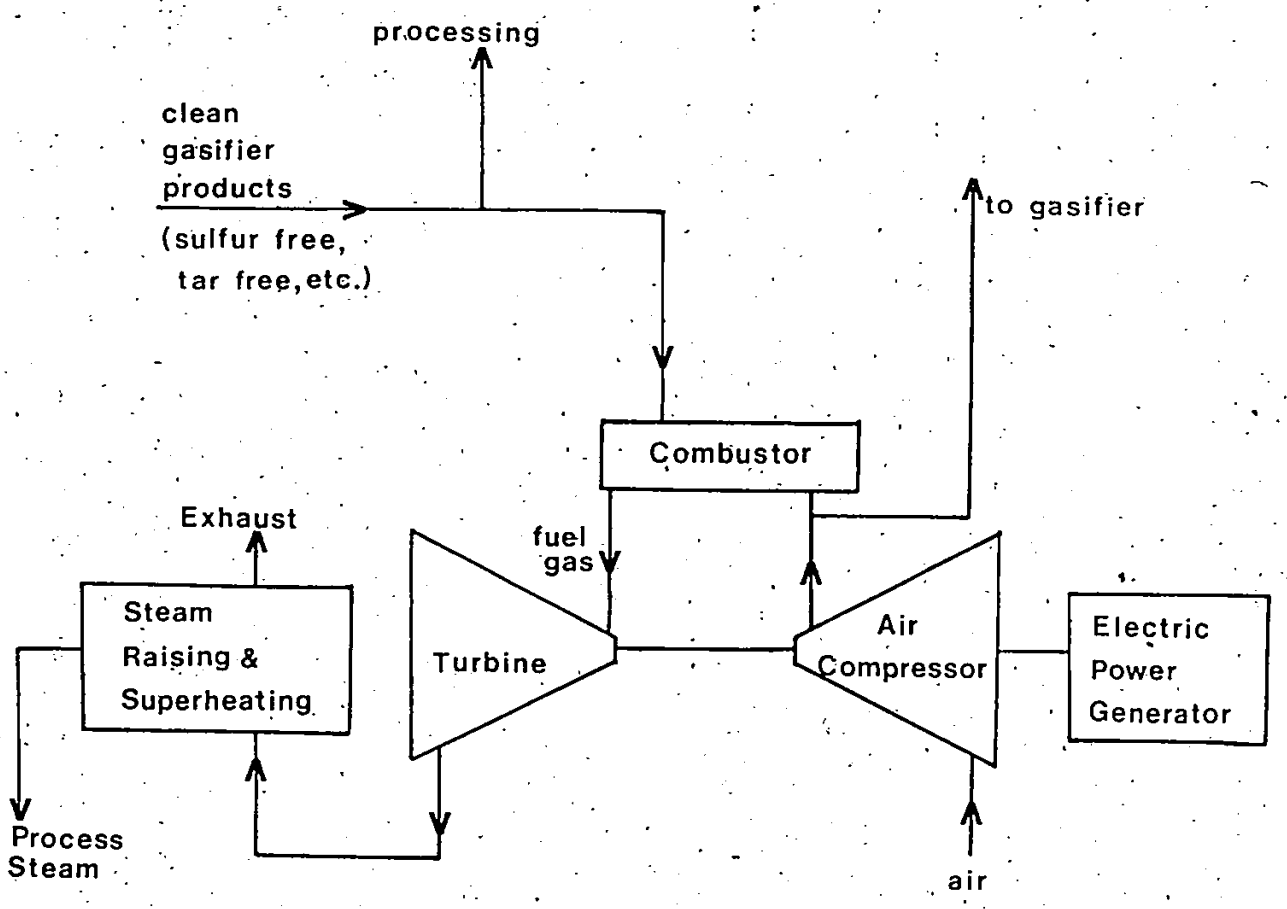

Figure 2.2: Basic Flowsheet for Combined Cycle Power Generation

may include particulate removal, gas quenching and cooling, and acid gas removal. The intended use of the synthesis gas (refer to Table 2.2) determines which of these purification steps is used (1). Synthesis gas hydrogenation catalysts are susceptible to poisoning above hydrogen sulfide levels of 0.13 ngS/mL (0.1 ppm). In boilers and power generation equipment, severe corrosion occurs if hydrogen sulfide is not removed from the coal gases prior to combustion. Owing to smaller gas volumes, H_2S is more readily removed before combustion, than from the stack of a power boiler. Clearly, for the applications discussed in section 2.1, major energy savings may be achieved if the products of coal gasification are desulfurized and subsequently used at high temperatures, thereby, avoiding the sensible heat losses associated with conventional low temperature desulfurization processes. The relative economics of coal based technology, compared to technology based on natural gas, would consequently be improved.

Most high temperature desulfurization processes are based on the reaction of certain metal oxides with hydrogen sulfide. Two examples are the Appleby-Frodingham process, using ferric oxide at 400°C, for coke oven gas desulfurization (24) and a process using zinc oxide, at 400°C for desulfurizing hydrocarbon feedstocks for ammonia synthesis (25). Work is on-going for the development of a high temperature limestone/dolomite desulfurization process (38).

Westmoreland and Harrison (27) evaluated twenty-eight metal oxides of potential interest for high temperature desulfurization of reducing gas streams. Their analysis indicated that eleven oxides (Mg, Ca, V, Fe, Co, Cu, Zn, Sr, Mo, Ba, W) satisfied the thermodynamic criteria over at least a portion of the temperature range, 360-1560°C. Cerium oxide, however, was judged unsatisfactory because it was believed that a stable unreactive oxide was formed throughout this temperature range. Lanthanum oxide was also rejected because the analysis indicated that the solid was not capable of removing 95% or greater of

the gaseous sulfur compounds. The results of thermodynamic evaluations of this type are strongly dependent upon the availability of complete and accurate thermodynamic data. Since several desulfurization processes, based on cerium and lanthanum oxides, have been developed (see section 2.2.3), critical information must have been omitted in Westmoreland's and Harrison's analysis. One of the purposes of this study is to consolidate thermodynamic data for interpreting the high temperature desulfurization behaviour of cerium oxide sorbents.

2.2.1 Iron Oxide Desulfurization Processes

Low-temperature iron oxide based processes have existed for many years. The iron sponge process (28,32) uses wood chips impregnated with 85-250 kg hydrated iron oxide per cubic meter to selectively remove H_2S at temperatures below 45°C. This process requires a relatively small investment for small to moderate gas volumes (8-10 tonnes/day S) compared with other processes. Hydrogen sulfide reacts with the sponge to form iron sulfide. Regeneration is accomplished by the continuous injection of a stream of air ($< 0.4\%$ O_2 to control the heat of reaction) into the feed gas, converting the sulfide to an oxide and liberating elemental sulfur. Alternatively, regeneration can be done periodically by passing air through the bed. Each charge of sponge can be regenerated several times but deposition of entrained oils or distillates eventually reduce adsorption capacities; replacement of the bed is eventually required. Operating temperatures above 114°C are avoided in order to prevent the loss of water of hydration, since dry iron oxides have negligible adsorption capacities for hydrogen sulfide (32).

A comprehensive review of high temperature processes, based on iron oxides, can be found in reference 29. The following discussion highlights the extensive work done by Mohan (29,30) and Schrodt (30,31), using gasifier coal ashes containing 5 to 23 wt% iron

oxides as high temperature sorbents for synthesized low heat content fuel gases. This process is limited to temperatures below 1033K to prevent thermal damage to the sorbent.

Schrodt noted that in many coals, a significant fraction of the sulfur exists in the pyrite (FeS_2) and sulfate ($FeSO_4$) forms. During gasification, the iron is converted to various oxides and removed in the gasifier ash residues, while the sulfur is converted to H_2S, COS and CS_2. The high iron oxide content of the gasifier ash residues makes them economical sources of high temperature sorbents for sulfur in fuel gases.

Figure 2.3 illustrates the Fe-O-S phase stability diagram derived by Schrodt (30). Note that oxygen partial pressures below 10^{-21} atm at 1000 K (see Figure 2.3) results in the reduction of iron oxides to the metallic form, precluding the use of these sorbents for some gas mixtures. Iron oxides in the gasifier ashes are rapidly reduced to magnetite and sometimes wüstite upon exposure to hot reducing fuel gases of composition 20% CO, 17% CO_2, 10% H_2, 3% CH_4, 49% N_2, 0.5-1.0% H_2S.

$$3\,Fe_2O_3(s) + H_2(g) = 2\,Fe_3O_4(s) + H_2O(g)\quad K_{1000} = 1.0 \times 10^5 \qquad 2.2.1.1$$

$$3\,Fe_2O_3(s) + CO(g) = 2\,Fe_3O_4(s) + CO_2(g)\quad K_{1000} = 1.1 \times 10^5 \qquad 2.2.1.2$$

$$Fe_3O_4(s) + H_2(g) = 3\,FeO(s) + H_2O(g)\quad K_{1000} = 0.34 \qquad 2.2.1.3$$

$$Fe_3O_4(s) + CO(g) = 3\,FeO(s) + CO_2(g)\quad K_{1000} = 0.63 \qquad 2.2.1.4$$

The oxygen and sulfur potentials of this gas mixture correspond to point B on the diagram and show that desulfurization leads to the formation of pyrrhotite, FeS. Large equilibrium constants favour nearly complete removal of H_2S.

$$Fe_3O_4(s) + 3\,H_2S(g) + H_2(g) = 3\,FeS(s) + 4\,H_2O(g)\quad K_{1000} = 2.67 \times 10^7 \qquad 2.2.1.5$$

$$FeO(s) + H_2S(g) = FeS(s) + H_2O(g)\quad K_{1000} = 4.21 \times 10^2 \qquad 2.2.1.6$$

Experimentally, sulfide removal efficiencies in excess of 99.0% were obtained (31).

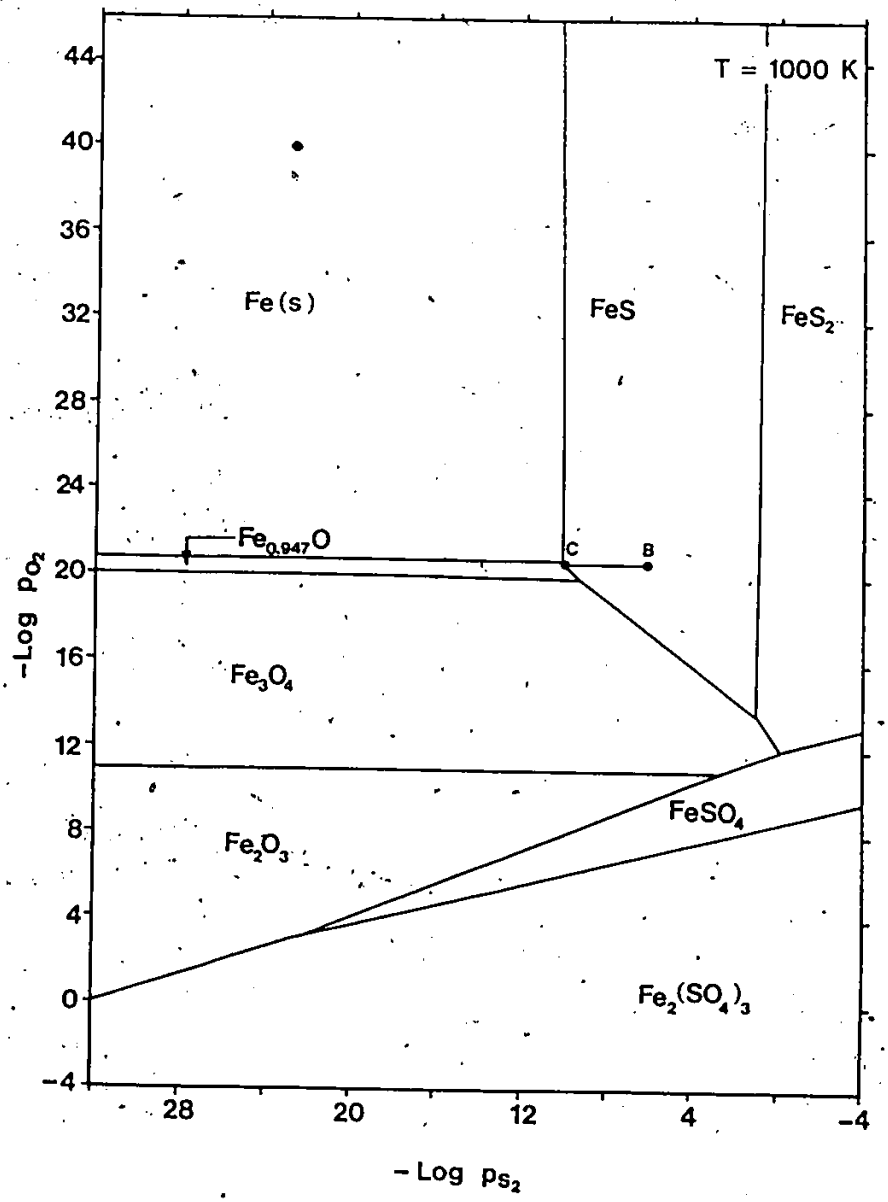

Figure 2.3: The Fe-O-S Phase Stability Diagram (30)

Regeneration of sulfided ashes was accomplished with a 3% O_2/N_2 gas mixture, releasing sulfur as SO_2. Since this reaction is highly exothermic (1.232 kJ/mol Fe_2O_3, 295 Kcal/mol), low oxygen levels are required to prevent thermal damage to the sorbents.

$$2\,FeS(s) + 7/2\,O_2(g) = Fe_2O_3 + 2\,SO_2 \quad K_{1000} = 10^{90} \qquad 2.2.1.7$$

Spent ashes (regenerated up to 20 times) indicated that cyclic use improved the ash capacity, stabilizing to a constant value of 60% Fe_2O_3 utilization beyond 10-12 cycles. Analysis of ash particles by SEM and EDAX suggested that the observed increase in adsorption capacity with cyclic use of the ash, was the result of diffusion of the iron from deep within the particle to the surface of the particle and its pores. Ash capacities and bed efficiencies were reported to increase with temperature, Fe_2O_3 content and decreasing particle size. At a constant linear velocity, the space velocity had no significiant effect on the capacity or efficiency.

Two asymptotic regimes of reaction control were proposed: a region of chemical control where Fe_3O_4 grains react in a spatially uniform way with a uniform concentration of H_2S, and a region of diffusion control where the reactant gas diffuses through interstices and reacts rapidly at a sharp solid product-reactant interface. The experimental breakthrough curves, for fixed bed studies, were reproduced using a combination of two models for each of the rate controlling regimes. For values of C/C_0 less than 0.7-0.8 the uniform conversion model was fitted to the breakthrough curve. An activation energy of $E_a = 11.48 \pm 0.13$ kJ/mol was obtained for the desulfurization reaction. The pore diffusion model was fitted to the breakthrough curve above C/C_0 values of 0.7-0.8. Diffusion coefficients, which varied with the square root of temperature (implying Knudsen diffusion control), were in the range $1.5 \times 10^{-2} - 1.5 \times 10^{-3}\ cm^2/s$.

Mohan's fluidized bed studies (29,30) using small gasifier ash particles (<0.2 mm diameter) showed no significant dependence on particle size, suggesting chemical reaction control. An activation energy of 45.53 kJ/mol was obtained using the uniform conversion

model. Mohan (29) explained that the lower numerical value of activation energy obtained in fixed bed studies was due to the difficulty in uncoupling the associated transport processes from the chemical phenomena. For example, chemically controlled gas-solid reaction systems show intrinsic activation energies greater than 33.5 kJ/mol. Intraparticle and gas film diffusional resistance controlled reactions, on the other hand, have typical values of apparent activation energies of 6 and 2 kJ/mol respectively. The E_a value of 45.53 kJ/mol obtained in fluidized bed studies suggested chemical reaction control; whereas, the E_a value of 11.48 kJ/mol reported for the fixed bed studies suggested mixed control (kinetic and diffusional).

2.2.2 Limestone or Dolomite Desulfurization Processes

The widespread availability and low cost of limestone and dolomite underlie their consideration as sorbents in processes for SO_2 or H_2S removal from hot gases. The use of calcium-based sorbents under oxidizing and reducing conditions were summarized by O'Neill and Keairns (33) (see Table 2.3). Contact between the solid and gas were attained either by the injection of finely powdered limestone into the boiler combustion chamber, or by passing flue gases through a fluidized bed of limestone, or by burning fuel in such a bed.

Table 2.3:

Calcium based Sorbent Processes as Summarized by O'Neil and Keairns (33).

	Products Desulfurized	Pressure (kPa)	Temperature (°C)	Reaction	Equilibrium H_2S or SO_2 (ngS/mL)
(1)	Fluidized-bed combustion	101.3	705-900	$CaO + SO_2 + \frac{1}{2} O_2 = CaSO_4$	0.026 (870°C)
(2)	Fluidized-bed combustion	101.3	730-950	$CaCO_3 + SO_2 + \frac{1}{2} O_2 = CaSO_4 + CO_2$	0.0143 (870°C)
(3)	Fluidized-bed low Btu coal gasification	1013-1520	870-925	$CaCO_3 + H_2S = CaS + H_2O + CO_2$	87*
(4)	Fluidized-bed residual oil gasification	101.3	790-955	$CaO + H_2S = CaS + H_2O$	0.0026

* depends on CO_2, H_2O, CO, H_2 content

Note: 1 ppm ≡ 1.3 ng S/mL

The application of limestone desulfurization to the removal of SO_2 from flue gases (see (1) and (2) in Table 2.3), however, is limited to a maximum calcium oxide utilization of 45%. A strong diffusional resistance is developed in the interior of the particles as the reaction proceeds owing to the formation of the less porous $CaSO_4$ (34,35). Comparison of the molar volumes of reactants and products illustrates the significant increase in solid volume associated with the formation of the sulfate ($CaCO_3$, $\hat{V}$ = 36.9 cm^3/mol; CaO, $\hat{V}$ = 16.9 cm^3/mol; $CaSO_4$, $\hat{V}$ = 52.2 cm^3/mol).

Regeneration can be accomplished by one of two methods (36). The first, is a one step process, suitable for use at atmospheric pressure and temperatures greater than 950°C.

$$CaSO_4(s) + H_2(CO)(g) = CaO(s) + H_2O(CO_2)(g) + SO_2(g) \qquad 2.2.2.1$$

The second, incorporates a two step approach and is described by equations 2.2.2.2-4. This method consists of a reduction step followed by a mildly oxidizing step to convert the CaS to the carbonate. Regeneration is further facilitated by the solid-solid reaction 2.2.2.4.

$$CaSO_4(s) + 4\,H_2(4\,CO)(g) = CaS(s) + 4\,H_2O(4\,CO_2)(g) \qquad 2.2.2.2$$

$$CaS(s) + CO_2(g) + H_2O(g) = CaCO_3(s) + H_2S(g) \qquad 2.2.2.3$$

$$CaS(s) + 3\,CaSO_4(s) = 4\,CaO(s) + 4\,SO_2(g) \qquad 2.2.2.4$$

The extent of reaction 2.2.2.3 decreases rapidly as the stone is cycled between the desulfurizer and regenerator; consequently, the mean extent of regeneration is only 15% of the calcium content per cycle. None of the stones studied formed a totally regenerable calcium sulfide (33). This process is most favourable at pressures of 1015-1520 kPa and temperatures of 650-700°C.

In the desulfurization of reducing gas streams (see (3) and (4) of Table 2.3), the CaO utilization reaches 80-96% of total capacity compared to 45% for oxidizing streams. However, similar regenerability problems are encountered with calcium sulfide conversion according to reaction 2.2.2.3. In 1980, Nemeth et al. (38) patented a regeneration process in which the

regenerated limestone or dolomite has nearly the same capacity for reaction as the fresh sorbent. The sulfided sorbent is reacted with $CO_2/H_2O/O_2$ gas mixtures in the temperature range 925-1200°C at atmospheric pressure. Oxidizing conditions promote the conversion of sulfides to sulfates according to the following reactions:

$$CaS(s) + 4\,H_2O\,(4\,CO_2)(g) = CaSO_4(s) + 4\,H_2(4\,CO)(g) \qquad 2.2.2.5$$

$$CaS(s) + 2\,O_2(g) = CaSO_4(s) \qquad 2.2.2.6$$

$$CaS(s) + 3\,CaSO_4(s) = 4\,CaO(s) + 4\,SO_2(g) \qquad 2.2.2.4$$

For example, a gas mixture containing 3% O_2, 67% CO_2 and 30% H_2O can be used to regenerate the sulfided bed. Greater concentrations of O_2 increase SO_2 concentrations in the product gas but also convert a substantial portion of the CaS to $CaSO_4$ which is not as readily decomposed in the absence of CaS. In a typical desulfurization/regeneration cycle, the SO_2 concentration may be enriched from 2.0 to 3.2%. Nemeth suggested the use of a series of beds, alternating between desulfurization and regeneration, to concentrate the SO_2 sufficiently for subsequent by-product manufacture (e.g. sulfuric acid required a minimum of 3.5% SO_2).

2.2.3 Rare Earth Oxide or Rare Earth Mineral Desulfurization Processes

Four recently patented desulfurization processes, based on rare earth oxides or minerals, are summarized in Table 2.3: the Longo et al. and Baron et al. processes for use in oxidizing gas atmospheres, and the Wheelock et al. and Wilson et al. processes for use in reducing gas environments. Details of the chemistry and thermodynamics of these processes (with the exception of Wilson et al.) were not indicated.

In the Longo et al. processes (2,3), an oxidizing gas (eg. a flue gas from a utility boiler) containing SO_2 and/or SO_3 is contacted with a cerium oxide sorbent, preferably between 500-600°C. Unsupported cerium oxide or a supported sorbent containing 1-40 wt% CeO_2 (e.g. $(NH_4)_2\,[Ce\,(NO_3)_6]$ impregnated on γ-alumina and thermally decomposed at 300-

600°C) may be used. Note that none of the additional components of the flue gas, O_2, N_2, CO_2, CO, H_2O, NO or NO_2 are found to interfere with this process. When 30-70% of the adsorption capacity is reached, the sorbent is regenerated in a reducing atmosphere containing 15% H_2O in hydrogen or a mixture of hydrogen in nitrogen, preferably between 500-600°C. During regeneration, SO_2 is initially produced and after 50% regeneration, H_2S becomes the major species. Longo suggested using the effluent from the regeneration step as feed to a Claus Plant.

In the Baron et al. process (6), SO_x is removed from the regenerator associated with cyclical fluidized catalytic cracking (FCC) units used to convert hydrocarbon feedstocks into more valuable products. Bastnaesite particles, which cycle with the cracking catalyst, are used for this purpose.

In fluidized bed cracking of hydrocarbon feedstocks, catalyst particles pass through catalytic reactors called risers (see Figure 2.4) to convert the feedstock into gaseous lower boiling hydrocarbons. Because of coke deposition on the catalyst surface, the activity of the catalyst deteriorates rapidly if the coke is not removed. A stripper partially regenerates the particles with steam, converting some of the coke (containing sulfur) to hydrocarbon vapours (simultaneously releasing some of the sulfur as H_2S). Reactivation is then completed in a regenerator, where, in the presence of an oxygen containing gas such as air, the larger proportion of coke is removed by combustion. Sulfur is released in the regenerator as SO_x. The patent suggests the use of bastnaesite particles, circulating with the catalyst particles, to remove the SO_x produced in the regenerator. Regeneration of the bastnaesite particles occurs in the cracking unit and stripper, where reducing conditions favour the release of chemically sorbed sulfur as H_2S. Consequently, SO_x which would have otherwise been exhausted from the regenerator, is removed as H_2S by the existing desulfurization facilities.

Table 2.4:

Desulfurization Processes Using Rare Earths*

	Longo (1976),(1981)	Baron (1980)	Wheelock (1976,1977)	Wilson (1978/79/80)
Desulfurization				
Species Removed	SO_2, SO_3	SO_x	H_2S, COS	H_2S, COS
Inlet Conc.	0.1-20%	.07%	<10%	
Space Velocity	1000-10,000 GHSV		300-1000 vol gas·(vol catalyst)$^{-1}$·h^{-1}	
Sorbent	CeO_2	Bastnaesite	La_2O_3, Nd_2O_3/Pr_2O_3	Ce_2O_3, Bastnaesite
Temperature	500-600°C	480-760°C	350-550°C	
Regeneration				
Medium	H_2	H_2O	1) H_2O, 2) Air	
Space velocity	Not indicated	6.1-18.3 m/s	1) 2-5 moles H_2O·(mole H_2S)$^{-1}$·min^{-1} 2) 500-2500 vol gas·(vol catalyst)$^{-1}$·h^{-1}	
Temperature	500-600°C	425-600°C	300-600°C	
Products	1) SO_2 2) H_2S	H_2S	H_2S	

* Preferable conditions listed.

GHSV = gas hourly space velocity

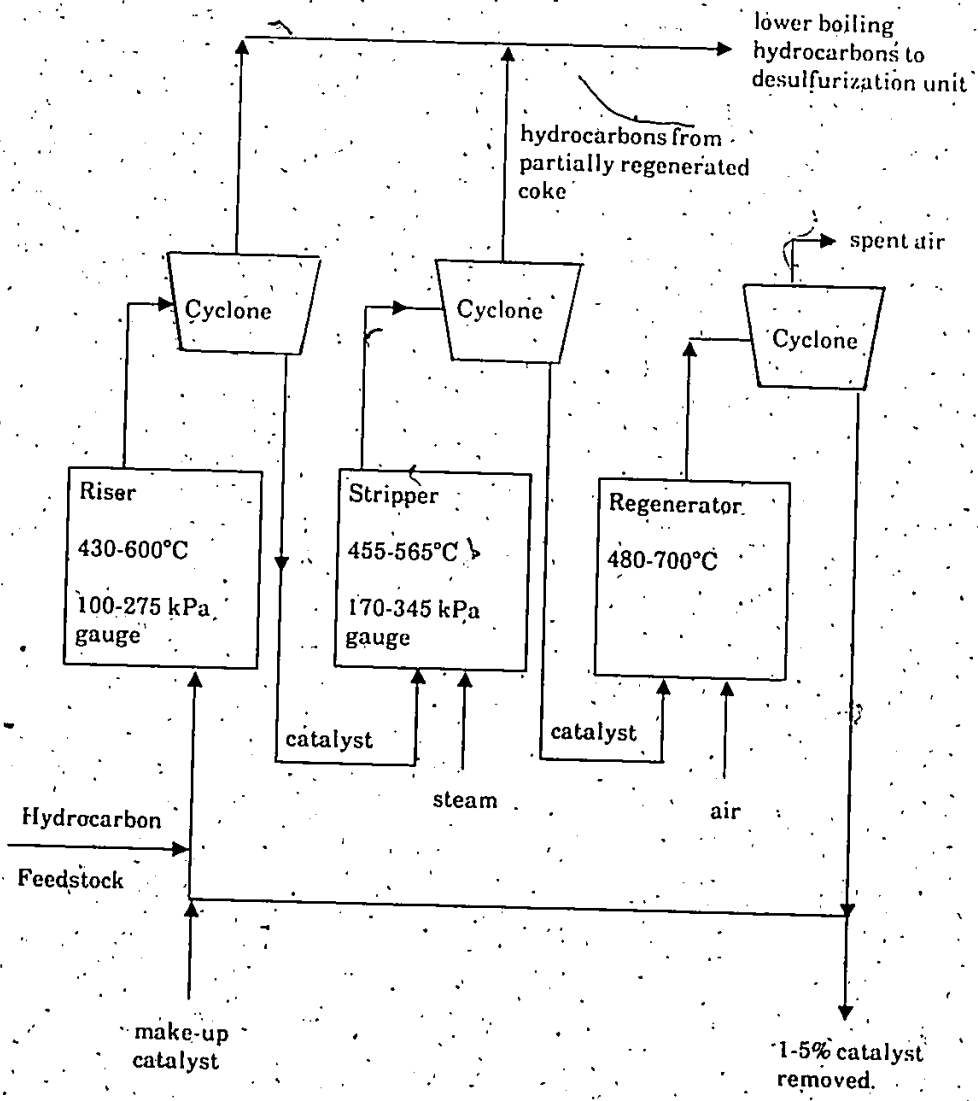

Figure 2.4: Cyclical Fluidized Catalytic Cracking Unit for Converting Hydrocarbon Feedstocks (based on reference 6)

Baron indicates that bastnaesite in its unaltered form (i.e. with at least some of the original fluorine present) has a greater activity than treated forms (i.e. calcined, steamed or leached). Sufficient air is required in the regenerator to prevent the deactivation of the bastnaesite particles from excessive coke depositions.

In the Wheelock et al. processes (4,5), H_2S and/or COS are adsorbed from reducing gas streams using rare earth oxide sorbents (eg. La_2O_3), at temperatures above 150°C (preferably between 370-450°C). Regeneration is accomplished by passing steam over the sorbent, at temperatures and pressures similar to those used during desulfurization, to release chemically sorbed sulfur in concentrations greater than in the original feed stream. Because the steam desorbed sorbent does not have sufficient activity to be used in subsequent sorption cycles, regeneration is completed by contacting the sorbent with an oxidizing gas, such as air, at similar temperatures and pressures. Since the cited examples state that 100% of the sulfur is desorbed as H_2S during steam regeneration, it is probable that air is required to convert $La(OH)_3$ to La_2O_3. Based on thermodynamic data, recently published by Dwivedi (16) for the La-O-S system, regeneration of lanthanum oxide sorbents under conditions of low oxygen potential (eg. steam) would be necessary to avoid the formation of a stable oxysulfate which does not decompose, in air, below 1670°C.

The process in its preferred embodiment, utilizes supported sorbents containing 10-30 wt% of a rare earth oxide. Alkali or alkaline earth oxides (eg. Na_2O, K_2O) can be used as promoters. Although the patent claims that hydrated sorbents containing cerium can be regenerated by using nitrogen to purge the sorbent of H_2S, this was not found to occur in this study, probably because cerium hydroxides are not stable at the higher temperatures used in this investigation (800-1000°C). No attempt was made to verify Wheelock's claim.

The Wilson and Kay process (7,8) was investigated in this thesis. Although rare earth oxides or bastnaesite concentrates can be used for desulfurization of any fluid material

(i.e. molten iron or steel, stack gases, coal gasification or liquefaction products), this study focused on the application to coal gasification products.

Chapter III

THERMODYNAMICS AND CHEMISTRY

In this chapter, literature dealing with the cerium-oxygen-sulfur system is summarized and used to complete the Ce-O-S thermodynamic phase stability diagram in the temperature range 1073 to 1273 K. The following changes are recommended, in addition to those suggested by Dwivedi (16) in 1982:

(1) The Ce_2O_2S/CeO_{2-x}, Ce_2O_2S/CeO_2, $Ce_2S_3/Ce_2(SO_4)_3$, and Ce_2S_3/CeO_2 boundaries have been added.

(2) The Ce_2O_{3+x} phase has been added.

(3) The $CeO_{1.714}$ phase is noted to disappear above 1025°C (see Figure 6.14 in Chapter 6).

(4) The CeO_2/CeO_{2-x} phase boundary has been dotted to indicate that a clear distinction does not physically exist between these two phases, but rather a gradual transition from one phase to the other occurs.

This diagram is used in sections 3.2 and 3.3 to determine the predominant desulfurization reactions for a cerium oxide sorbent in contact with a typical coal gas containing CO, CO_2, H_2, and H_2S. The summary, given below, reviews the data included in the diagram, and draws attention to newly identified phases for which thermochemical data are currently unavailable but may need to be included in future versions. Equilibrium constants for the predominant reactions were also calculated.

3.1 Review of Reported Cerium Oxides, Sulfides and Sulfates

3.1.1 Cerium Oxides

A cerium oxygen phase diagram, which correlates most of the direct phase analysis work accomplished to-date, was suggested by Height and Bevan in 1976 (39) and is shown in Figure 3.1. Corresponding oxide phases and their peritectoidal decomposition temperatures are summarized in Table 3.1. Lattice parameters of these compounds can be found in reference (39).

At temperatures above 1025 ± 5°C (the peritectoidal decomposition temperature of $CeO_{1.714}$), two nonstoichiometric phases, Ce_2O_{3+x} and CeO_{2-x}, dominate the phase diagram. Bevan commented that the CeO_{2-x} phase region, until now considered to be continuously non-stoichiometric, shows grossly non-ideal behaviour and has been interpreted by Sorensen (40) as divided into several distinct nonstoichiometric subregions (see insert Figure 3.1). Below 685°C, Bevan and Kordis (41) reported a miscibility gap consisting of two nonstoichiometric CeO_{2-x} phases α' and α. Desulfurization experiments in this study were conducted above 700°C; consequently, the phases considered for the construction of the Ce-O-S phase stability diagrams were Ce_2O_3, Ce_2O_{3+x}, $CeO_{1.714}$, CeO_{2-x} and CeO_2. In section 3.2, it will be shown that CeO_{2-x} is the stable oxide phase in typical coal gases.

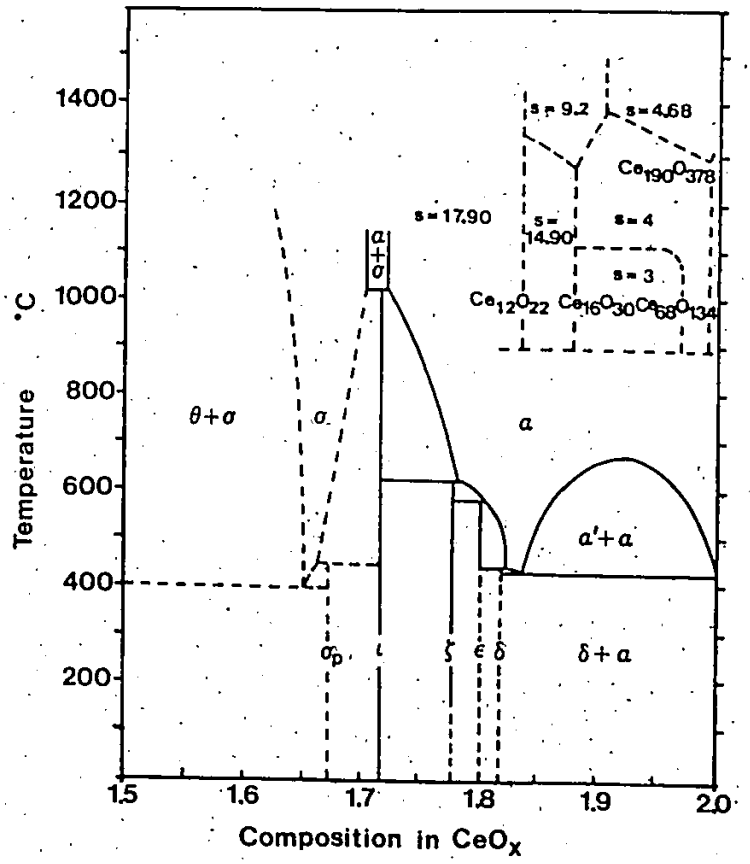

Figure 3.1: The CeO_x Phase Diagram. (s denotes a region where the isotherms have the slope specified*) (39).

α = CeO_{2-x}

δ = $CeO_{1.818}$ = $Ce_{11}O_{20}$

ε = $CeO_{1.800}$ = $Ce_{10}O_{18}$

ζ = $Ce_{1.778}$ = Ce_9O_{16}

ι = $Ce_{1.714}$ = Ce_7O_{12}

σ = Ce_2O_{3+x}

σ_p = $CeO_{1.67}$

θ = $CeO_{1.5}$

* See Appendix 5.

Table 3.1:

Table of Cerium Oxide Phases (39)

Phase	Composition	Alternative Formula	Colour*	vacancy/unit cell (fraction of oxygens missing)	Peritectoidal Decomposition Temperature (°C)
∞	CeO_2		pale yellow	0	–
α	CeO_{2-x}		blue		–
δ	$CeO_{1.818}$	$Ce_{11}O_{20}$	dark blue	(1/11)	445 ± 10
ε	$CeO_{1.800}$	$Ce_{10}O_{18}$	dark blue	(1/10)	585 ± 10
ζ	$CeO_{1.778}$	Ce_9O_{16}	dark blue	(1/9)	625 ± 10
ι	$CeO_{1.714}$	Ce_7O_{12}	blue-black	2 (1/7)	1025 ± 5
σ	Ce_2O_{3+x}		black		–
σ_p	$CeO_{1.67}$		black		–
θ	$CeO_{1.5}$	Ce_2O_3	white	0	–

* The colours were used to identify the oxide present under desulfurization conditions experimentally.

Cerium dioxide has the face-centred cubic fluorite type structure which can be described either as edge shared MO_8 cubes in a three dimensional chess-board network or as edge shared OM_4 tetrahedra. This structure type is very stable, even in grossly non-stoichiometric phases for anion to cation ratios both greater than and less than two. When oxygen is removed from this structure, the crystalline products are fluorite-related either as members of an homologous series of intermediate oxides having the formula $Ce_n O_{2n-2}$ or as non-stoichiometric phases CeO_{2-x} or Ce_2O_{3+x}. The nonmetal constituent is extremely mobile in fluorite-type materials; oxygen is mobile at 300°C (39). It will be subsequently shown in section 6.2.1.3 that the oxygen mobility plays an important role in the desulfurization reaction. In contrast, the metal substructure is rigid up to the melting point of the oxide and temperatures of the order of 1200 - 1400°C are required before appreciable metal atom movement occurs. These materials are among the most thermally stable known, melting at about 2500°C. For the intermediate oxide phases of CeO_2, the composition may be adjusted by annealing at suitable oxygen pressures and temperatures (see Figure A1.1 in Appendix 1) without destroying the crystal integrity.

Three studies have provided strong evidence that the predominant non-stoichiometric defects in CeO_{2-x} are oxygen vacancies. Oxygen self-diffusion coefficients were measured by Faber (46) using X-ray and neutron diffraction measurements from 800 to 1000°C. Panlener et al. (47) showed that oxygen vacancies are doubly ionized and essentially randomly distributed near stoichiometry ($x \leq 0.006$). Steel and Floyd (see Table 3.2) obtained activation energies for oxygen mobility in non-stoichiometric ceria. Larger oxygen diffusion coefficients were obtained as the number of vacancies increased. For ceria close to stoichiometry the activation energy for the mobility of oxygen ions is approximately 84 kJ (48).

Table 3.2:

Oxygen Self-diffusion Data for Ceria as Reported by Steel and Floyd (48) from 850 to 1150°C. $D = D_e \exp(-E_a/RT)$

Composition	Anion Vacancy Concentration (%)	Pre-exponential term (cm^2/s)	Error in D_e	Activation Energy (kJ)
$CeO_2(p_{O_2}=0.21)$	$<10^{-2}$	1.9×10^{-4}	$(-1.4/+5.7)10^{-4}$	104 ± 15
$CeO_2(p_{O_2}=0.21)$*	$<10^{-2}$	1.4×10^{-4}	$(-0.3/+0.4)10^{-4}$	89.1 ± 2.5
$CeO_2(p_{O_2}=0.02)$	$<10^{-2}$	1.8×10^{-5}	$(-1.2/+2.1)10^{-5}$	72.8 ± 8.0
$CeO_{1.92}$	4	1.5×10^{-5}	$(-1.2/+6.1)10^{-5}$	49.8 ± 16
$CeO_{1.8}$	10	6.2×10^{-6}	$(-5.0/+2.5)10^{-6}$	15.1 ± 18

* polycrystalline sample

3.1.2 Cerium Sulfides and Oxysulfides

Figure 3.2 is a modified version of the cerium-sulfur phase diagram which is given in a review by Gschneidner (42). Four cerium sulfides have been reported -- CeS, Ce_3S_4, Ce_2S_3 and CeS_2. The Ce_5S_7 phase has been deleted from the original diagram. Two polymorphic forms of Ce_2S_3 have been identified. The α-type is orthorhombic, stable at low temperatures and is exactly stoichiometric. The γ-type, based on the Ce_3S_4 structure, has a body-centered cubic cell containing 16/3 Ce_2S_3 formulas or $4Ce_{8/3}S_4$ formulas. Vacancies exist on the metal sites and have a disordered arrangement. By filling the vacancies, continuous solid solutions are obtained from Ce_2S_3 ($Ce_{8/3}\square_{1/3}S_4$) to the Ce_3S_4 composition. Besançon (43) determined the $\alpha \rightleftharpoons \gamma$ transition temperature of 1150°C by Differential Thermal Analysis. Thus, above 1150°C, a clear physical boundary does not exist between the Ce_2S_3 and Ce_3S_4 phases.

Besançon (43) showed that the compound previously believed to be β-Ce_2S_3 by Marcon (44) and Ce_5S_7 by Klinvex and Berger (45) is actually $Ce_{10}S_{14}O$. This compound is tetragonal with the oxygen atom having a special position at the center of the tetrahedron of cerium atoms. It is possible to substitute the oxygen by a sulfur atom giving rise to a solid solution of composition $Ce_{10}S_{14}O_{1-x}S_x$. Besançon reported that $Ce_{10}S_{14}O$ is stable to temperatures of 1500-1600°C and can be formed via reaction 3.1.2 above 1300°C.

$$9\,\gamma\text{-}Ce_2S_3(s) + Ce_2O_2S(s) = 2Ce_{10}S_{14}O(s) \qquad 3.1.2$$

Hexagonal Ce_2O_2S was the first oxysulfide to be reported; Zachariasen published the crystal structure in 1949 (49). In 1978, Wichelhaus (50) and Guittard and Dugué (51) reported two new oxysulfides, $Ce_4O_4S_3$ and $Ce_6O_6S_4$ with intermediate valence. Both compounds contain Ce^{3+} and Ce^{4+} ions and belong to the same general formula $Ce_{2n}O_{2n}S_{n+1}$ or $Ce^{III}_{2n-2}Ce^{IV}_{2}O_{2n}S_{n+1}$. The structure of these oxysulfides, based on the Ce_2O_2S lattice, contain periodic dislocations parallel to the x0z plane; the period of the dislocation being 2 and

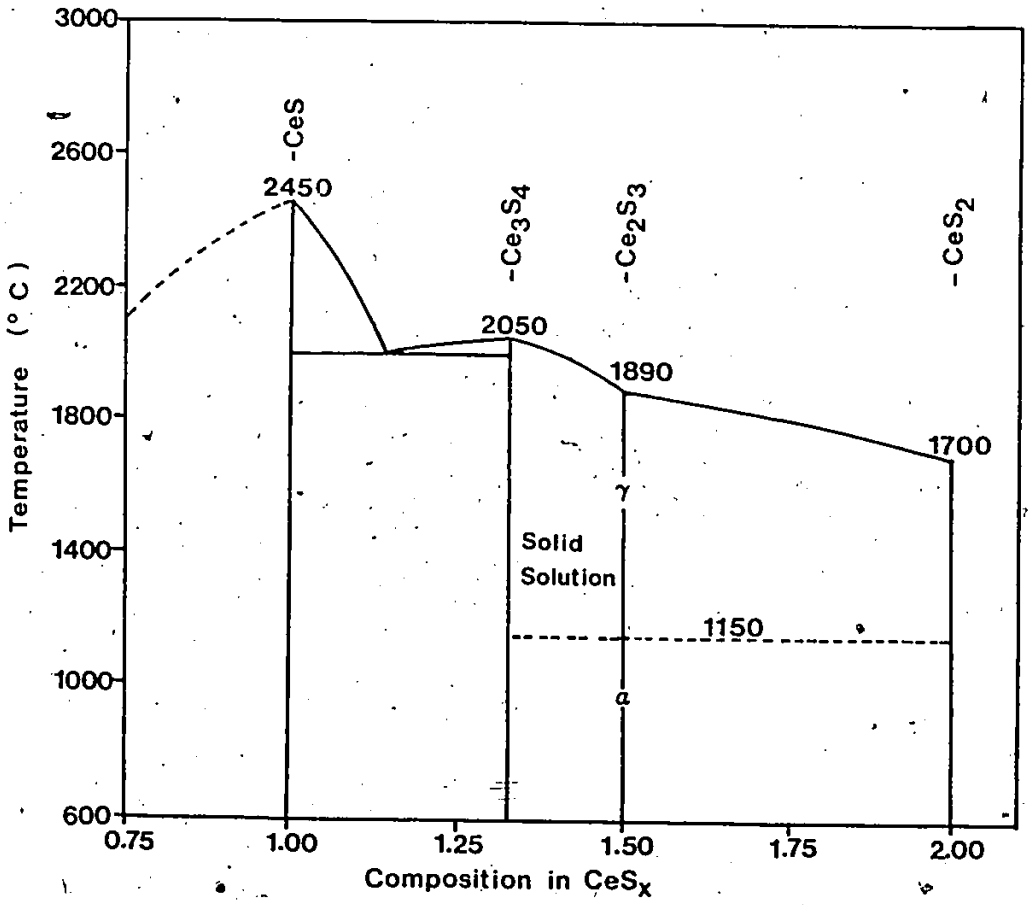

Figure 3.2: The Cerium-Sulfur Phase Diagram (after Gschneidner).

3 unit cells of Ce_2O_2S when n = 2 and n = 3 respectively (51). Black crystals of $Ce_4O_4S_3$ were prepared by reaction of CeO_2 with Ce_2S_3 in an NaCl/KI melt enclosed in an evacuated quartz tube at 550-600°C. It decomposes above 730°C in vacuo to form Ce_2O_2S and elemental sulfur (50).

Thus, for Ce-O-S phase stability diagrams between 800 to 1000°C, sulfide phases which should be included are CeS, Ce_3S_4, α-Ce_2S_3 and Ce_2O_2S.

3.1.3 Cerium Sulfates and Oxysulfates

Further work is necessary to resolve conflicting reports in the literature regarding the composition of the various sulfates and their decomposition properties. Duval (52) first reported TGA decomposition studies of $Ce(SO_4)_2 \cdot 3.1\ H_2O$ in 1956. Below 197°C, physical desorption of water was observed. The sulfate began to lose weight at 300°, with maximum weight loss occurring between 450° - 540°C, after which the TGA was terminated. The decomposition product was believed to be $3\ CeO_2 \cdot 4\ SO_3$. Another TGA/DTA study of $Ce(SO_4)_2$, by Lóránt (53) in 1965, stated that $Ce(SO_3)_2$ was formed above 400°C which subsequently decomposed to cerium dioxide at 860°C. However, the TGA/DTA curves were not given. Omer et al. (54), in 1981, published TGA decomposition studies of $Ce(SO_4)_2$ in a molten lithium sulfate-sodium sulfate-potassium sulfate eutectic. $Ce(SO_4)_2$ reacted with the melt in two stages commencing at 100° and 750°C, respectively, forming pale yellow products in both stages with the evolution of SO_3. The powder diffraction patterns of the products from the first and last stages corresponded to $CeOSO_4 \cdot H_2O$ and CeO_2 respectively. The reactions, however, are not believed to be the simple decomposition of $Ce(SO_4)_2$.

$$Ce(SO_4)_2(s) = CeOSO_4(s) + SO_3(g) \qquad 3.1.1$$

$$CeOSO_4(s) = CeO_2(s) + SO_3(g) \qquad 3.1.2$$

Table 3.3:

Table of Cerium Sulfides (42)

Compound	Crystal Class	Lattice Parameters Å a	b	c
CeS	cubic	5.769 ± 4	–	–
Ce_3S_4*	cubic	8.628 ± 3	–	–
α-Ce_2S_3	ortho.	7.513	4.091	15.715
γ-Ce_2S_3*	cubic	8.630 ± 1	–	–
CeS_2	cubic	8.115 ± 5	–	–

* These two phases form a complete series of solid solutions at high temperature.

Longo (3) has reported the formation of $CeOSO_4 \cdot H_2O$ in a flue gas desulfurization process using cerium oxide at 500° - 700°C. Clearly this oxysulfate must be stable at least to the upper temperature limit of this process. The crystal structure of this compound has been reported by Lundgren (55), Gillespie (56), and Lindgren (57).

Other reported oxysulfates or oxysulfites (58,59) for which structural and decomposition data are sparse are:

$2CeO_2 \cdot 3SO_3 \cdot 5H_2O$, $3CeO_2 \cdot 2SO_3 \cdot 3H_2O$, $4CeO_2 \cdot 3SO_3 \cdot 12H_2O$, $6CeO_2 \cdot 5SO_3 \cdot 12H_2O$, $CeO_2 \cdot SO_3 \cdot H_2O$, and $CeO_2 \cdot SO_3 \cdot 2H_2O$.

Decomposition studies of cerium (III) sulfate have been more conclusive. Studies by Nathans and Wendlandt (60) showed that decomposition to CeO_2 commences at 700°C and becomes rapid at 920°C. Omer et al. (54) studied the decomposition of $Ce_2(SO_4)_3$ using the melt technique previously mentioned. An unidentified colourless intermediate was formed at 580°C which subsequently decomposed to CeO_2 at 760°C. It must again be pointed out that decomposition reactions in the sulfate eutectic are probably not representative of ordinary decomposition reactions. A few decomposition properties are summarized in Table 3.4. Clearly, much work needs to be done to resolve the various sulfate phases, their decomposition and thermodynamic properties. $Ce_2(SO_4)_3$ was the only sulfate included in the Ce-O-S phase stability diagrams because thermodynamic data for other sulfates were not available.

Table 3.4:

Decomposition Properties of Reported Rare Earth Sulfates

Compound	Product of Decomposition	Temperature Range (°C)	Reference
$Ce_2(SO_4)_3$	CeO_2	760-950	60
$Ce(SO_4)_2$	$Ce(SO_3)_2$	400-860	53
$Ce(SO_3)_2$	CeO_2	> 860	53
$Ce(SO_4)_2$	$CeOSO_4$	100 *	54
$CeOSO_4$	CeO_2	750 *	54

* decomposition in molten sulfate eutectic.

3.2 Thermodynamic Ce-O-S Phase Stability Phase Diagrams and Their Use

In the construction of high temperature phase stability diagrams in the range 1073 to 1273 K, standard free energies of formation (61-63), see Table 3.5, of a pair of compounds are combined to give an equation defining the boundary between the phase fields. Sample calculations are provided in Appendix 1 and the resulting equations are summarized in Table 3.6. The boundaries between the cerium oxide phases were determined from the data of Bevan and Kordis (41). For example, the phase change from CeO_{2-x} to $CeO_{1.714}$ at 1145°K occurs at an oxygen partial pressure given by $-\log p_{O_2} = 23.4$ in accordance with the phase rule (see Appendix 1, Figure A1.1 and Table A1.2). A typical Ce-O-S phase stability diagram at 1145 K is illustrated in Figure 3.3. Stability diagrams at four other temperatures 1073, 1189, 1244 and 1296 K were constructed and are given in Figures 6.12-6.15 of Chapter 6.

When a cerium oxide sorbent is exposed to a gas containing CO, CO_2, H_2 and H_2S, the initial gas phase composition and temperature can be used in conjunction with the Ce-O-S phase stability diagram to predict the reactants and products. However, this technique should be used cautiously because the equilibrium products are not necessarily the real products. The computer program F*A*C*T (described in Appendix 2), calculates the equilibrium composition of the gas before desulfurization, at the conditions prevailing in the reactor, from the room temperature composition of the gas. The calculated oxygen and sulfur partial pressures determine the thermodynamically stable solid product of reaction.

For example, consider a gas mixture of composition A (see Table 3.7) at room temperature, with corresponding high temperature gas composition B (see Appendix 2 for detailed listing of composition). The oxygen and sulfur potentials of gas B are represented by point B on the phase stability diagram and shows that the Ce-O-S phase in equilibrium with this gas is Ce_2O_2S.

Table 3.5

Standard Free Energies of Formation of Relevant Cerium Compounds

$\Delta G° = \Delta H° - T\Delta S°$ kJ/mol

Reaction	$\Delta H°$ (kJ/mol)	$\Delta S°$ (kJ/(mol·K))	Estimated Error (kJ)
$CeO_2(s) = Ce(\ell) + O_2(g)$	1086.38	0.2121	± 13
$Ce_2O_3(s) = 2Ce(\ell) + 3/2\ O_2(g)$	1780.80	0.2761	± 13
$CeS(s) = Ce(\ell) + 1/2\ S_2(g)$	554.30	0.1042	± 8
$Ce_3S_4(s) = 3Ce(\ell) + 2S_2(g)$	2021.63	0.4109*	± 42
$Ce_2S_3(s) = 2Ce(\ell) + 3/2\ S_2(g)$	1469.25*	0.3180*	± 42
$Ce_2O_2S(s) = 2Ce(\ell) + O_2(g) + 1/2\ S_2(g)$	1718.49	0.2720	± 63
$Ce_2(SO_4)_3(s) = 2Ce(\ell) + 6O_2(g) + 3/2\ S_2(g)$	4133.64	1.4009	± 13

*Estimated.

Valid temperature range is 1071-2000 K

Table 3.6:

Equations Defining the Location of Boundaries on the Ce-O-S Phase Stability Diagram

Boundary	Equation	Reference
CeS/Ce_3S_4	$\log p_{S_2} = -37469.8/T + 10.3$	7
$*Ce_3S_4/Ce_2S_3$	$\log p_{S_2} = -38072.7/T + 13.8$	7
Ce_2O_3/Ce_2O_2S	$\log p_{O_2} = \log p_{S_2} - 6507.61/T + 0.43$	7
CeS/Ce_2O_2S	$\log p_{O_2} = 1/2 \log p_{S_2} - 31851.9/T + 3.3$	7
Ce_3S_4/Ce_2O_2S	$\log p_{O_2} = 5/6 \log p_{S_2} - 19362.0/T + 0.10$	7
$*Ce_2S_3/Ce_2O_2S$	$\log p_{O_2} = \log p_{S_2} - 13016.5/T - 2.4$	7
Ce_2O_3/Ce_2O_{3+x}	$\log p_{O_2} = -24.7$ at 1145 K	this work
$Ce_2O_{3+x}/CeO_{1.714}$	$\log p_{O_2} = -24.0$ at 1145 K	this work
$CeO_{1.714}/CeO_{2-x}$	$\log p_{O_2} = -23.4$ at 1145 K	16, this work
$*CeO_{2-x}/CeO_2$	$\log p_{O_2} = -15.0$ at 1145 K	16, this work
$CeO_2/Ce_2(SO_4)_3$	$\log p_{O_2} = -3/8 \log p_{S_2} - 25576.8/T + 12.88$	16, this work
CeO_2/Ce_2O_2S	$\log p_{O_2} = 1/2 \log p_{S_2} - 2334.9/T + 7.43$	this work
$*Ce_2S_3/Ce_2(SO_4)_3$	$\log p_{O_2} = -23193.3/T + 9.43$	this work
$*CeO_2/Ce_2S_3$	$\log p_{O_2} = -3/4 \log p_{S_2} - 18426.3/T + 2.50$	this work

* Estimated

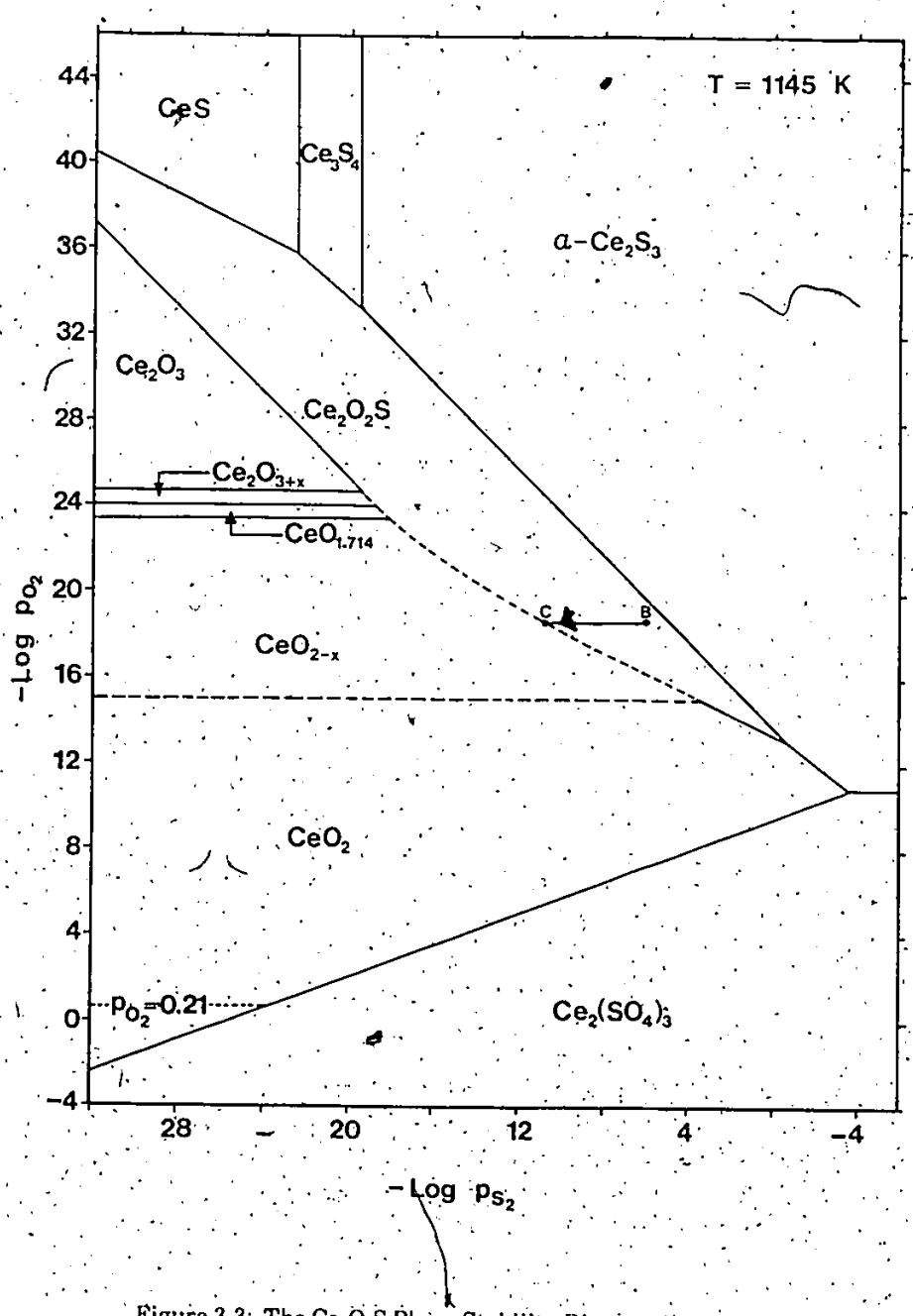

Figure 3.3: The Ce-O-S Phase Stability Diagram at 1145 K.

Table 3.7

Table of Gas Compositions

Components	Composition (mole fraction) A	B	C
CO	0.550	0.591	0.591
H_2	0.330	0.289	0.289
CO_2	0.108	0.0679	0.0679
H_2O	–	0.0420	0.0420
H_2S	0.011	0.0101	5.02×10^{-5}
S_2	–	1.01×10^{-6}	2.51×10^{-11}
O_2	–	2.65×10^{-19}	2.65×10^{-19}
T(K)	298	1145	1145
P(kPa)	101.3	101.3	101.3

Concentrations of the major components CO, CO_2, H_2, H_2O are comparatively unchanged in the desulfurization of dilute H_2S streams, thus the path of the desulfurization reaction can be represented by a line with constant oxygen partial pressure, until the gas composition reaches the point C in Figure 3.3, corresponding to the CeO_{2-x}/Ce_2O_2S equilibrium. Beyond this point, no further desulfurization can occur. Point C predicts that the solid reactant phase is CeO_{2-x} and determines the final composition of the gas phase. Although the boundary between the CeO_{2-x} and Ce_2O_2S phase fields cannot be calculated owing to the lack of thermodynamic information, estimates of the final gas composition at equilibrium can be made by drawing a smooth curve joining the Ce_2O_3/Ce_2O_2S and CeO_2/Ce_2O_2S boundaries. From Figure 3.3, estimated equilibrium concentrations at point C are $p_{S_2} = 2.51 \times 10^{-11}$ atm or $p_{H_2S} = 5.02 \times 10^{-5}$ atm (65 ngS/mL, 50 ppm). In section 6.2, these estimates will be compared with experimental data. The thermodynamically predicted H_2S concentrations are well below the EPA standards of 1000 ppm (1300 ng S/mL) for temperatures up to 1273 K.

The limitations of the phase stability diagram are as follows:

1. The diagrams presented in this work, strictly apply to the temperature range of 800°C to 1100°C. Other oxide phases exist below 685°C as described by Figure 3.1. Above 1150°C, the Ce_2S_3/Ce_3S_4 phase boundary will not be clearly defined because of the formation of a solid solution of the two sulfides.
2. Other oxysulfide phases, i.e. $Ce_{10}S_{14}O_{1-x}S_x$ may exist.
3. Other sulfate phases may exist between the CeO_2 and $Ce_2(SO_4)_3$ phases.
4. The diagram represents equilibrium conditions only. Experimentally measured concentrations may differ from predicted values if equilibrium is not attained.
5. Some chemical reactions, although thermodynamically possible, will not occur to an appreciable extent because of kinetic limitations.

3.3 Chemistry

3.3.1 Reduction

The strong reducing atmosphere present in low/medium-heat content coal gases permits the reduction of CeO_2 in the desulfurization reactor. The composition of the stable oxide phase for a given temperature is uniquely determined by the oxygen partial pressure as shown in Figure A1.1 (Appendix 1). For most low/medium grade coal gases, the non-stoichiometric CeO_{2-x} phase is formed. This conclusion was further verified upon examination of partially desulfurized pellets which showed an inner core containing a blue solid (see section 6.2). The reduction reactions may be represented as:

$$CeO_2(s) + xCO(g) = CeO_{2-x}(s) + xCO_2(g) \qquad 3.3.1$$

$$CeO_2(s) + xH_2(g) = CeO_{2-x}(s) + xH_2O(g) \qquad 3.3.2$$

Estimated free energies of reaction and equilibrium constants were calculated, using Barin, Knacke and Kubaschewski's data for $CeO_{1.83}$ (64).

$$CeO_2(s) + 0.170CO(g) = CeO_{1.83}(s) + 0.170CO_2(g) \qquad 3.3.3$$

$$\Delta G^\circ = 2004.8 - 1.90\,T \text{ cal}$$

$$= 8.3867 - 0.00795\,T \text{ kJ}$$

$$K_{1100} = 1.04$$

$$CeO_2(s) + 0.170H_2(g) = CeO_{1.83}(s) + 0.170H_2O(g) \qquad 3.3.4$$

$$\Delta G^\circ = 22552 + 2.33\,T \text{ cal}$$

$$= 94.342 + 0.00975\,T \text{ kJ}$$

$$K_{1100} = 1.03 \times 10^{-5}$$

The equilibrium constants of equations 3.3.3 and 3.3.4 show that reduction of cerium dioxide is thermodynamically more favourable with carbon monoxide than with hydrogen.

3.3.2 Desulfurization

During desulfurization of low/medium grade coal gases, H_2S reacts with non-stoichiometric CeO_{2-x} to form Ce_2O_2S (see thermodynamic arguments in section 3.2). The chemical reactions may be represented as:

$$2CeO_{2-x}(s) + H_2S(g) + (1-2x)H_2(g) = Ce_2O_2S(s) + 2(1-x)H_2O(g) \quad 3.3.5$$

$$2CeO_{2-x}(s) + H_2S(g) + (1-2x)CO(g) = Ce_2O_2S(s) + H_2O(g) + (1-2x)CO_2(g) \quad 3.3.6$$

Since there is no net change in the number of moles of gaseous species in reactions 3.3.5 and 3.3.6, total pressure will not affect equilibrium compositions. Combining Gschneidner's data for Ce_2O_2S (61,62) with Barin, Knacke and Kubaschewski's data for non-stoichiometric $CeO_{1.83}$, the standard free energy changes and equilibrium constants are:

$$2\,CeO_{1.83}(s) + H_2S(g) + 0.66\,H_2(g) = Ce_2O_2S(s) + 1.66\,H_2O(g) \quad 3.3.7$$

$$\Delta G^\circ = 6331 - 11.0\,T \text{ cal}$$

$$= 26.48 - 0.0460\,T \text{ kJ}$$

$$K_{1100} = 14.06$$

$$2CeO_{1.83}(s) + H_2S(g) + 0.66CO(g) = Ce_2O_2S(s) + H_2O(g) + 0.66\,CO_2(g) \quad 3.3.8$$

$$\Delta G^\circ = 1061 - 6.09\,T \text{ cal}$$

$$= 4.451 - 0.0255\,T \text{ kJ}$$

$$K_{1100} = 13.2$$

Note that equilibrium constants are large in the temperature range of interest (1071-1273 K) indicating favourable desulfurization; reactions can be considered to be irreversible for $K_{eq} \geqslant 10$.

3.3.3 Secondary Reactions

Unless the components of the simulated coal gas, CO, CO_2, H_2, H_2S, and H_2O are introduced into the desulfurizer in proportions generally existing in the reactor at a given

temperature, reactions between the components will occur. Of major importance are the water-gas shift reaction, the Boudouard reaction, and the hydrogen sulfide dehydrogenation reactions

$$CO_2(g) + H_2(g) = CO(g) + H_2O(g) \qquad 3.3.9$$

$$2CO(g) = C(s) + CO_2(g) \qquad 3.3.10$$

$$CO(g) + H_2S(g) = COS(g) + H_2(g) \qquad 3.3.11$$

$$CO_2(g) + H_2S(g) = COS(g) + H_2O(g) \qquad 3.3.12$$

The computer program, F*A*C*T (refer to section 3.2 and Appendix 2), was used to determine the equilibrium gas compositions entering a bed of cerium oxide based on the assumption that equilibrium was attained in the preheating zone of the reactor. Other investigators (31) have shown that this assumption is valid at the high temperatures used in this study. Experimentally, carbon deposition was not observed.

3.3.4 Regeneration

Oxidation of oxysulfides in the spent sorbent under conditions of high oxygen potential permits the regeneration and recycling of the oxides. In air ($-\log p_{O_2} = 0.678$, $-\log p_{S_2} < 24$), CeO_2 will be predominantly produced with release of adsorbed sulfur as SO_2 according to reaction 3.1.13.

$$Ce_2O_2S(s) + 2O_2(g) = 2CeO_2(s) + SO_2(g) \qquad 3.3.13$$

$$\Delta G^\circ = -195164 + 1.52\,T \text{ cal}$$

$$= -816.432 + 0.00636\,T \text{ kJ}$$

$$K_{1100} = 2.67 \times 10^{38}$$

Further discussion of regeneration reactions is given in section 6.2.2.

Chapter IV

GAS-SOLID REACTION KINETICS

The work discussed in this thesis is primarily concerned with the chemistry and thermodynamics of the desulfurization reaction of cerium oxide or bastnaesite with H_2S. However, a kinetic analysis is ultimately required to determine the feasibility of the process. In this chapter, a simple kinetic model is selected and used to ascertain the parameters necessary to estimate the relative reaction rates from the preliminary breakthrough curves presented in section 6.2.1.5. These results are needed in order to proceed with further developmental work.

4.1 Kinetic Modelling

Both the desulfurization and regeneration reactions discussed in Chapter III, are examples of heterogeneous non-catalytic gas-solid reactions of the type:

$$A(g) + bB(s) = cC(g) + dD(s) \qquad 4.1$$

where A and B are the gaseous and solid reactants; C and D are the gaseous and solid products; and b, c, and d are their respective stoichiometric coefficients.

The following series of steps are involved in the overall reaction process (74):

(1) Gas phase mass transfer of the gaseous reactant from the bulk of the gas stream to the external surface of the solid particle.

(2) Diffusion of the gaseous reactant through the pores of the solid matrix, which could consist of a mixture of solid reactants and products.

(3) Adsorption of the gaseous reactant on the surface of the solid matrix.

(4) Chemical reaction at the surface of the solid matrix.

(5) Desorption of the gaseous product from the surface of the solid matrix.

(6) Diffusion of the gaseous reaction product through the pores of the solid matrix.

(7) Gas phase mass transfer of the gaseous product from the external surface of the solid to the bulk of the gas stream.

Steps (5), (6) and (7) do not contribute directly to the observed rate of reaction in this study because the reactions can be considered to be irreversible (see sections 3.3.2 and 3.3.4).

Levenspiel (76) recently summarized the mathematical models available for gas-solid reactions, see Figure 4.1. Since sulfur loaded pellets show a blue inner core of CeO_{2-x} surrounded by a green outer shell of sulfide, diffusion must be the predominant mechanism. The reaction is also associated with a decrease in porosity (see Appendix 6). Thus the uniform conversion, crackling core and thermal decomposition models are unsuitable. The shrinking core model was not used because it can be obtained as a special case of the grain model (diffusion controlled reactions in non-porous solids). Simple equations were selected from the two remaining models for the feasibility studies. The relationship between the adsorption capacity and the physical properties of the solid reactants and products, has been derived by Ramachandran and Smith using the changing voidage pore model (77). This relationship is valid in the absence of pore diffusion control and is therefore helpful in the identification of the rate determining mechanism (see Appendix 6 and section 6.2.1.4). However, this model has only been applied to the reaction of single particle systems. The limited amount of kinetic data presented in this thesis does not warrant a complex derivation to obtain equations applicable to a fixed bed system. The relationship between the rate of reaction and the slope of the breakthrough curve, on the other hand, is easily obtained from the grain model. This model cannot account for changes in porosity, but is satisfactory for a preliminary kinetic evaluation of the process. A more suitable model can be selected when the process has been optimized. The remainder of this chapter briefly summarizes the relevant equations.

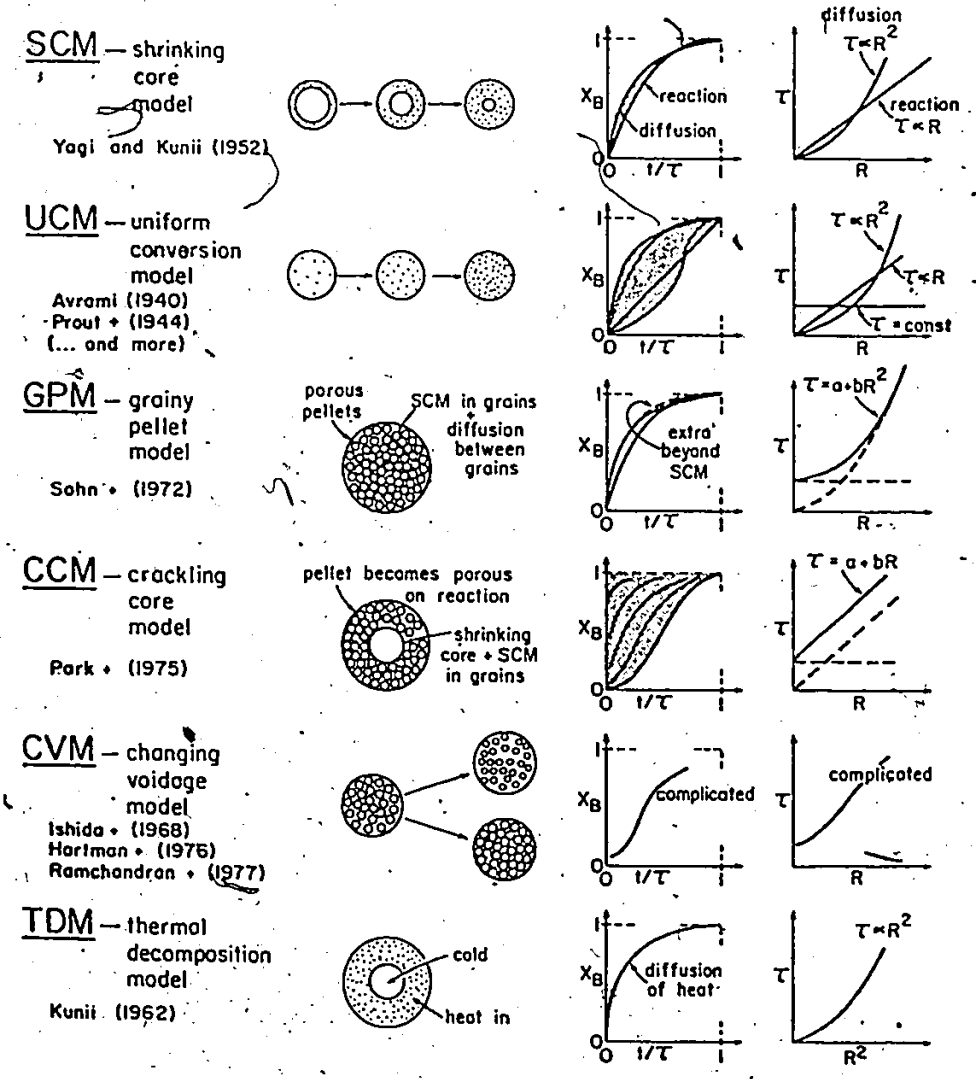

Figure 4.1: A summary of kinetic models for gas solid reactions (taken from reference 76)

In the grain model, porous pellets are considered to be agglomerations of uniform grains which may be spheres, long cylinders or flat plates (for which the grain shape factor, F_g, is 3, 2, or 1, respectively). Each grain reacts according to the shrinking core model. The model allows for the limitation of the progress of reaction by intergranular diffusion of gaseous reactant as well as by the chemical step at the shrinking reaction surfaces within the grains (74). (Refer to Appendix 13 for additional details.)

The differential mass balance equation 4.2, is solved twice; once for the individual grains and a second time for a single pellet consisting of the grains.

$$\frac{\partial C_A}{\partial t} + \nabla \cdot \underline{v} C_A = D_e \nabla^2 C_A + R_A \qquad 4.2$$

To obtain the grain model kinetic equations, the assumptions listed in Table 4.1 are made. Most of these assumptions are applicable to this work with the exception of the requirement of no change in solid structure. The detailed analysis and resulting equations can be found in reference 74.

Three additional assumptions are required for the packed bed system:

(1) The plug flow of gas.
(2) Uniform spherical pellets.
(3) Negligible diffusive or dispersive mass transfer in the axial direction.

The following differential material balance was obtained by Evans and Song (78):

$$\frac{\partial \theta}{\partial y^*} = \frac{dX}{dt} = \theta\beta \qquad 4.3$$

with the boundary condition

$$X = 0 \text{ at } t^* = 0, \quad y^* \geq 0 \qquad 4.4$$

where $\theta = C/C_o$ = dimensionless gas concentration external to the pellet (this allows for variations in the concentration of the bulk gas as it passes through the reactor).

C = gas concentration at the pellet surface
C_o = inlet gas concentration
X = solid conversion
y^* = dimensionless length (defined by eqn. 4.6)
β = effectiveness factor.

Table 4.1 Assumptions in Grain Model

	Assumption	Validity
(1)	The pseudo-steady state approximation can be used to describe the concentration of the gaseous reactant within the pellet (i.e $\partial C_A/\partial t = 0$)	Valid since the diffusion of gaseous species has been found to be 1000 times faster than the progression of the reaction front (74).
(2)	The resistance due to external mass transfer is negligible.	This study used a modified version of the grain model given by Wang (80) which incorporates a bulk diffusion correction factor.
(3)	Diffusion within the pellet is either equimolar counter diffusion or is at a low concentration of the diffusing species.	Concentrations of H_2S were less than 1.0% by volume. Moles of gaseous reactants and products are equal (see section 3.3.2). Thus assumption is valid.
(4)	The system is isothermal.	Valid because H_2S concentrations were low and because enthalpies of reaction are weakly endothermic ($\Delta H° = 4.45 - 26.48$ kJ/mol).
(5)	The viscous flow contribution to mass transport in the pores may be neglected ($\nabla \cdot \underline{v} C_A = 0$).	This term accounts for the mass added to the system in continuous flow problems. Valid assumption.
(6)	The reaction rate is first order with respect to the gaseous concentration. $R_A = k C_A$	This may or may not be valid.
(7)	The solid structure consists of macroscopically uniform non-porous grains which are unchanged by reaction.	SEM micrographs showed the CeO_2 sorbent to consist of uniform spherical grains. However the solid structure does undergo a large change in porosity during reaction (see Appendix 6). Thus this assumption is not valid.

The dimensionless time, t^*, is defined as

$$t^* = \left| \frac{k C_o A_g}{\rho_s F_g V_g} \right| t \qquad 4.5$$

where k = intrinsic kinetic rate constant

A_g = external surface area of the grain

F_g = shape factor for the grain

V_g = volume of the grain

ρ_s = molar density of the solid reactant

t = time

The dimensionless length, y^*, is defined as

$$y^* = \frac{k A_g (1-\varepsilon_p)(1-\varepsilon_v) y}{F_g V_g v_o} \qquad 4.6$$

v_o = superficial gas velocity

ε_v = bed void fraction

ε_p = void fraction in pellet

y = distance from inlet end of reactor

β is defined as the effectiveness factor and is given by the value of dX/dt^* when $\theta = 1$. β values, determined by Evans and Song (78) using numerical methods, are given in Table 4.2 for a spherical pellet consisting of spherical grains (i.e. $F_p = F_g = 3$). Note that β is a function of F_p, F_g, X and $\hat{\theta}$, where the reaction modulus, $\hat{\theta}$, is defined by

$$\hat{\theta} = \frac{V_p}{A_p} \sqrt{\frac{F_p k (1-\varepsilon_p) A_g}{2 D_e F_g V_g}} \qquad 4.7$$

and D_e = effective diffusivity

V_p = volume of pellet

A_p = external surface area of the pellet

Table 4.2: Values of Effectiveness Factor, β, for spherical pellets consisting of spherical grains ($F_p = F_g = 3$) (78).

Extent of reaction X	$\hat{\theta}$					
	0.3	0.5	0.8	1.2	1.8	3.0
0.00	2.72	2.37	1.88	1.42	1.02	0.653
0.05	2.63	2.30	1.82	1.38	0.984	0.614
0.10	2.55	2.23	1.77	1.33	0.942	0.575
0.15	2.46	2.16	1.71	1.28	0.898	0.533
0.20	2.37	2.08	1.65	1.23	0.853	0.490
0.25	2.28	2.01	1.59	1.18	0.806	0.444
0.30	2.18	1.93	1.53	1.13	0.758	0.396
0.35	2.08	1.85	1.47	1.07	0.707	0.347
0.40	1.98	1.76	1.40	1.02	0.655	0.297
0.45	1.88	1.68	1.33	0.959	0.600	0.251
0.50	1.77	1.58	1.26	0.898	0.542	0.213
0.55	1.65	1.49	1.19	0.833	0.482	0.182
0.60	1.54	1.39	1.11	0.765	0.442	0.155
0.65	1.41	1.28	1.02	0.693	0.361	0.132
0.70	1.28	1.17	0.930	0.617	0.306	0.112
0.75	1.14	1.04	0.832	0.535	0.257	0.0941
0.80	0.986	0.909	0.724	0.448	0.212	0.0779
0.85	0.819	0.760	0.603	0.357	0.170	0.0626
0.90	0.629	0.587	0.461	0.265	0.129	0.0477
0.95	0.399	0.374	0.284	0.166	0.0843	0.0319
0.99	0.137	0.124	0.0877	0.0581	0.0340	0.0144

F_p = shape factor for the pellet

The reaction modulus indicates the relative importance of kinetics and diffusion in the overall reaction rate. The reaction is primarily kinetically controlled for values of $\hat{\theta}$ less than 0.3 and is diffusion-controlled for values of $\hat{\theta}$ greater than 3.0 (74).

Values of β outside the range of tabulated values may be approximated by an equation provided by Evans and Ranade (79):

$$\beta = \left\{ \frac{1}{F_g}(1-X)^{1/F_g - 1} + 2\hat{\theta}[(1-X)^{-1/3} - 1] + (0.21 - 0.62X) \right.$$

$$\left. (1+\hat{\theta}^2)\exp[-0.9(\ln(\hat{\theta}/1.08))^2] \right\}^{-1} \qquad 4.8$$

4.2 Constant Pattern Grain Model Kinetic Equations

This section reviews a simplified grain model kinetic analysis given by Wang (80). Since the rate constant k_s always appears with the term $F_g V_g/A_g$ (equivalent to the grain radius), a new rate constant parameter k, can be defined such that:

$$k = k_s \left| \frac{A_g}{F_g V_g} \right| (1-\varepsilon_p) \qquad 4.9$$

Substituting k into the original equations for t^*, y^* and $\hat{\theta}$ yields:

$$t^* = \frac{k C_0}{\rho_s} t \qquad 4.5a$$

$$y^* = \frac{k(1-\varepsilon_v)y}{v_0} \qquad 4.6a$$

$$\hat{\theta} = \frac{V_p}{A_p} \sqrt{\frac{k F_p}{2 D_e}} \qquad 4.7a$$

where $\rho_s = \rho_s (1-\varepsilon_p)$

If it is assumed that, after an initial period, the reaction front develops a sigmoid shape which moves through the fixed bed unchanged at a constant velocity, the analysis is greatly simplified. Under these conditions, the relationship between gas and solid at any given point in the bed is

$$\theta = X \tag{4.10}$$

This is called the "constant pattern" solution. Thus equation 4.3 becomes:

$$\frac{dX}{dt^*} = \frac{d\theta}{dt^*} = \beta X \tag{4.11}$$

A discussion of the assumptions and the mathematical development is given in Appendix 12. Note that $(d\theta/dt^*)$ gives the slope of the breakthrough curve and it is also equal to the rate of reaction (dX/dt^*) through equation 4.11. If a dimensionless throughput parameter, ι, is defined such that:

$$\iota = \frac{t^*}{y_b^*} \tag{4.12}$$

where

$$y_b^* = \frac{k(1-\varepsilon_v)y_b}{v_o} \quad \text{(see eq'n 4.6a)}$$

y_b = the total bed length

equation 4.11 becomes:

$$\frac{d\theta}{d\iota} = \beta X y_b^* \tag{4.13}$$

The bed length, y_b, superficial velocity, v_o, and bed void fraction, ε_v, can be easily measured. The slope of the breakthrough curve $(d\theta/d\iota)$ at a particular value of X can be obtained from plots of θ versus ι. Thus, values of βk for each experiment can be obtained and compared.

When external mass transfer is not negligible, Wang showed that a modified effectiveness factor β' replaces β in equations 4.11 and 4.13 where:

$$\frac{1}{\beta'} = \frac{1}{\beta} + \frac{2\theta^2}{Sh'} \tag{4.14}$$

$$Sh' = \text{Sherwood number} = \frac{k_f F_p V_p}{D_e A_p}$$

k_f = local mass transfer coefficient.

Combining the Sherwood number with equation 4.7a yields:

$$\frac{1}{\beta'} = \frac{1}{\beta} + \frac{k V_p}{k_f A_p} \qquad 4.15$$

Therefore βk is given by:

$$\beta' k = \left| \frac{1}{\beta' k} - \frac{V_p}{k_f A_p} \right|^{-1} \qquad 4.16$$

Thus, slopes obtained from the breakthrough plots of θ versus t, give values of $\beta' k$ where

$$\beta' k = \left(\frac{d\theta}{dt} \right) \frac{v_o}{X(1-\varepsilon_p) y_b} = \left(\frac{d\theta}{dt} \right) \frac{\rho_s (1-\varepsilon_p)}{C_o X} \qquad 4.17$$

(refer to Appendix I-I for derivation of eqn. 4.17) which can be converted to values of βk using equation 4.16. Note that the mass transfer coefficient, k_f, needs to be known in order to calculate βk.

4.3 Estimation of the External Mass Transfer Coefficient

Figure 4.2 illustrates the correlation of the external mass transfer coefficient, k_m,[1] with increasing Peclet numbers ($v_o d_p / D_L$) for low Reynolds number (< 5) compiled by Fedkiw (81). In the high Pe region, the k_m values correlate with the cube root of velocity and good estimates of the mass transfer coefficient can be obtained using the relationship:

---

(1) k_f relates the local concentration driving force to the local transfer rate, whereas, k_m is based on the averaged inlet and outlet concentration driving force. The values of k_f and k_m are identical for high Pe numbers.

$$\frac{\varepsilon_v k_m d_p}{D_f} = 1.09 \left| \frac{v_o d_p}{D_f} \right|^{1/3} \qquad 4.18$$

In the low Pe region, axial dispersion becomes important and equation 4.18 overestimates the mass transfer coefficient. In this region, k_m is proportional to the velocity as illustrated in Figure 4.2.

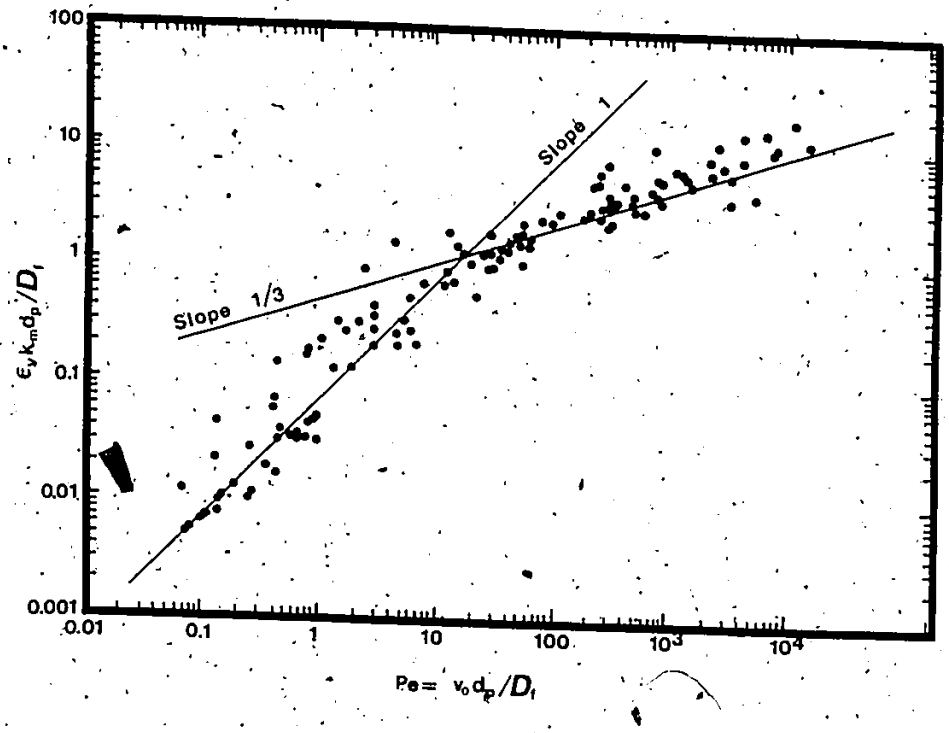

Figure 4.2: Mass-Transfer Coefficients in Packed Beds for Low Reynolds Numbers (compiled by Fedkiw (81)).

Chapter V

EXPERIMENTAL METHOD

5.1 Description of Apparatus

A schematic diagram of the experimental system is illustrated in Figure 5-1. The reactor, shown in Figure 5-2, consisted of a quartz U-tube (64 cm x 1.2 cm o.d.); the inlet side of the tube provided a preheating zone for gases which were metered through calibrated rotameters. A 100 mesh stainless steel screen supported the sorbent 15 cm from the bottom of the tube and the height of the assembly was adjusted such that the packed region of the reactor was within the constant temperature zone of the furnace. The temperature was measured with a chromel/alumel thermocouple, suspended just outside the mid-section of the fixed bed. Heat losses were minimized by the use of a circular piece of firebrick, inserted in the bottom of the furnace, and by the use of Fiberfrax insulation at the top. Reactor effluent travelled through teflon gas lines to the gas analysis system described in section 5.3.

5.2 The Gas Flow System

The gas flow system consisted of gas cylinders, needle valves for controlling flow rates, and calibrated rotameters. Three-way valves were used to select the desired gas stream entering the fixed bed reactor, which operated at essentially atmospheric pressure. The system was flushed with nitrogen during heating, cooling and between changes of gas streams. Five percent hydrogen in nitrogen was used for pre-reducing the sorbent. Desulfurization experiments were carried out with a simulated coal gas containing CO, CO_2, H_2 and H_2S. Regeneration experiments were conducted in air.

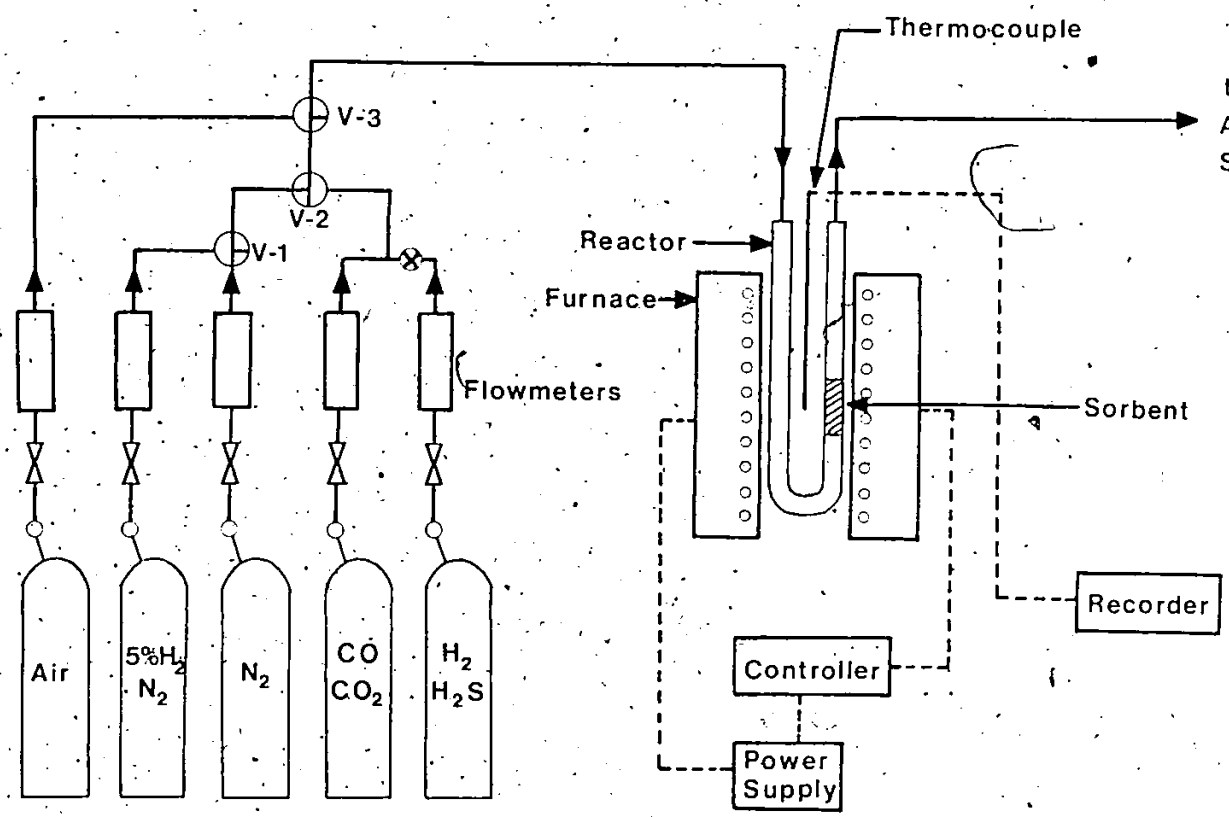

Figure 5.1: Schematic Diagram of Experimental System

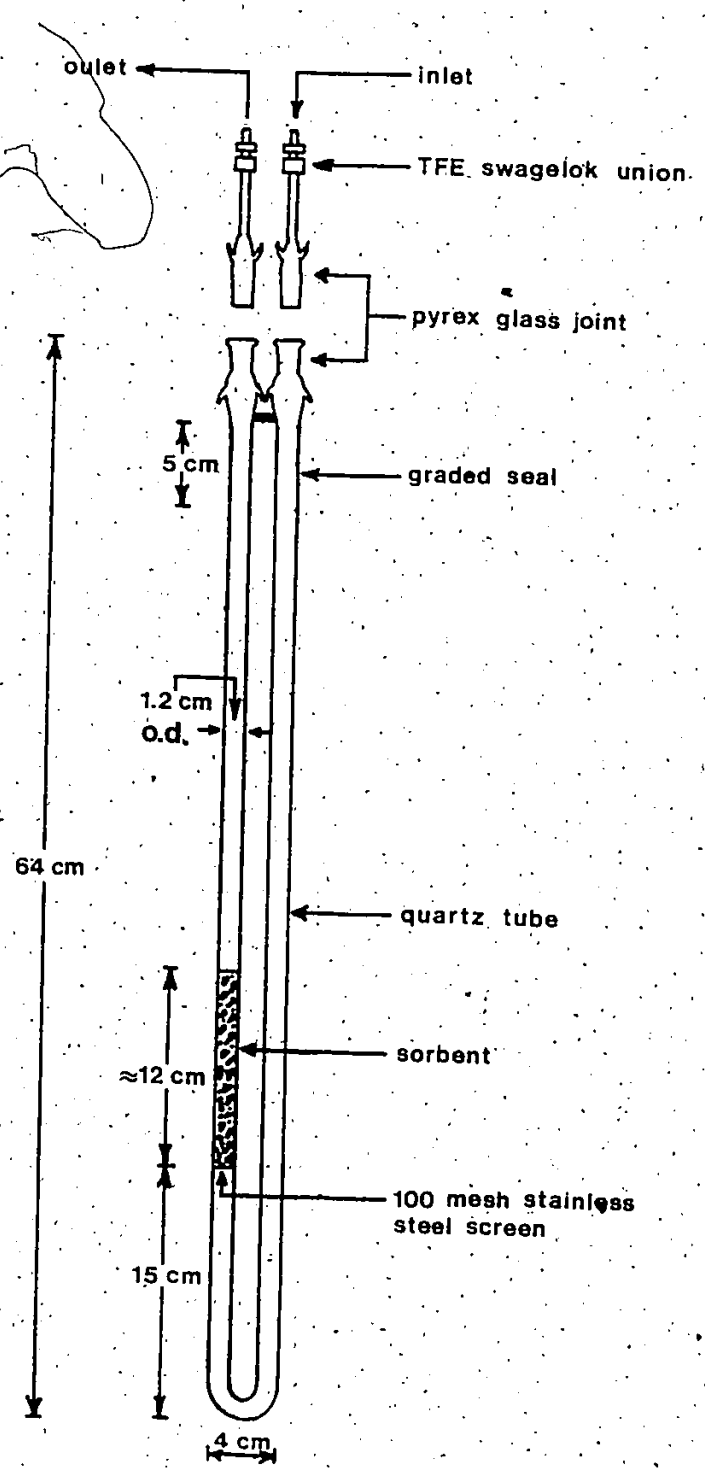

Figure 5.2: Schematic Diagram of Reactor

A simulated coal gas containing 55.0% CO, 33.0% H_2, 10.8% CO_2 and 1.2% H_2S by volume, was used for preliminary desulfurization experiments. However, the H_2S content of this gas mixture, following breakthrough, was above the analytical capability of the flame photometric gas chromatograph. In subsequent desulfurization experiments, two gas streams were blended: one containing 91.9% CO and 8.1% CO_2, the other 99.0% H_2 and 1.0% H_2S, by volume. The proportions of these gases could be altered without significantly changing the oxygen and sulfur potentials of the inlet gas. The CO/CO_2 gas mixture could also be used to pre-reduce the sorbent. The computer program described in Appendix 2 was used to determine the composition of the simulated coal gas at conditions prevailing in the reactor prior to desulfurization (see section 3.2).

5.3 Gas Analysis System and Calibration

A schematic diagram of the gas analysis system is given in Figure 5.3. Effluents from desulfurization and regeneration experiments were analyzed by a Hewlett Packard 5830A gas chromatograph, equipped with a flame photometric detector (FPD) and a teflon column (46 cm x 0.3175 cm o.d.; 18" x 1/8" o.d.) packed with acetone washed poropak QS. Detector gas flow rates were adjusted to the recommended values for sulfur gas analysis (H_2 50 mL/min, O_2 10 mL/min, air 50 mL/min) with the helium carrier gas flow rate between 25-35 mL/min. The g.c. was controlled by an HP data system which also processed peak data.

Samples were introduced into the chromatograph via a Valco 6-port Hastalloy C automatic gas sampling valve (see V-5, Figure 5-3). All sample loops and gas lines, downstream from the reactor, were constructed of FEP teflon and joined with teflon or stainless steel swagelok fittings (the former being preferable unless the fitting was in a heated zone).

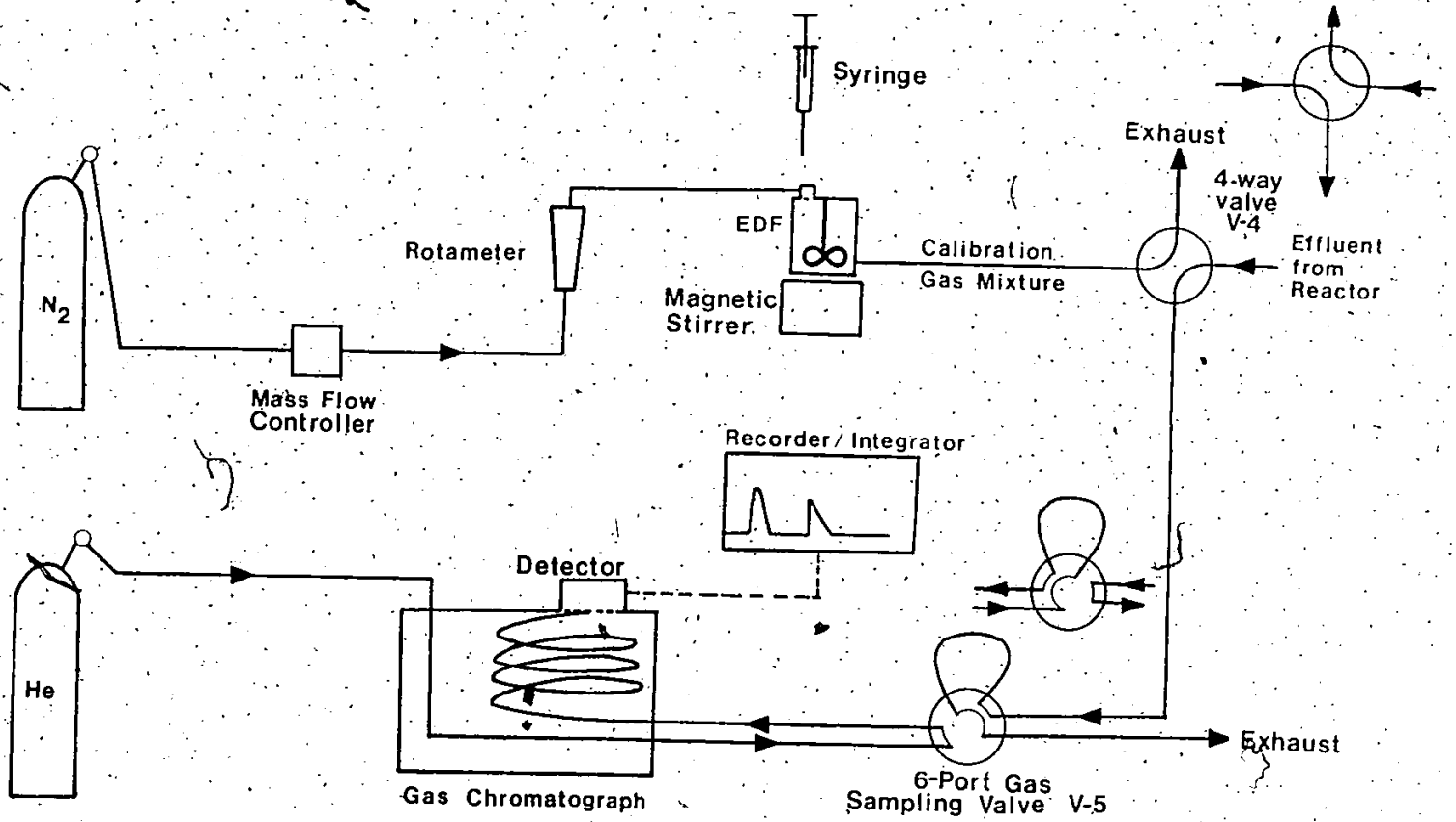

Figure 5.3: Schematic Diagram of Gas Analysis System

To calibrate the gas chromatograph for a given sample loop size, 30.0 to 150.0 μL of C.P. grade H_2S were measured with a gas tight syringe and injected into an exponential dilution flask (EDF) constructed entirely of teflon. Details of the flask construction and application are described in the literature (66,71). Equations 5.3.1 and 5.3.2 were used to calculate concentrations of H_2S in the EDF effluent stream as a function of time (injection of H_2S into the flask defines t = 0).

$$C = C_i \exp(-Ut/V) \qquad 5.3.1$$

$$C_i\,(\text{as ngS/mL}) = \frac{32000}{24.5}\left(\frac{\mu\text{L } H_2S \text{ injected}}{V}\right) \qquad 5.3.2$$

where

C = H_2S concentration of EDF effluent at time t

C_i = initial concentration of H_2S in EDF (at t = 0)

U = volumetric flow rate of nitrogen in mL/min (refer to Figure 5.3)

t = time in minutes after injection of H_2S into EDF

V = volume of EDF (215.0 mL for this flask).

EDF effluent was sampled at 2.0 minute intervals with the automatic gas sampling valve V-5. A typical calibration curve for a 0.5 mL sample loop is illustrated in Figure 5.4. (Refer to Appendix 3 for procedure and detailed calculations.) Reproducibility was good provided detector conditions remained constant. Figure 5.4 illustrates the strong dependence of detector sensitivity upon detector gas flow rates. Because it was impossible to adjust the detector to the same conditions each time the gas chromatograph was shut down and started up again, calibration curves needed to be generated each time.

The four way valve V-4 (see Figure 5.3) was used to select either calibration effluent or reactor effluent for gas analysis.

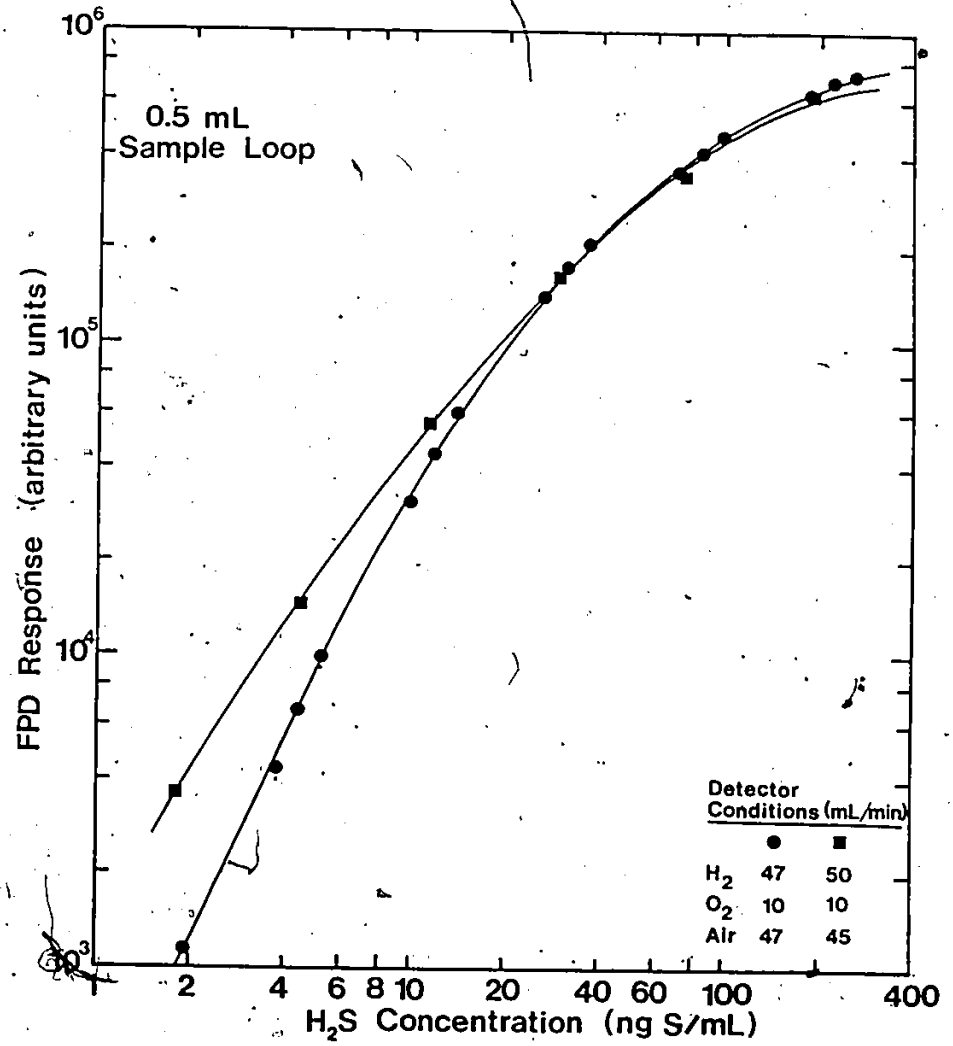

Figure 5.4: Typical Calibration Curve

5.4 Sorbent Preparation and Analysis

Three types of solids were used for desulfurization/regeneration studies;

1) Bastnaesite concentrates (4000C and 4100)
2) Cerium oxide
3) Supported Cerium oxide.

The preparation and characterization of these solids are described below.

5.4.1 Bastnaesite Concentrates

Four commercially available bastnaesite concentrates were obtained from Union Molycorp Inc. in powder form (d_p = 1-65 μm dia.). The nominal compositions are given in Table 5.1. Although the components are listed as oxides, the elements are not present in this form (see section 6.1.1). The elemental analyses of the concentrates were performed by direct current argon plasma emission spectroscopy and are presented in Tables A4.3 and A4.4 of Appendix 4. X-ray powder diffraction patterns of the uncalcined concentrates, 4000 and 4010, confirmed the presence of bastnaesite as a major component (see Table A4.1 of Appendix 4). The diffraction patterns of the calcined concentrates, 4000 C and 4100, are discussed in Section 6.1.1. TGA/DTA experiments were conducted on concentrates taken directly from the manufacturer's container, or on samples dried at 130°C, or on samples calcined at 1000°C.

Table 5.1: Bastnaesite Concentrates - Typical Composition - % by Weight

		# 4000	# 4010	# 4100
Total	Re Oxides*	55-60	68-72	85-90
	SrO	6.0	1.0	1.2
	CaO	5.0	0.4	0.5
	BaO	1.5	1.8	2.2
	F	4.0	5.0	6.0
	SiO_2	0.4	0.4	0.6
	Fe_2O_3	0.5	0.5	0.6
	P_2O_5	0.9	1.0	1.2
	MgO, Na_2O, K_2O (each)	<0.5	<0.5	<0.5
	ThO_2	<0.1	<0.1	<0.1
	Loss on ignition (CO_2)	24.0	20.0	

*Contained RE, expressed as oxides:

Oxides	%
CeO_2	48-50
La_2O_3	32-34
Nd_2O_3	13-14
Pr_6O_{11}	4-5
Sm_2O_3	0.5
Gd_2O_3	0.2
Eu_2O_3	0.2
Other	0.2

5.4.2 Cerium Oxide

Twenty grams of calcined cerium dioxide (99.9% purity, optical grade, -325 mesh, 1.03 m^2/g, Cerac Inc.) were mixed with 6.0 g of warm starch solution (10 g soluble starch dissolved in 310 mL boiling water) in order to prepare hand-rolled green pellets for preliminary desulfurization/regeneration experiments. These pellets were dried at 120°C overnight and subsequently sintered at 1250°C or 1400°C for 4 hours. The sintered material had the following properties:

Sintering Temperature	1250°C	1400°C
B.E.T. surface area	0.45 m^2/g	-
average pore radius	1.68×10^{-5} cm	-
porosity	29.0%	11.4%

Some of the sintered pellets were crushed and sieved for fixed bed desulfurization/regeneration studies. Fractions at -0.297/+0.210 mm (-50/+70 mesh) and -0.841/+0.595 mm (-20/+30 mesh) were used for this purpose.

5.4.3 Supported Cerium Oxide

Supported cerium dioxide pellets were prepared by impregnating type SAHT-96 fused aluminum oxide (supplied by Carborundum, 95.95% Al_2O_3, balance SiO_2) with 99.0% ammonium cerium (IV) nitrate. Physical properties of the support are given below:

surface area	0.74 m^2/g
pore volume	60%
average pore size	2 µm
bulk density	1.51 g/cm^3
particle size	-2.00/+1.68 mm (-10/+12 mesh).

To prepare a sorbent containing 14.3wt % CeO_2, 12.74 g of $Ce(NH_4)_2(NO_3)_6$ (previously dried at 120°C) was dissolved in 10.0 g of water. Twenty-eight grams of the high porosity support was exposed to the solution for 16 hours, dried at 120°C and calcined at 1000°C for 2 hours. Fines were removed by resieving the calcined sorbent.

5.5 Experimental Procedure

An experiment consisted of weighing approximately 15 g of sorbent; recording the weight and loading the solid into the reactor with a vibrator to eliminate channels in the bed. The height of the fixed bed was recorded and silica wool was placed over the sorbent to hold the bed in place. This also prevents fine solid particles from entering the gas analysis system. Gas flow rates were adjusted to the desired values before the reactor was connected; nitrogen was flushed through the system while the reactor heated to the set point temperature. The sorbent was reduced with 5% H_2 in nitrogen overnight and was subsequently flushed with nitrogen for 15 minutes.

To begin the desulfurization experiment, the simulated coal gas was introduced into the reactor through valve V-2 (see Figure 5.1), while simultaneously initiating the HP control data system. The time delay between valve V-2 and the gas sampling valve V-5 (refer to Figure 5.3) was measured for the flow rates used in these experiments and the desulfurization breakthrough curves were appropriately corrected. Reactor effluent was sampled at 2.0 minute intervals, until the entire breakthrough curve was generated. A typical trace from a desulfurization run is given in Appendix 10. Prior to breakthrough, 0.5 to 5.0 mL sample loops were used to determine H_2S concentrations. The remainder of the curve was obtained with a 1/16 mL sample loop.

Before air was introduced into the reactor to regenerate the sorbent, nitrogen was flushed through the system for 30 minutes. The initial section of the regeneration curve was

obtained with a 1/16 mL sample loop at 2.5 minute intervals. After the SO_2 concentration dropped below 13 ngS/mL (approximately 10 ppm), a 1.0 mL sample loop was used. A trace from a typical regeneration run is also given in Appendix 10. The regenerated sorbent was used for several desulfurization/regeneration cycles.

To carry out a differential thermal analysis, about 50 mg each, of sample and reference alumina, are placed in similar platinum capsules resting on the tips of a vertical differential thermocouple. An outer alumina tube isolates the samples from the external environment. The temperature inside the alumina block is measured with a second thermocouple in a separate cavity between the vertical wells holding the sample and reference. Analyses were done in air, in carbon monoxide, or in a gas mixture containing 91.9% CO/ 8.1% CO_2, by volume.

During an experiment, both sample and alumina are heated at a constant rate (between 10 - 20°C/min) to a final temperature. Alumina does not undergo any reactions. When an endothermic reaction occurs in the sample, a negative peak is recorded on the chart because the sample is cooler than the reference alumina. The opposite is observed for an exothermic reaction. A solid such as LaOF, which transforms from the rhombohedral to the fluorite form at 505°C and does not undergo any chemical reactions, can be used to calibrate the horizontal temperature axis of the instrument. A thermogravimetric analysis is similar, except that weight changes are measured as a function of temperature.

Chapter VI

RESULTS AND DISCUSSION

6.1 Bastnaesite Concentrates as Desulfurizing Agents

An outline of the following discussion is given in Figure 6.1. The five sub-sections which follow, deal with the characterization of bastnaesite concentrates, their behaviour in reducing and moist environments and their desulfurization/regeneration characteristics. Further discusssion of the desulfurization/regeneration reactions is given in section 6.2 for cerium oxide sorbents.

6.1.1 Characterization

To understand how bastnaesite works as a desulfurizing agent, it is important to know the chemical composition of the mineral, and to determine how this composition changes during the various processing stages.

The four bastnaesite concentrates discussed in this study, were produced by Union Molycorp Inc. (refer to Table 6.1) from ore bodies located in the Mountain Pass district of California. The elemental analysis is given in Table A4.3 of Appendix 4.

Table 6.1: Commercially Available Bastnaesite Concentrates (85)

Concentrate	Method of Preparation
4000	froth flotation of ore
4010	HCl leaching of concentrate 4000 to remove Ca, Sr
4000C	calcination of 4000
4100	calcination of 4010

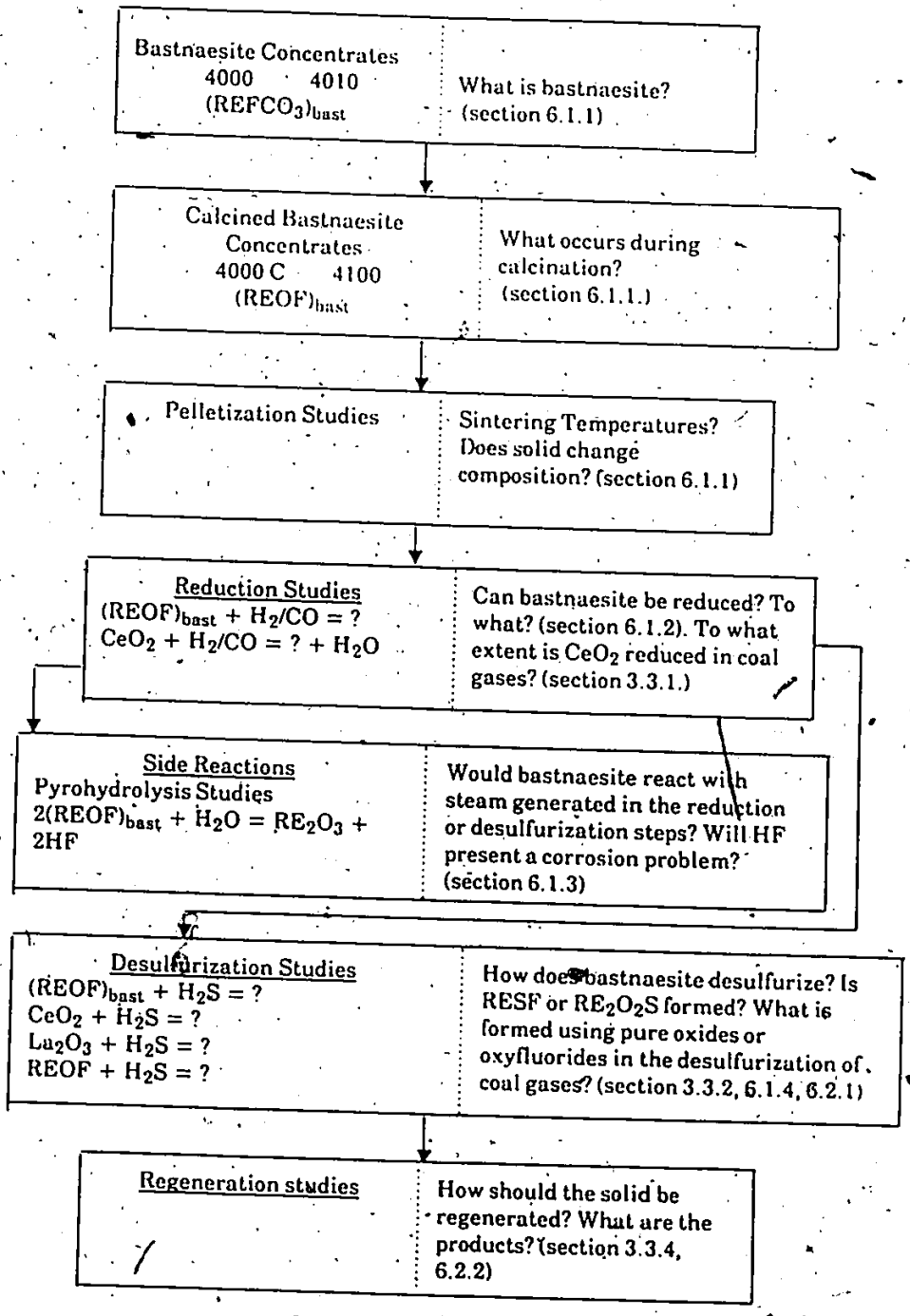

Figure 6.1: Program for the Study of the Desulfurization of Coal Gases using Bastnaesite Concentrates

Although bastnaesite has been described by the chemical formula $REFCO_3$, the actual composition is variable and difficult to define. Single crystals of this mineral rarely occur and many specimens are syntaxic intergrowths (82, 83) of two or more related minerals of the type $xREFCO_3 \cdot yCaCO_3$; bastnaesite ($x = 1, y = 0$), parasite ($x = 2, y = 1$), roentgenite ($x = 3, y = 2$), and synchisite ($x = 1, y = 1$). Every pair has been observed except bastnaesite-synchisite. Donnay and Donnay (82) reported the crystal structure of bastnaesite as alternating sheets of carbonate ions and rare earth-fluoride ions, the latter arranged alternately at the vertices of a regular hexagon. Layers of calcium ions (A) alternate with layers of rare earth-fluoride ions (B) in differing sequences for the related minerals; parasite-ABBABB-; roentgenite - ABABBABABB-; synchisite - ABAB-. Other minerals that are often associated with bastnaesite are cerite, barite, strontianite, calcite, quartz, chalcedony, galena and acmite (84).

X-ray powder diffraction patterns (see Appendix 4, Table A4.1) of the uncalcined concentrates, 4000 and 4010, agree well with literature values given by Glass et al. (84). The associated minerals are probably responsible for the additional lines, since some of the lines disappear when the calcium and strontium are leached out to produce the 4010 concentrate.

Concentrates 4000C and 4100 are formed by the calcination of concentrates 4000 and 4010, respectively. During this process, the rare earth fluorocarbonates decompose to the oxyfluorides according to reaction 6.1.1:

$$REFCO_3(s) = REOF(s) + CO_2(g) \qquad 6.1.1$$

The X-ray powder diffraction patterns of these concentrates will be discussed later in this section.

Percentages of $REFCO_3$ and REOF in the uncalcined and calcined concentrates, respectively, can be theoretically estimated from the chemical analysis provided in Table A4.3. However, these calculations revealed that the molar ratio of the fluorine to total rare

earth content is less than the 1:1 ratio required by stoichiometry (refer to Appendix 4). Only $57 \pm 1\%$ of the rare earth content of concentrate 4000 is present as the fluorocarbonate. Similarly, $56 \pm 1\%$ of concentrate 4100 is present as the oxyfluoride. Thus, the formulas $REFCO_3$ and REOF do not accurately describe the compositions of the uncalcined and calcined concentrates, respectively.

This work proposes that the uncalcined concentrates consist of a mixture of $RE(OH)CO_3$ and $REFCO_3$ which decompose to a mixture of CeO_2 and REOF upon calcination. Evidence for this hypothesis is provided by a study published by Haschke in 1975 (86). It was shown that fluoride ions could be quantitatively substituted in $La(OH)CO_3$ for $La(OH)CO_3$: F ratios in the range $0 < x < 3$. For $x \leq 1$, hydroxide replacement by fluoride results in the formation of a continuous solid solution $La(OH)_{1-x}F_xCO_3$, across the entire composition range to $x = 1$. At the $La(OH)_{0.25}F_{0.75}CO_3$ composition, only superstructure lines characteristic of bastnaesite are detectable. In the middle of the miscibility range, a high level of disorder is indicated by broadened diffraction lines. At the $La(OH)_{0.75}F_{0.25}CO_3$ composition, an orthorhombic $La(OH)CO_3$-type superlattice is observed. The gradual structural transition from an $La(OH)CO_3$-type to an $LaFCO_3$-type lattice suggested to Haschke that micro-domains of the two phases are coherently intergrown in the $La(OH)_{1-x}F_xCO_3$ phase. Thermogravimetric studies of these compounds were also done. Between 425 and 525°C, the hydroxide carbonate loses H_2O and CO_2 to form $La_2O_2CO_3$, which subsequently decomposes to La_2O_3 between 625 and 800°C. The $LaFCO_3$ phase decomposes between 520 and 550°C with the formation of LaOF. Pyrolysis of $La(OH)_{1-x}F_xCO_3$ produces a mixture of the dioxide monocarbonate and oxide halide. Presumably, at higher temperatures, a mixture of the oxide halide and oxide would be obtained.

X-ray powder diffraction patterns of the calcined concentrates (see Table A4.2, Appendix 4) agree remarkably well with the diffraction pattern of EuOF at 800°C. Since the

solid obviously cannot be EuOF, the crystal structure, cell dimensions and atom sizes must be similar. REOF phases for RE = La through Er and including Y, are known to have identical fluorite-related rhombohedral structures at low temperatures which transform to the cubic fluorite-type structure at high temperatures (83,87). For example, LaOF transforms to the fluorite form at 505°C (88,89). The dioxides of cerium and praseodymium also crystallize in the face-centered cubic fluorite-type structure. If two or more components crystallize in the same structure type, the mixed system forms a solid solution of the same structure over the whole range of composition and Végard's law (a linear relationship between lattice parameter and composition) should apply (87). A solid solution of CeO_2 and REOF could give rise to the observed diffraction pattern for the 4100 concentrate. Not only are the scattering powers of the rare earths similar, but oxygen and fluorine are difficult to distinguish by X-ray methods for the same reason. A combination such as REOF and La_2O_3 was ruled out because lanthanum oxide exists in the hexagonal form below 2000°C. Other rare earth oxides are present in small quantities (see analysis, Appendix 4) and thus can be neglected.

The following DTA and TGA studies were undertaken to determine how the calcination process affects the chemical compositions of the bastnaesite concentrates.

DTA's of bastnaesite concentrates 4000, 4000C, 4010 and 4100 are presented in Figure 6.2. Below 300°C, physically bound water is desorbed. DTA's of concentrates, previously dried at 130°C overnight (eg. concentrate 4010 in Figure 6.2), confirmed this conclusion. Bastnaesite 4000, the flotation concentrate, decomposes endothermically in two stages, at 350-550°C and 750-850°C (see Table 6.2 for reactions). The former temperature range corresponds to the decomposition of the rare earth carbonates, $RE(OH)CO_3$ and $REFCO_3$, whereas the latter temperature range corresponds to the decomposition of $RE_2O_2CO_3$ and calcite. Thus, as expected, the uncalcined leached concentrate, 4010, has a major decomposition peak at 350-550°C, whereas, minor peaks are obtained for the calcined

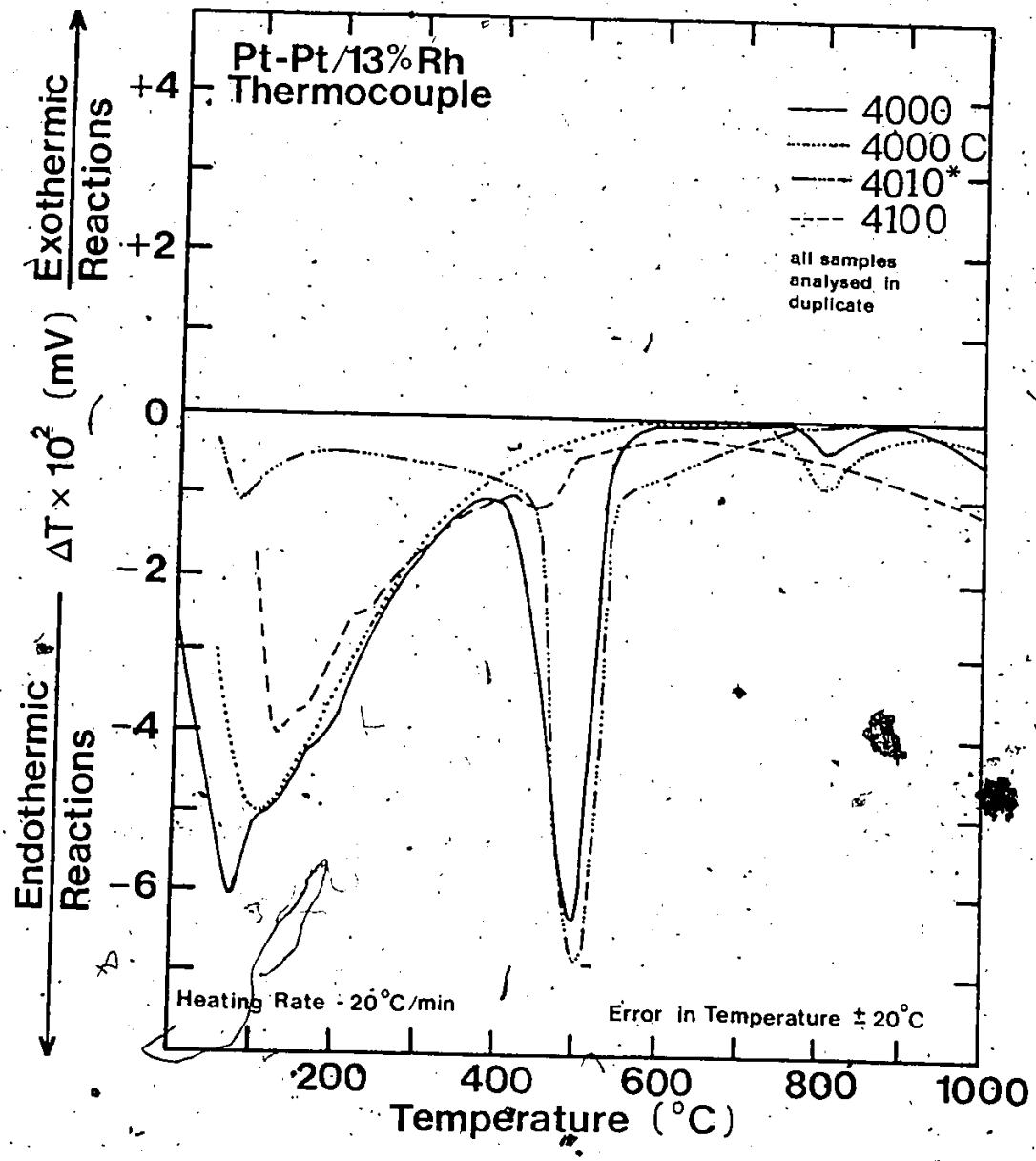

Figure 6.2: Differential Thermal Analyses of Bastnaesite Concentrates. Using the Dupont Thermal Analyser. (*previously dried at 130°C)

Table 6.2: Decomposition Temperature Ranges of Lanthanum and Calcium Carbonates (86,90)

Reaction	Temperature Range (°C)
$LaFCO_3(s) = LaOF(s) + CO_2(g)$	520-550
$La(OH)CO_3(s) = 1/2\ La_2O_2CO_3(s) + 1/2\ CO_2(g) + 1/2\ H_2O(g)$	425-525
$La_2O_2CO_3(s) = La_2O_3(s) + CO_2(g)$	625-800
$CaCO_3(s) = CaO(s) + CO_2(g)$	825-900

Table 6.3: Theoretical Weight Losses of Rare Earth Carbonate Mixtures

Composition of Solid	% Weight Loss < 600°C	% Weight Loss > 600°C	Total wt. % LOI
100% $La(OH)CO_3$	14.4	10.2	24.6
43% $La(OH)CO_3$ 57% $LaFCO_3$	17.66	4.39	22.05
17% $La(OH)CO_3$ 83% $LaFCO_3$	19.20	1.73	20.93
100% LaOF	20.20	0.0	20.20

Table 6.4: Measured Weight Losses for Bastnaesite Concentrates by TGA

Concentrate	%wt. loss <600°C		%wt. loss >600°C		Total wt. % lost
	Experimental	Theoretical*	Experimental	Theoretical*	
4000	15.08±0.06†	14.57±0.98	3.61±0.3	3.58±0.3	18.69±0.03
4000C** (calcined)	1.57±0.33 1.68±0.33	0.0	4.57±0.11 4.65±0.11	0.0	6.14±0.11 6.33±0.11
4010 (leached)	16.52±0.06	16.33±0.98	0.0	4.31±0.3	16.52±0.03
4100 (leached, calcined)	1.55±0.13	0.0	0.0	0.0	1.55±0.13

* Theoretical values were calculated using the elemental analyses reported in Appendix 4. A sample calculation is given on page 151. In this table, weight loss contributions from the decomposition of calcite are not included. The error bars on the theoretical weight losses reflect the errors associated with the chemical analysis.

† The error bars listed for the experimental weight losses are associated with the measurement error which is a function of sample size, heating rate, chart recorder settings and background noise.

** Sample analysed in duplicate.

concentrates, 4000C and 4100. TGA data support DTA results and show that the calcined concentrates lose $1.56 \pm 0.33\%$ by weight, owing to the presence of residual rare earth carbonates (see Table 6.4). The experimentally measured weight-losses given in Table 6.4 are comparable to the theoretical values within the range of measurement errors. This confirms previous calculations which indicate that the uncalcined bastnaesite concentrates consist of a mixture of $REFCO_3$ and $RE(OH)CO_3$.

Table 6.4 shows that concentrates 4000 and 4000C, have large decomposition peaks above 750°C. Since calcite is known to decompose in this temperature range, an additional weight loss contribution from this associated mineral is expected for concentrate 4000. The large weight loss obtained for the calcined concentrate, 4000C, indicates that the calcination process was incomplete. The absence of a small decomposition peak above 750°C, for concentrate 4010, cannot be explained.

Figure 6.2 shows that, above 900°C, the chemical composition remains constant. This was confirmed by X-ray powder diffraction of a sample heated to 1300°C (see Table A4.2 of Appendix 4). However, the concentrates should be used below 1100°C to avoid significant loss of surface area due to sintering (13).

Conclusions from the characterization studies are summarized below:

(1) The uncalcined bastnaesite concentrates used in this work, consist of a rare earth hydroxyfluorocarbonate, $RE(OH)_{1-x}F_xCO_3$ where the value of x is 0.57 ± 0.01.

(2) $RE(OH)_{1-x}F_xCO_3$ decomposes endothermically from 400-550°C and 800-900°C to a solid solution of oxides and oxyfluorides. This is comparable to the decomposition range of $La(OH)CO_3$ (425-525°C and 800°C) and $LaFCO_3$ (520-550°C)

(3) Above 900°C, further changes in chemical composition are not expected. The calcined concentrates have a fluorite type structure and consist of a solid solution of

REOF and CeO_2. The percentage of rare earth oxyfluorides in concentrate 4100 is $56 \pm 1\%$

(4) To avoid losses in surface area, the concentrates should be used below 1100°C.

The major emphasis of the remaining discussion will be on bastnaesite concentrate 4100 because fewer impurities are present, permitting analogies with the pure oxides or oxyfluorides.

6.1.2 Reduction

In the previous section, it was shown that adequately calcined bastnaesite concentrates consist of a solid solution of oxyfluorides and oxides with a fluorite type structure. Since $83 \pm 1\%$ by weight of the total rare earth content consists of cerium and lanthanum (see Table A4.3), the remaining discussion can be simplified by considering the calcined concentrates to be made up of a solid solution of LaOF and CeO_2.

It is known that, in a reducing environment, cerium dioxide forms a range of non-stoichiometric oxides with related fluorite type structures containing oxygen vacancies (see section 3.1.1). Thus, it is possible that CeO_2 dissolved in an REOF framework can be similarly reduced. A TGA/DTA reduction study, in carbon monoxide, was undertaken to test this hypothesis. Hydrogen was not used owing to the possibility of hydrolysing oxyfluorides to oxides (refer to section 6.1.3). Solid samples were previously dried at 130°C overnight.

Figure 6.3 illustrates the DTA/DTG[2] of bastnaesite 4100 (as received) in CO. The endothermic peak at 400-600°C, with corresponding weight loss of $1.60 \pm 0.06\%$ (refer to Appendix 7 for calculations), was attributed to the decomposition of residual rare earth fluorocarbonates.

---

(2) A DTG gives the rate of weight change with increasing temperature and is the first derivative of the TGA curve.

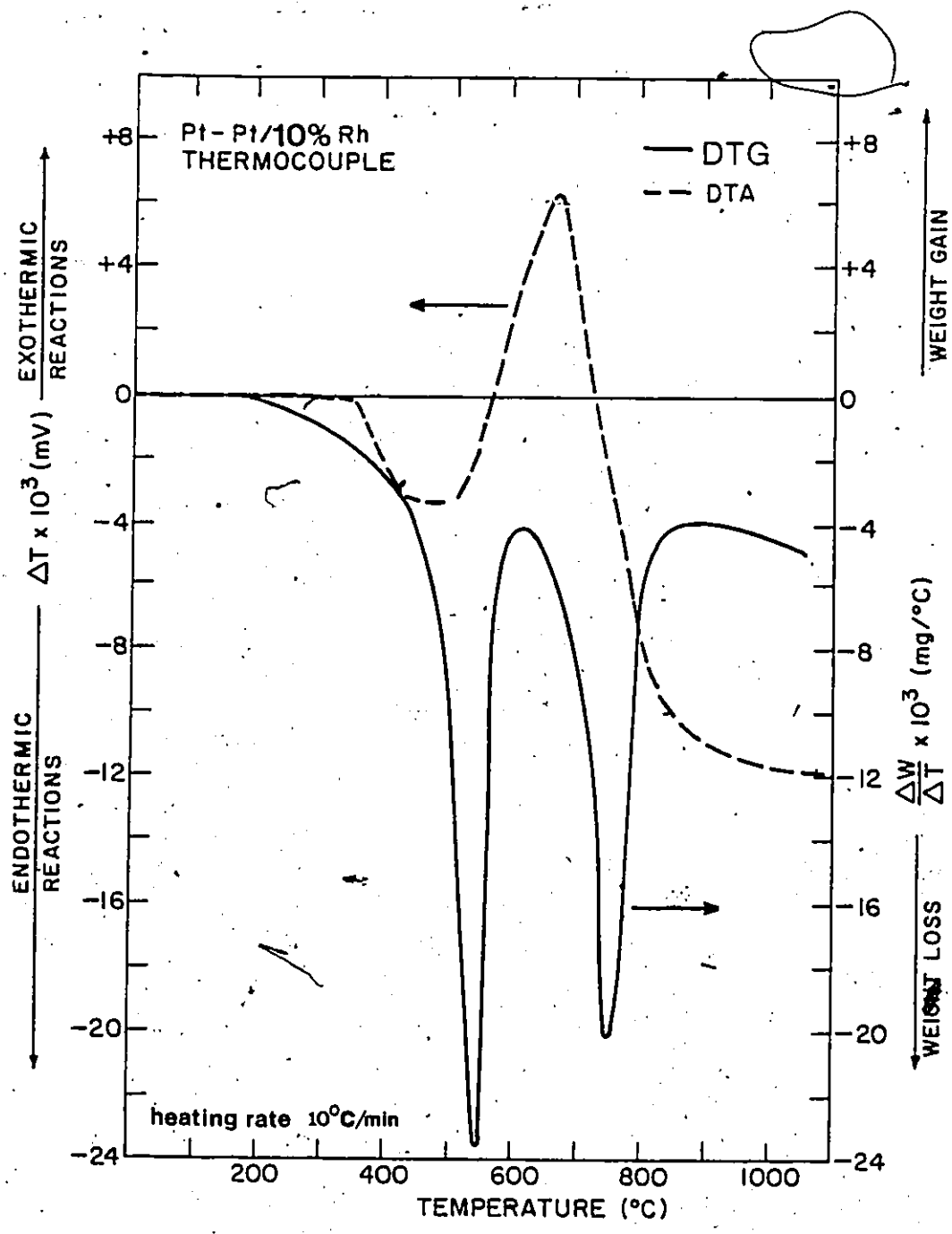

Figure 6.3: DTA and DTG of Bastnaesite 4100 in Carbon Monoxide Using a Netzsch Gerätebau Thermal Analyser.

as discussed in section 6.1.1. The exothermic peak at 600-850°C, with corresponding weight loss of $2.35 \pm 0.06\%$, was concluded to be the result of some type of reduction reaction. Two observations were made:

(1) The theoretically calculated weight loss of $2.19 \pm 0.05\%$, associated with the complete conversion of dissolved CeO_2 in bastnaesite to 'Ce_2O_3', is significantly less than the experimentally measured weight loss of $2.35 \pm 0.06\%$ (see Appendix 7).

(2) Theoretically, partial and full reduction of CeO_2 by CO, are weakly endothermic (5.4 ± 6.3 or 37.7 ± 6.3 kJ·(mol CeO_2)$^{-1}$ respectively); whereas, an exothermic peak was obtained experimentally.

To resolve these contradictions, additional experiments were carried out on LaOF, CeO_2 and bastnaesite 4100, previously calcined at 1000°C, to ensure removal of residual carbonates. Accurate weight loss measurements were obtained by TGA, using large samples (~ 300 mg) on a Netzsch Gerätebau Thermal Analyser Model No. STA 409 (refer to Figure 6.4). DTA curves[3], using small samples (~ 50 mg), were generated on a Dupont 900 Differential Thermal Anayser. Thus, exact resemblance of the DTA curves, illustrated in Figures 6.3 and 6.5, should not be expected. Carbon monoxide or a gas mixture containing 92% CO/8% CO_2 was passed over the samples in these experiments. The latter gas mixture was also used in subsequent desulfurization studies (section 6.2.1).

Figure 6.4 shows that LaOF does not undergo any weight changes, indicating that this compound is unreactive with CO. The endothermic peak at 505°C (refer to Figure 6.5), corresponds to the rhombohedral to fluorite transition temperature reported in the literature (88,89), and also provides an internal check of the temperature ranges reported in this work.

---

(3) Owing to the larger sample sizes used in the TGA studies, temperature ranges for these curves will be delayed with respect to the DTA curves. Thus, only the DTA temperature ranges are reported.

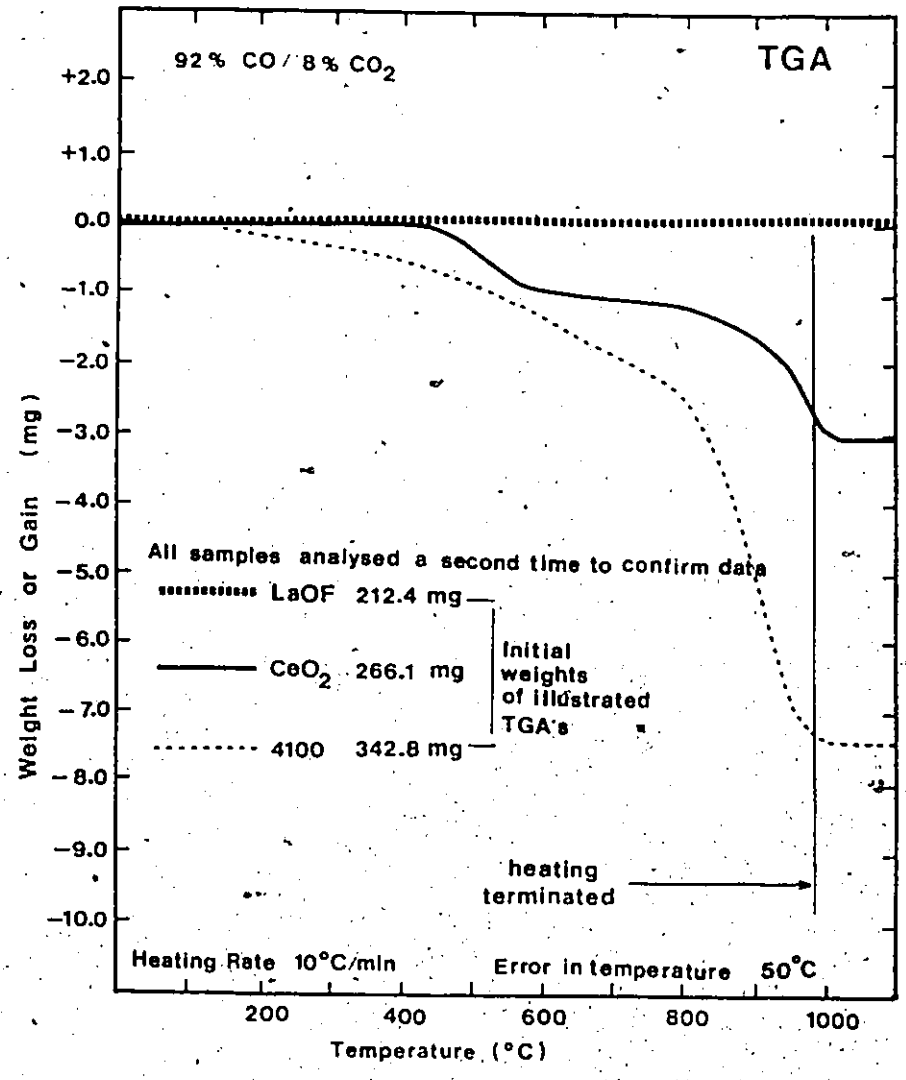

Figure 6.4: TGA curves of calcined LaOF, CeO_2 and Bastnaesite 4100 in 92% CO/8% CO_2, Using a Netzsch Gerätebau Thermal Analyser.

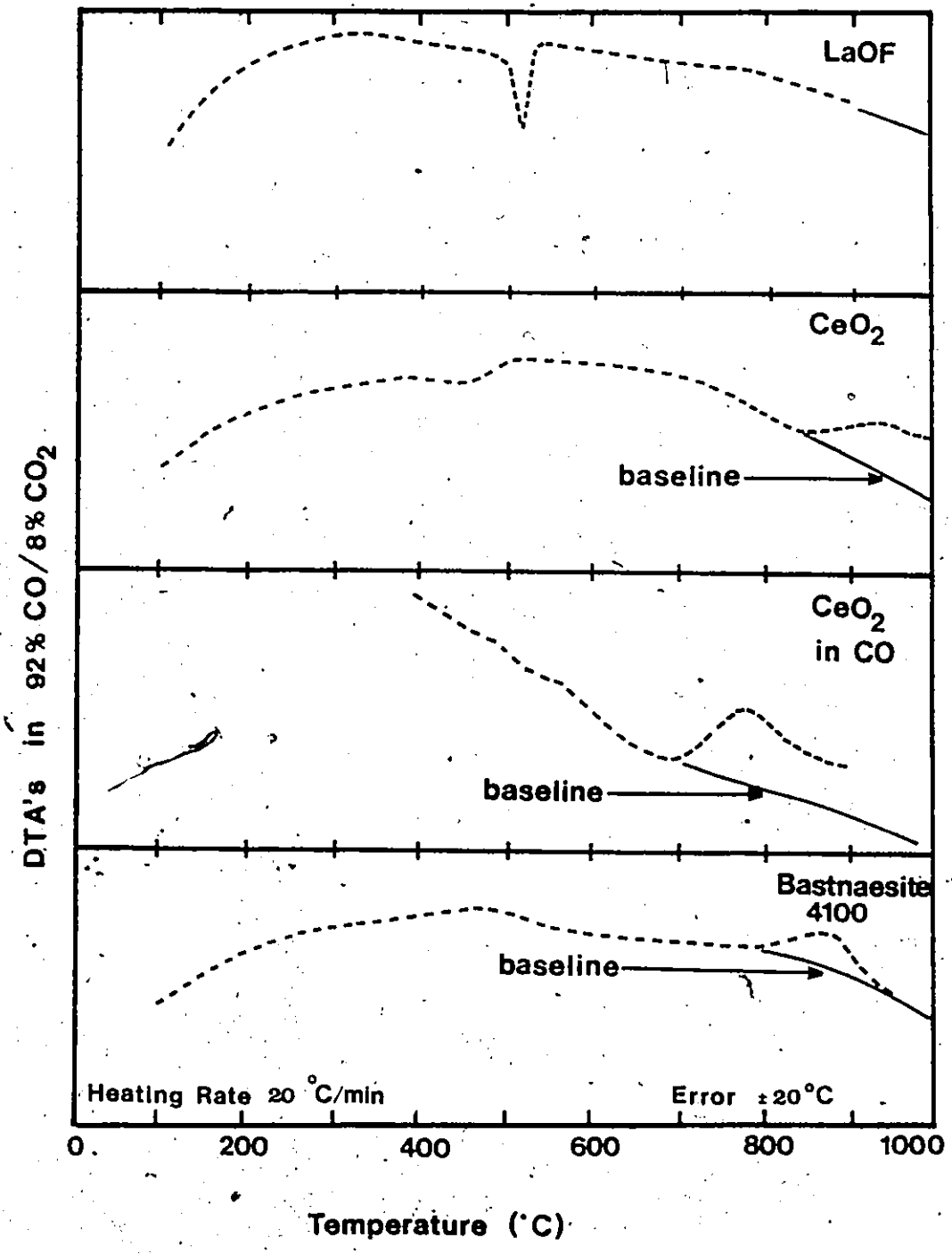

Figure 6.5: DTA curves of calcined LaOF, CeO_2 and Bastnaesite 4100 in 92% CO/8% CO_2 or 100% CO, Using a Dupont Thermal Analyser.

CeO_2 reacts endothermically from 400-500°C and exothermically from 850-1000°C. Although, it is difficult to establish the baseline in the DTA curves, the interpretation of the curves is facilitated by overlaying the DTA and TGA curves such that the DTA peaks correspond to the maximum change of weight in the TGA curves. Under these conditions, it is obvious that the second reduction peak is exothermic rather than endothermic. In pure CO, the exothermic peak is more pronounced. In 92% CO/8% CO_2, the total weight loss (up to 995°C) of 1.09%, corresponds to the molecular formula $CeO_{1.88}$, which is in excellent agreement with the composition predicted by Bevan and Kordis' diagram (41) given in Figure A1.1 of Appendix 1.

Bastnaesite 4100, calcined at 1000°C, shows a negligible peak at 400-600°C (compare Figures 6.3-6.5), but the exothermic peak at 800-900°C still remains. The corresponding weight loss of 2.16 ± 0.06% agrees much better with the predicted value of 2.19 ± 0.05%. In addition, it has been shown that residual carbonates are not responsible for this peak. Since exothermic peaks were obtained for both CeO_2 and bastnaesite 4100, it was concluded that inaccuracies in the thermodynamic data are probably responsible for the differences from theoretical behaviour.

The following conclusions were made from the reduction study:

(1) LaOF (or REOF) in the bastnaesite concentrates is stable in reducing environments (provided H_2O is not present in significant amounts, see section 6.1.3).

(2) Dissolved CeO_2 in bastnaesite concentrates can be completely reduced to the "Ce_2O_3" form. Since the bastnaesite concentrates consist of REOF and CeO_2 in a fluorite type structure, oxygen vacancies in the reduced solids probably exist.

(3) The reduction process is mildly exothermic in carbon monoxide rather than endothermic.

6.1.3 Pyrohydrolysis

During reduction and desulfurization, steam is produced as a by-product of reaction:

$$CeO_2(s) + x\,H_2(g) = CeO_{2-x}(s) + x\,H_2O(g) \qquad 3.3.2$$

$$CeO_{2-x}(s) + H_2S(g) + (1-2x)H_2(g) = Ce_2O_2S(s) + 2(1-x)H_2O(g) \qquad 3.3.5$$

$$CeO_2(s) + H_2S(g) + (1-2x)CO(g) = Ce_2O_2S(s) + H_2O(g) + (1-2x)CO_2(g) \qquad 3.3.6$$

It is possible for the rare earth oxyfluorides in the calcined bastnaesite concentrates to react with the steam, generating hydrofluoric acid:

$$2REOF(s) + H_2O(g) = RE_2O_3(s) + 2HF(g) \qquad 6.1.3$$

Since corrosion, associated with the evolution of hydrofluoric acid, may prohibit the use of bastnaesite concentrates for desulfurization purposes, thermodynamic and kinetic evaluations are necessary to determine the conditions when reaction 6.1.3 becomes significant.

6.1.3.1 Pyrohydrolytic Thermodynamic Evaluation

Standard free energies of formation of rare earth fluorides and oxyfluorides (RE = La, Pr, Sm, Ce) were determined in 1982 by Hong, using solid electrolyte cells, and selected thermodynamic values are given in Table 6.5 (15). Pertinent equilibrium data for the hydrolysis reactions were calculated (see Appendix 8) and are summarized in Table 6.6.

The equilibrium constants indicate that LaOF is reasonably stable, even in pure steam at elevated temperatures; whereas, CeOF readily decomposes in air in the presence of small quantities of moisture. However, the stability of CeOF is strongly dependent on oxygen partial pressure, and in a typical coal gas ($p_{O_2} = 10^{-20}$, $p_{H_2O} = 0.015$), CeOF could exist since the equilibrium partial pressure of HF is small (1.9×10^{-5} atm).

Table 6.5: Selected Thermodynamic Values of Rare Earth Fluorides and Oxyfluorides (15).

Compound	$\Delta H°$ kJ·mol^{-1}	$-\Delta S°$ kJ·mol^{-1}·K^{-1}	Error in $\Delta G°$ kJ·mol^{-1}	Valid Temperature Range (K)
LaOF	-1222.73	0.1831	6.63	950-1120
LaF_3	-1765.46	0.2296	11.36	950-1120
CeOF	-1179.29	0.1480	9.03	1077-1277

Table 6.6: Equilibrium Data for Pyrohydrolysis Reactions*

Reaction	$2LaOF(s) + H_2O(g) = La_2O_3 + 2HF(g)$	$2CeOF(s) + H_2O(g) + \frac{1}{2}O_2(g) = 2CeO_2(s) + 2HF(g)$
$\Delta G°$(kJ·mol^{-1})	380569 – 156.2T	-118785 + 61.99T
Valid Temperature Range (K)	< 1134	> 1077
K_{1100}	1.23×10^{-10}	2.52×10^{2}
P_{HF} (atm.) at 1145 K	1.11×10^{-5} ($p_{H_2O} = 1$) 2.22×10^{-6} ($p_{H_2O} = 0.04$)	2.31 ($p_{O_2} = 0.21$, $p_{H_2O} = 0.02$) 1.9×10^{-5} ($p_{O_2} = 10^{-20}$, $p_{H_2O} = 0.015$)

* Refer to Appendix 8 for calculations

The phase stability diagrams, illustrated in Figures 6.6 and 6.7, clearly show that CeOF is unstable above oxygen partial pressures of about 10^{-12} atm. at 1100K; whereas, LaOF has a stability region which extends over the entire range of oxygen partial pressures. Although thermodynamic data have not been previously measured for these oxyfluorides, the general observations of other investigators are consistent with these predictions. Finkelburg and Stein (91) noted that heat treatment of LaOF at 1200°C in oxygen has no effect, while temperatures above 300°C are sufficient for the quantitative transformation of CeOF to CeO_2. Pannetier and Lucas (92) mentioned that CeOF is unstable in air at room temperature and decomposes to $CeO_{1.15}F_{0.85}$ over a period of 10 days.

The thermodynamic data presented in this section provide additional quantitative arguments for the existence of a solid solution of CeO_2 and REOF in calcined bastnaesite concentrates. During the calcination process, the temperature (>550°C), oxygen and steam partial pressures (p_{O_2} = 0.21, p_{H_2O} = 0.02) would favour the rapid decomposition of CeOF (if formed) to CeO_2.

6.1.3.2 Pyrohydrolytic Kinetic Evaluation

The equilibrium constants indicate that very low HF partial pressures are generated when LaOF is exposed to steam at elevated temperatures. The reactivity, of course, will be dependent upon the chemical rate constant.

To study the rate of hydrofluoric acid evolution as a function of time, powdered bastnaesite concentrates, 4100 and 4000C (particle size 1-65 µm), were placed in an alundum boat in the center of a quartz tube heated by a resistance furnance (see Figure A9.1 in Appendix 9). Steam was passed over the solid, condensed and titrated with standard thorium nitrate (94) at regular time intervals. With the exception of the choice of titrant, the technique is similar to one used by Powel and Menis (93). Thorium nitrate was chosen because both

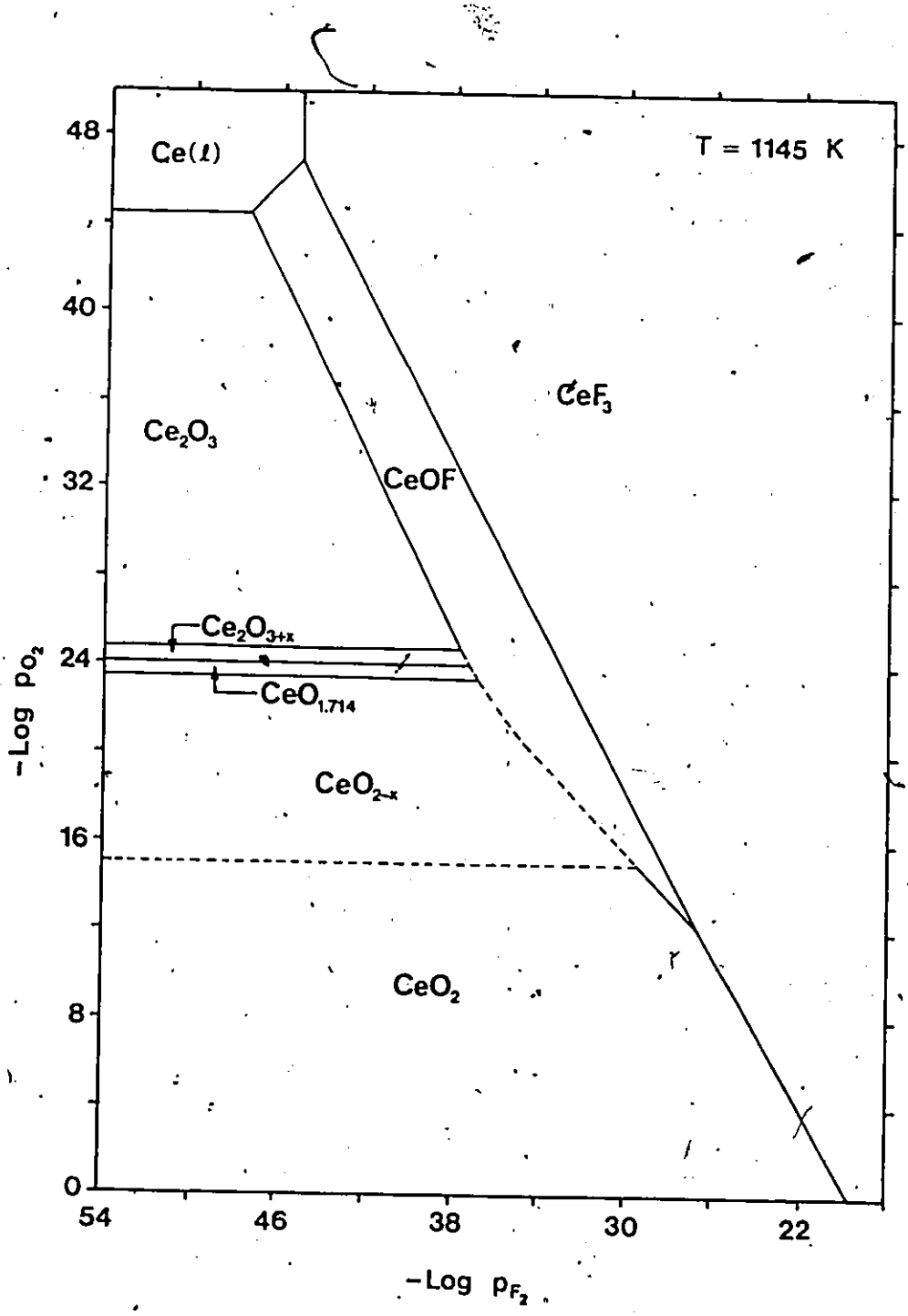

Figure 6.6: The Ce-O-F Phase Stability Diagram at 1145K (15).

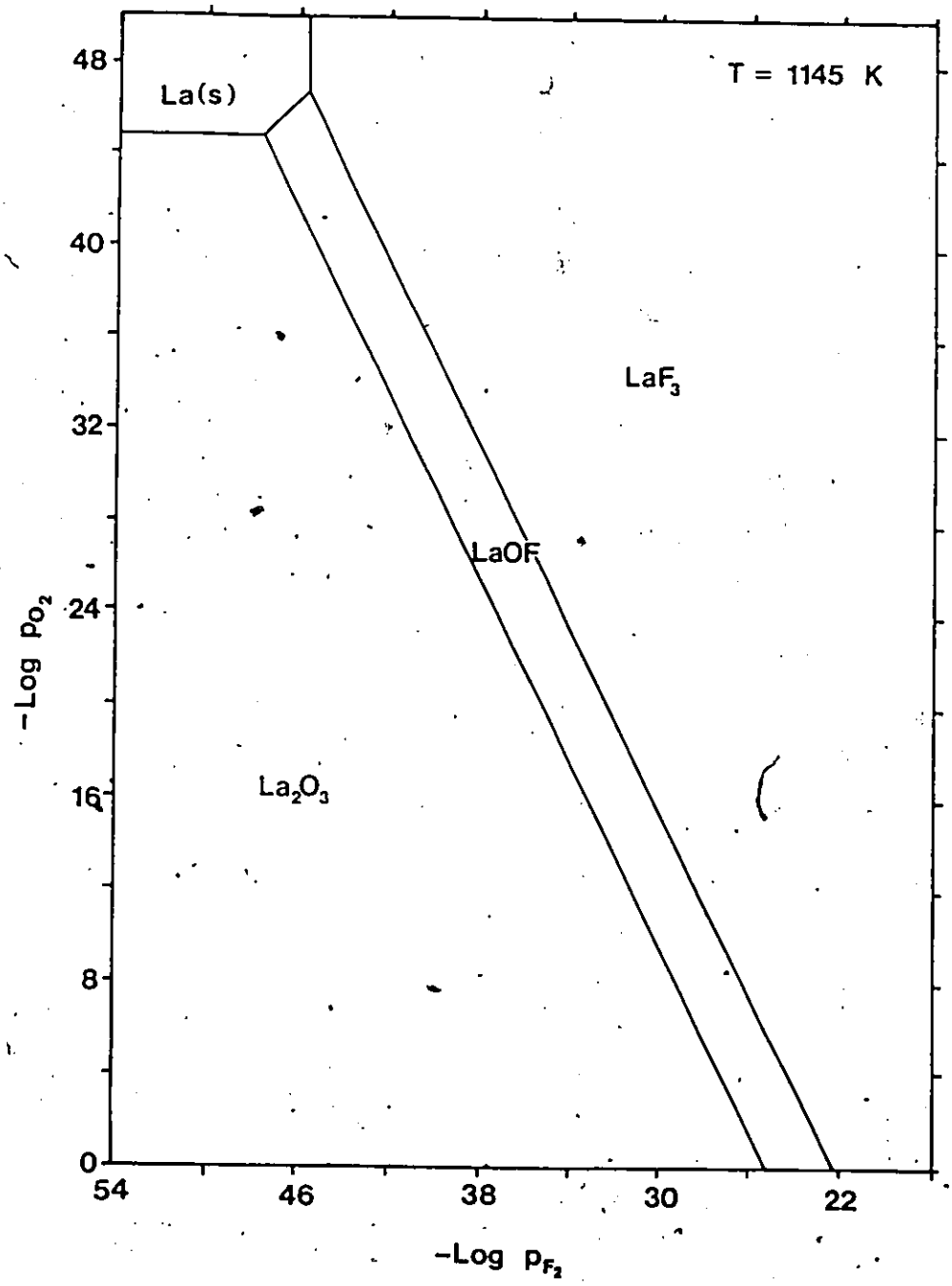

Figure 6.7: The La-O-F Phase Stability Diagram at 1145K (15).

hydrofluoric and silicic acids can be analysed by this method (the latter forms when HF reacts with the silica walls of the reactor). To obtain hydrolysis curves within a reasonable time frame, experiments were carried out above 700°C. High steam flow rates were used (36.8 L/min) to eliminate the effects of gas film diffusion.

Figure 6.8 illustrates the pyrohydrolysis curves obtained by Giacomelli (14). The results are included in this thesis because the experimental proposal (95), preliminary work and the final kinetic analysis were done by the author. The leached concentrate, 4100, hydrolyses faster than the 4000C concentrate containing calcite. Thus, it appears that the calcium carbonate inhibits the reactivity of the oxyfluorides in the bastnaesite concentrates with steam.

The pyrohydrolysis curve of concentrate 4100 is noted to level off at a slightly higher fluorine content than anticipated from the chemical analysis given in Table A4.3 of Appendix 4 (7.0 wt% F vs. 5.0 wt% ± 0.25. The differences in agreement were attributed to the difficulty in estimating the gradual pink endpoint during titration when the change in fluorine content is small. The limiting value, however, is not expected to affect the initial rates of reaction.

To obtain the activation energy for the pyrohydrolysis of bastnaesite 4100, the initial rates or reaction were estimated from the limiting slopes ($t \rightarrow 0$) of the hydrolysis curves, illustrated in Figure 6.8, and used to calculate the first order rate constant, k (see Appendix 9). An activation energy of E_a = 121 ± 15 kJ/mol is obtained from the plot of $\ln k$ versus 1/T, presented in Figure 6.9. This value is characteristic of reactions proceeding under

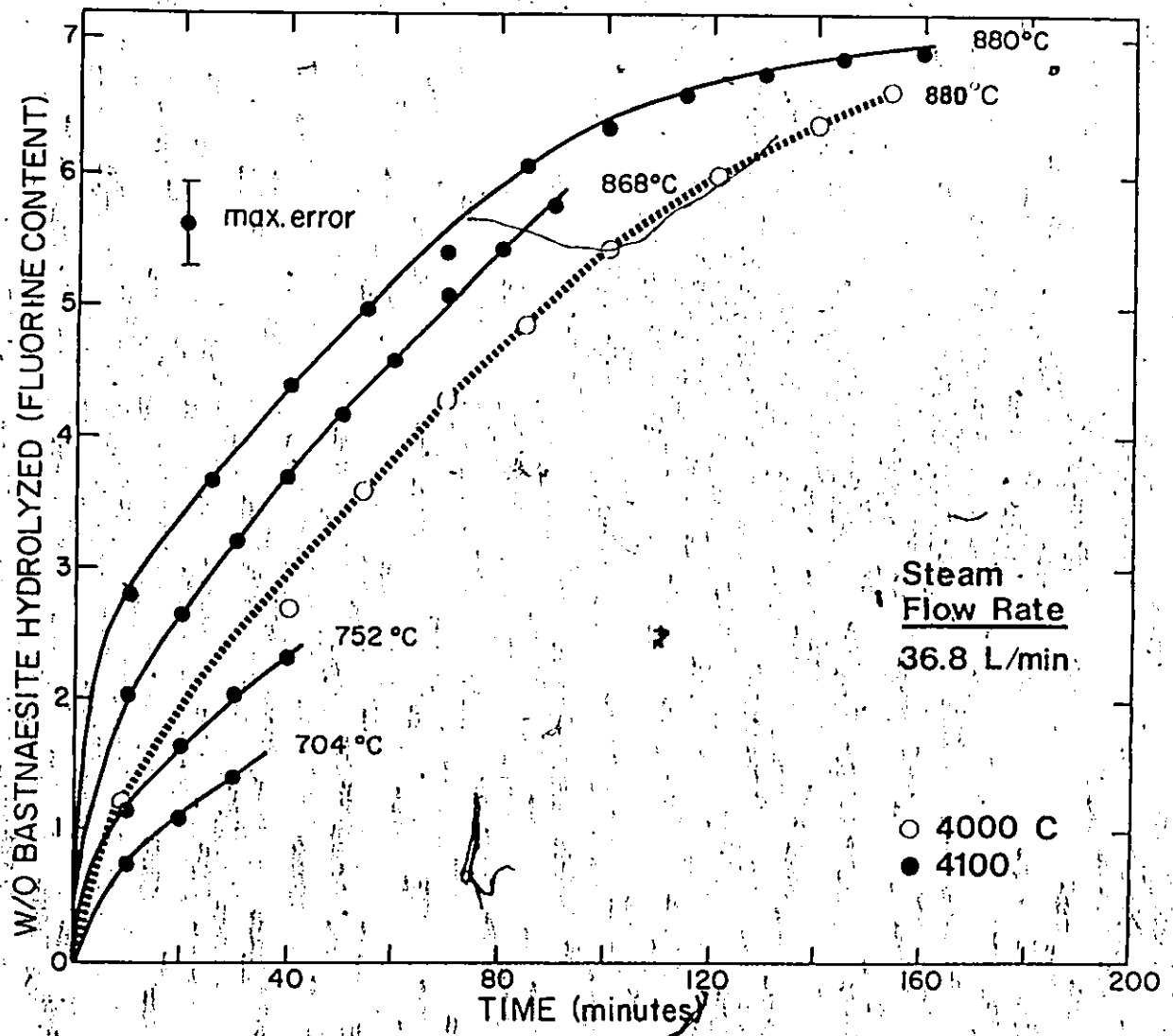

Figure 6.8: Pyrohydrolysis Curves for Bastnaesite Concentrates 4000C and 4100 (14).

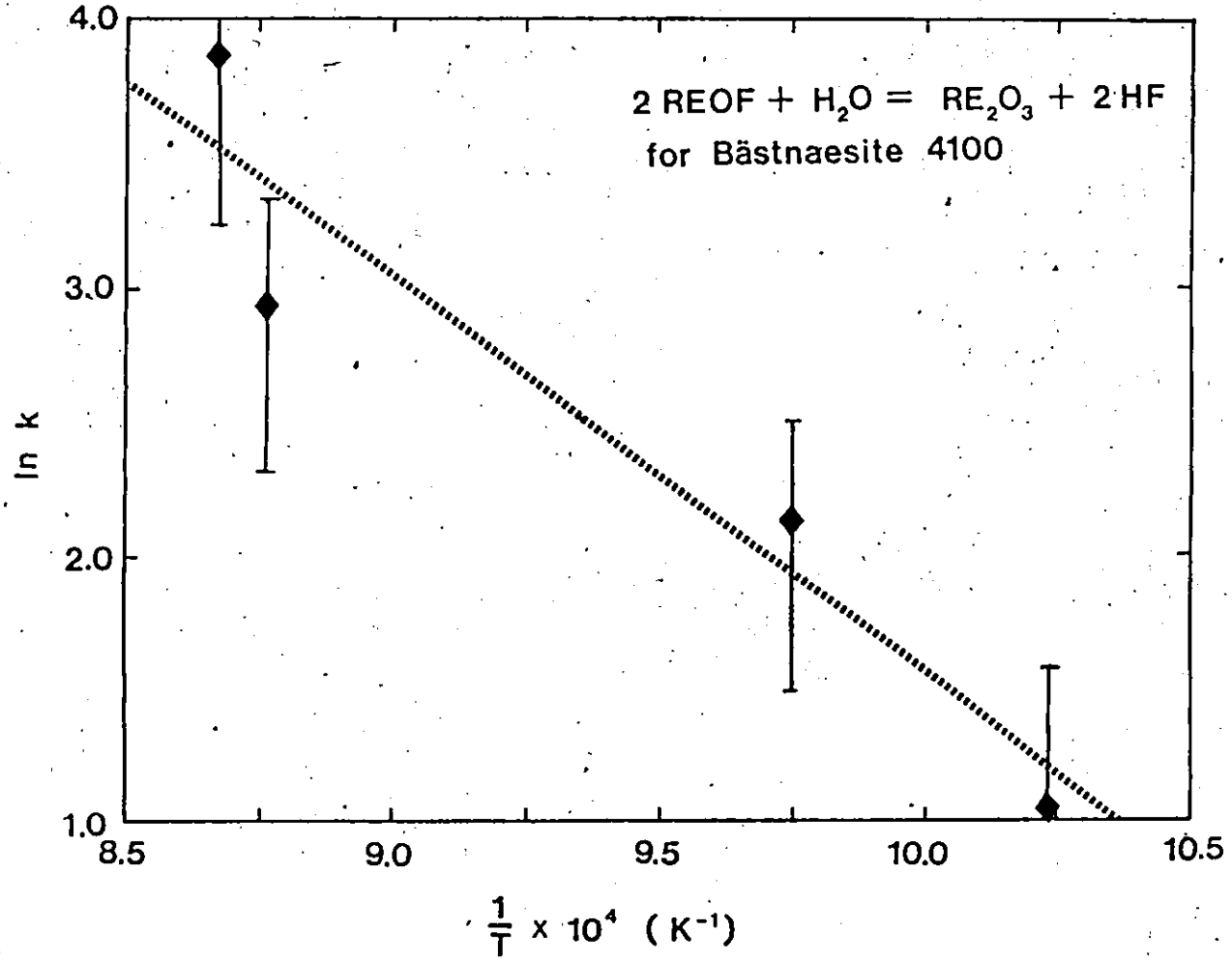

Figure 6.9: Plot of $\ell n\ k$ versus 1/T for the Pyrohydrolysis Reaction Using Bastnaesite Concentrate 4100.

kinetic control (i.e. $E_a > 33.5$ kJ·mol^{-1}, see section 2.2.1). The sensitivity of the rates of reaction to temperature indicated that, in steam, HF corrosion may be significant above 750°C.

The following conclusions were made from the pyrohydrolsis study:

(1) The equilibrium constants for the pyrohydrolysis reaction with LaOF and CeOF are 1.23×10^{-10} and 2.52×10^{2}, respectively, at 1100K. LaOF is relatively stable in steam; whereas, CeOF decomposes in the presence of small quantities of moisture in air. During calcination, CeOF would not form in bastnaesite since the conditions favour the formation of CeO_2. Thus, bastnaesite concentrates should consist primarily of a solid solution of LaOF and CeO_2.

(2) The activation energy for the pyrohydrolysis reaction was estimated for bastnaesite concentrate 4100. Small particles (1-65 μm) and high steam flow rates (36.8 L/min) were used to eliminate diffusional and mass transfer limitations. The value of E_a = 121. ± 15 kJ/mol was within the kinetic control regime. However, under reduction and desulfurization conditions, with considerably lower concentrations of steam, decomposition of the rare earth oxyfluorides in the bastnaesite concentrates would be slow. Corrosion associated with the evolution of HF would be unimportant.

6.1.4 Desulfurization/Regeneration

Preliminary work by Kay et al. (10,11) confirmed the viability of using bastnaesite concentrates for the desulfurization of coal gases. Regeneration can be accomplished in air, permitting recycling of the sorbent and lowering the capital cost of the process.

The main purpose of this study is to shed light upon the desulfurization/ regeneration processes. In previous sections, it was shown that calcined bastnaesite concentrates consist primarily of a solid solution of CeO_2 and LaOF; thus, two desulfurization mechanisms can contribute to the overall behaviour:

(1) The reaction of reduced CeO_2, dissolved in the concentrate, with H_2S:

$$2\,CeO_{2-x}(s) + H_2S(g) + (1-2x)H_2(g) = Ce_2O_2S(s) + 2(1-x)H_2O \qquad 3.3.5$$

$$2\,CeO_{2-x}(s) + H_2S(g) + (1-2x)CO(g) = Ce_2O_2S(s) + H_2O(g) + (1-2x)CO_2(g) \qquad 3.3.6$$

(2) The reaction of rare earth oxyfluorides (mainly LaOF) with H_2S:

$$REOF(s) + H_2S(g) = RESF(s) + H_2O(g) \qquad 6.1.4$$

Although a few rare earth thiofluorides have been reported (97,98), very little is known about these compounds. Equilibrium constants for reaction 6.1.4 could not be calculated because the free energies of formation of the thiofluorides have not yet been determined. However, thiofluorides must have an important role in the desulfurization process because Kay (10,11) and Baron (6) observed that bastnaesite concentrates, containing their original fluorine, are more active than rare earth oxides or treated forms of bastnaesite (i.e. steamed, leached, etc.).

Since it was not possible to study all aspects of the desulfurization/regeneration behaviour of bastnaesite concentrates, cerium oxide sorbents were investigated for the following reasons:

(1) The behaviour of a pure component is easier to study and relate to theoretical predictions than a complex solid.

(2) Cerium oxide is a major component in calcined bastnaesite concentrates (concentrate 4100 is approximately 32% by weight CeO_2).

(3) Thermodynamic data are available for some of the compounds in the Ce-O-S system.

In Chapter III, the available thermodynamic data were consolidated into the Ce-O-S phase stability diagram, and used to predict the predominant desulfurization/regeneration reactions and their associated equilibrium constants. The following discussion deals with the experimental verification of these predictions and the kinetic behaviour of cerium oxide sorbents.

6.2 Desulfurization/Regeneration Studies Using Cerium Oxides

6.2.1 Desulfurization

A simulated coal gas, containing 1.2% H_2S, 10.8% CO_2, 55% CO and 33.0% H_2, was passed through a fixed bed reactor containing 17.94 g of cerium oxide sorbent (previously sintered at 1400°C, and reduced overnight with 5% H_2/95%N_2, $\varepsilon_p = 0.114$, $d_p = -0.841/+0.297$ mm). A typical desulfurization breakthrough curve, at 1145 K, is illustrated in Figure 6.10 (see Appendix 10 for g.c. traces).

6.2.1.1 General Discussion of Breakthrough Curves

Difficulties were encountered when using the flame photometric detector (FPD) in obtaining the complete breakthrough curve. Despite the manufacturer's claim that the FPD has a dynamic range for sulfur of 1 ng to 600 ng, absolute, in the volume injected (99), experimental work showed that only a 100 ng S limit could be achieved (equivalent to 1600 ng S/mL or 1225 ppm by volume for a 1/16 mL sample loop, the smallest gas sampling loop which can be practically used). Excellent, reproducible data could be obtained prior to, and during breakthrough. At the tail end of the breakthrough curve, gas chromatograph traces contained multiple peaks, which is characteristic of H_2S concentrations well above the detector limit. This observation was most apparent during the calibration of the gas

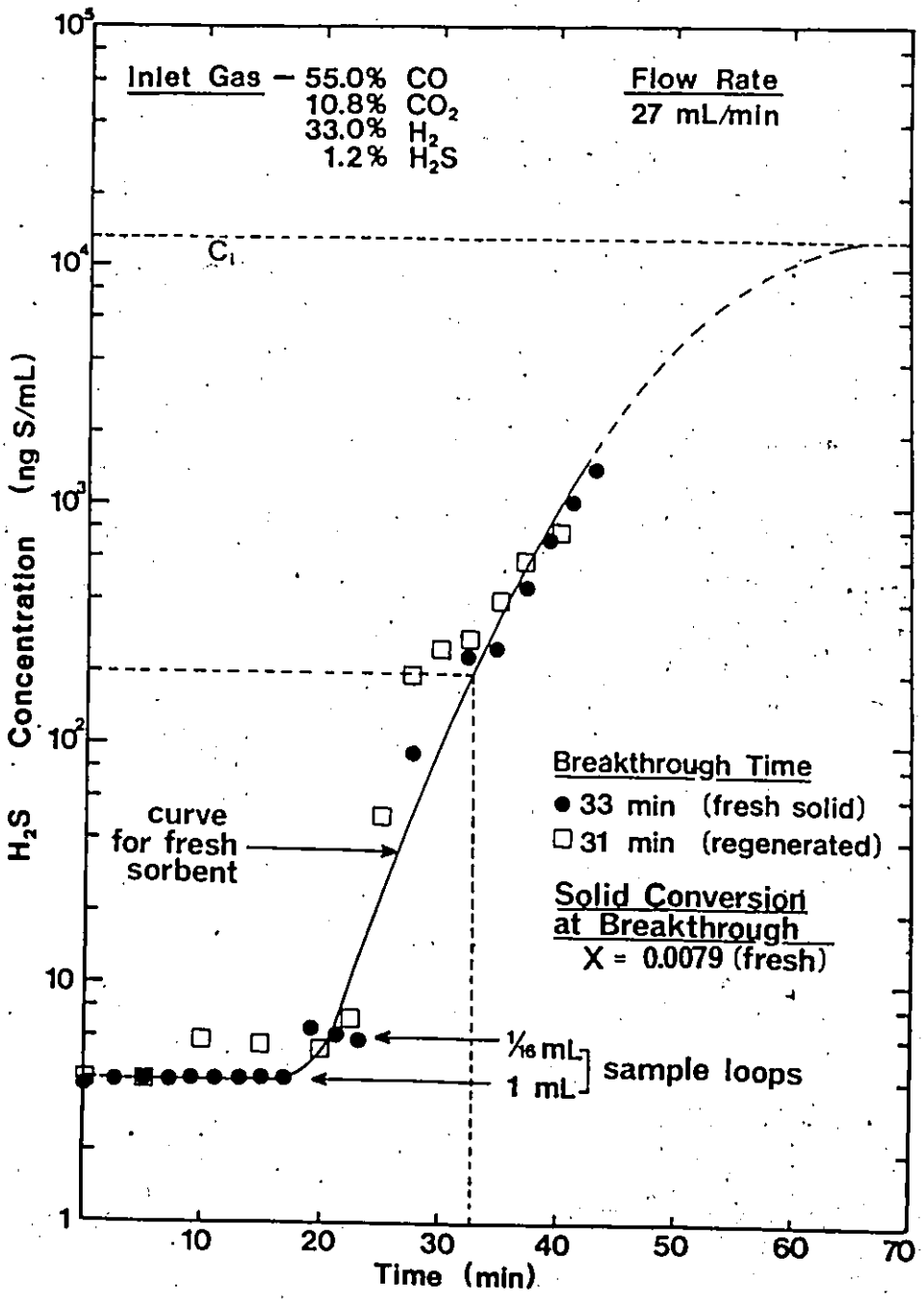

Figure 6.10: A Typical Desulfurization Breakthrough Curve at 1145 K.

chromatograph (g.c.), using the exponential dilution flask (EDF), described in section 5.3 and Appendix 3. Even though calibration samples contained one detectable component, the first few g.c. injections resulted in multiple peaks, if the concentration of H_2S was too high. As the EDF effluent decreased in concentration, single peaks were obtained. However, at the 100 ng sulfur limit, detector saturation is difficult to detect since the g.c. response gives single peaks, with nearly identical responses over a fairly large range of concentrations (see calibration curve, Figure 5.4).

6.2.1.2 Verification of Thermodynamic Predictions

In section 3.2, it is shown that the predicted partial pressure of H_2S, corresponding to point C (see Figure 3.3), is 50.2×10^{-6} atm, at 1145 K. A value of $(3.1 \pm 1) \times 10^{-6}$ atm (4.0 ng S/mL), averaged over three runs, was determined experimentally. The oxygen and sulfur potentials of the exit gas are plotted in Figure 6.11, and it can be seen that better estimates of the exit H_2S concentrations are obtained if the CeO_{2-x}/Ce_2O_2S boundary is extended from the Ce_2O_3/Ce_2O_2S boundary. Data points, measured at three other temperatures (refer to Table 6.7), gave similar results (see Figures 6.12, 6.13 and 6.14). Further work, using a wide range of coal gas compositions, is recommended in order to locate additional points on the CeO_{2-x}/Ce_2O_2S boundary.

The experimental point illustrated in Figure 6.15, confirms the position of the CeO_2/Ce_2O_2S boundary, and was determined from the solid electrolyte cell measurements reported by Dwivedi (16), at 1072 K.

6.2.1.3 The Effect of Reduction

Prior to all desulfurization experiments, the cerium oxide sorbent was reduced with 5% H_2/95% N_2. When the solids were reduced for 2 to 3 hours, immediate breakthrough of

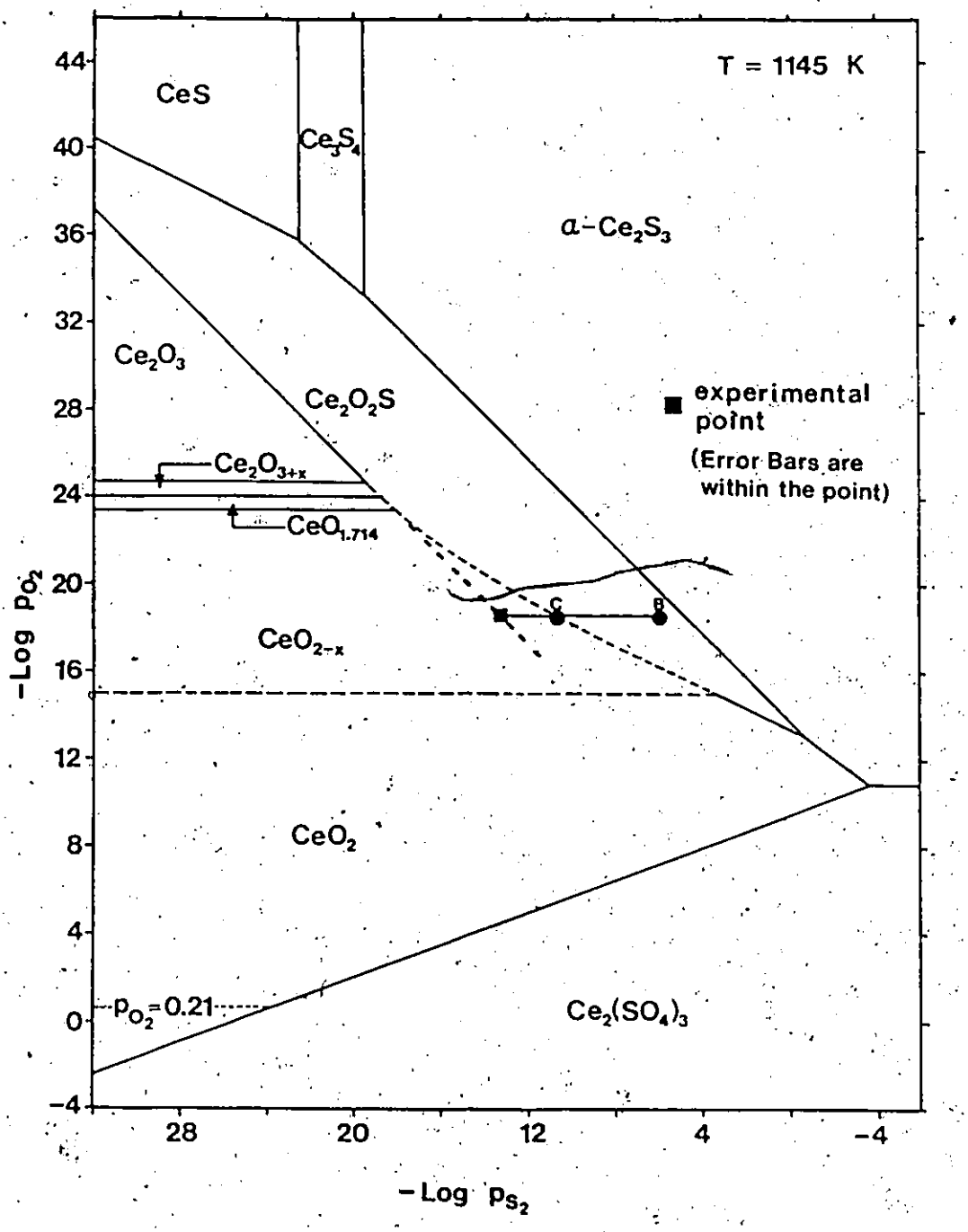

Figure 6.11: The Ce-O-S Phase Stability Diagram at 1145 K, indicating Position of an Experimental point on the CeO_{2-x}/Ce_2O_2S Boundary.

Table 6.7: Equilibrium H_2S Partial Pressure Measurements

		Experimental Values		Theoretical Values*	
T (K)	CeO_{2-x} Phase	p_{H_2S}	$-\log p_{s_2}$	p_{H_2S}	$-\log p_{s_2}$
1145	$CeO_{1.935}$	3.0×10^{-6}	13.1	2.0×10^{-6}	13.4
1189	$CeO_{1.911}$	6.0×10^{-6}	12.1	3.5×10^{-6}	12.6
1244	$CeO_{1.877}$	3.7×10^{-6}	12.1	5.2×10^{-6}	11.9
1296	$CeO_{1.862}$	4.3×10^{-6}	11.7	9.0×10^{-6}	11.1

* Theoretical values obtained by extending Ce_2O_3/Ce_2O_2S boundary.

Partial pressures are given in atmospheres. The standard deviations are $\pm 1 \times 10^{-6}$ atm.

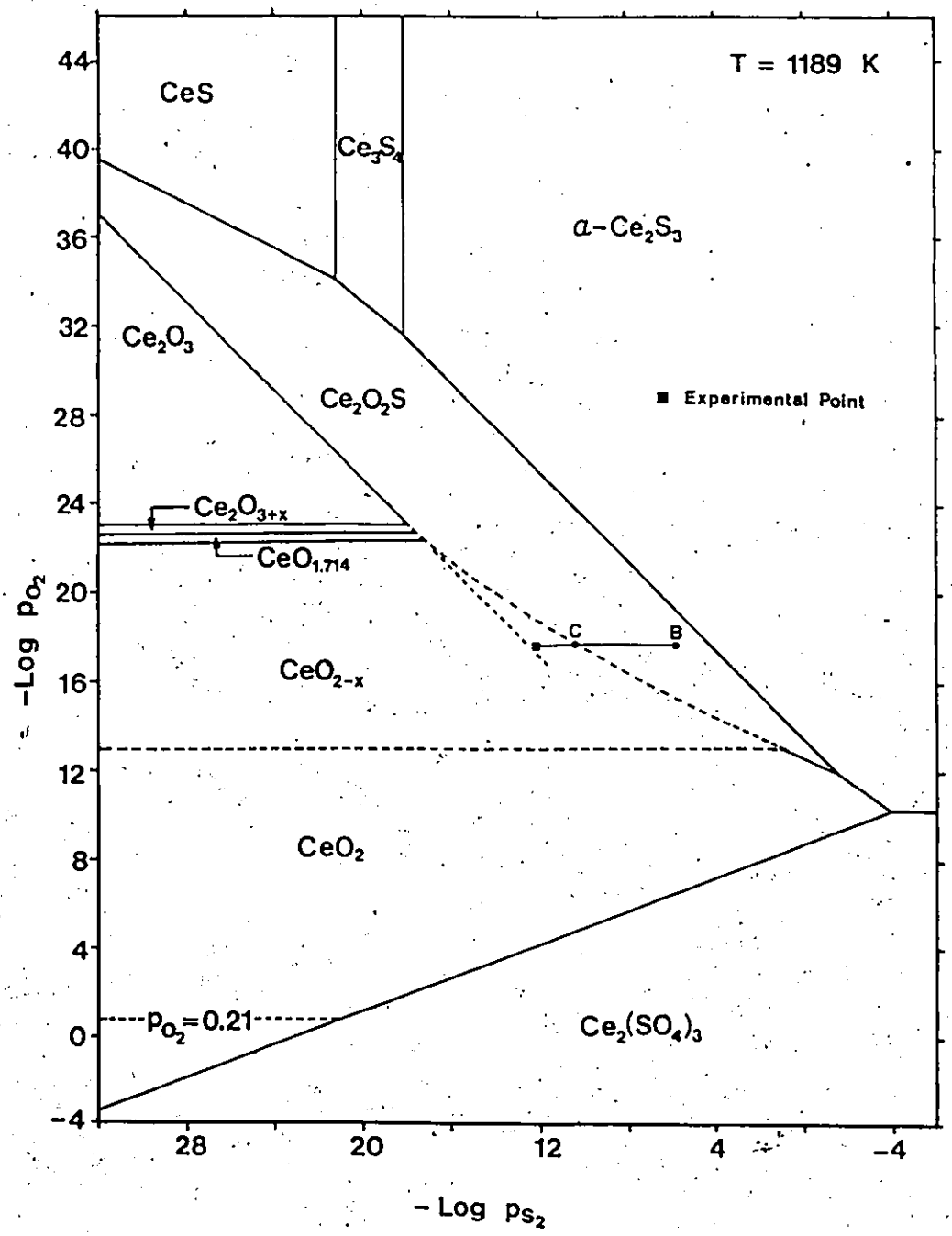

Figure 6.12: The Ce-O-S Phase Stability Diagram at 1189 K.

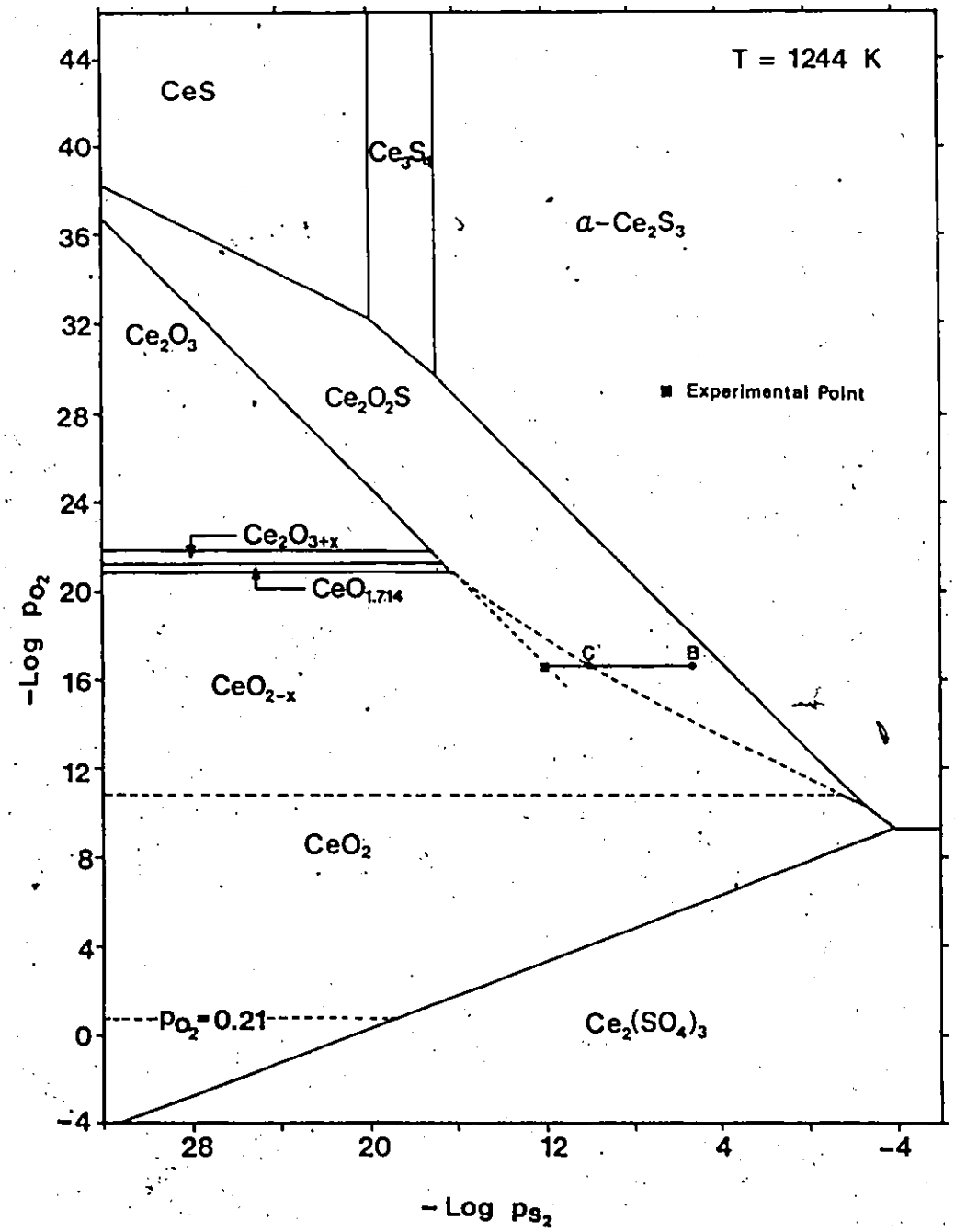

Figure 6.13: The Ce-O-S Phase Stability Diagram at 1244 K.

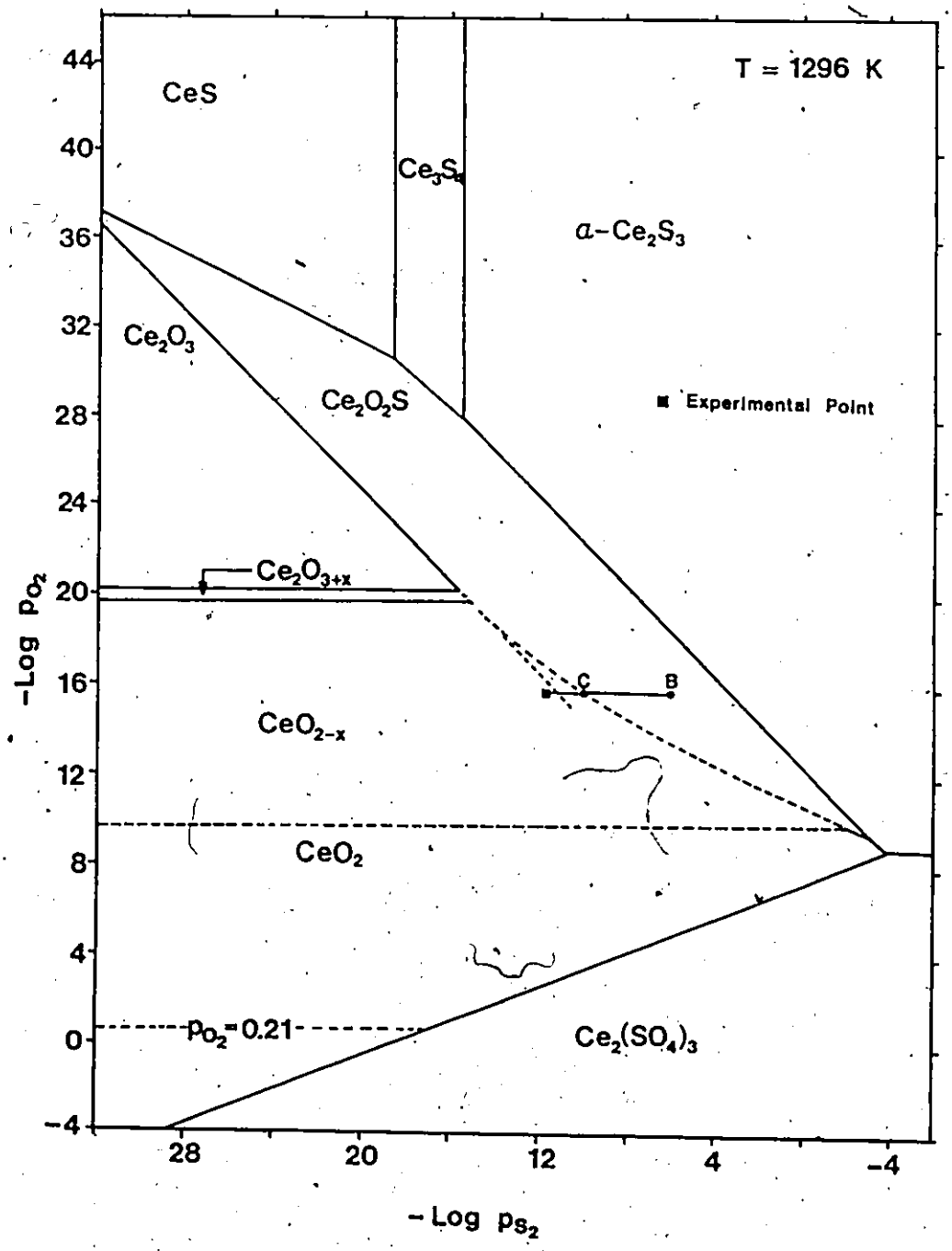

Figure 6.14: The Ce-O-S Phase Stability Diagram at 1296 K.

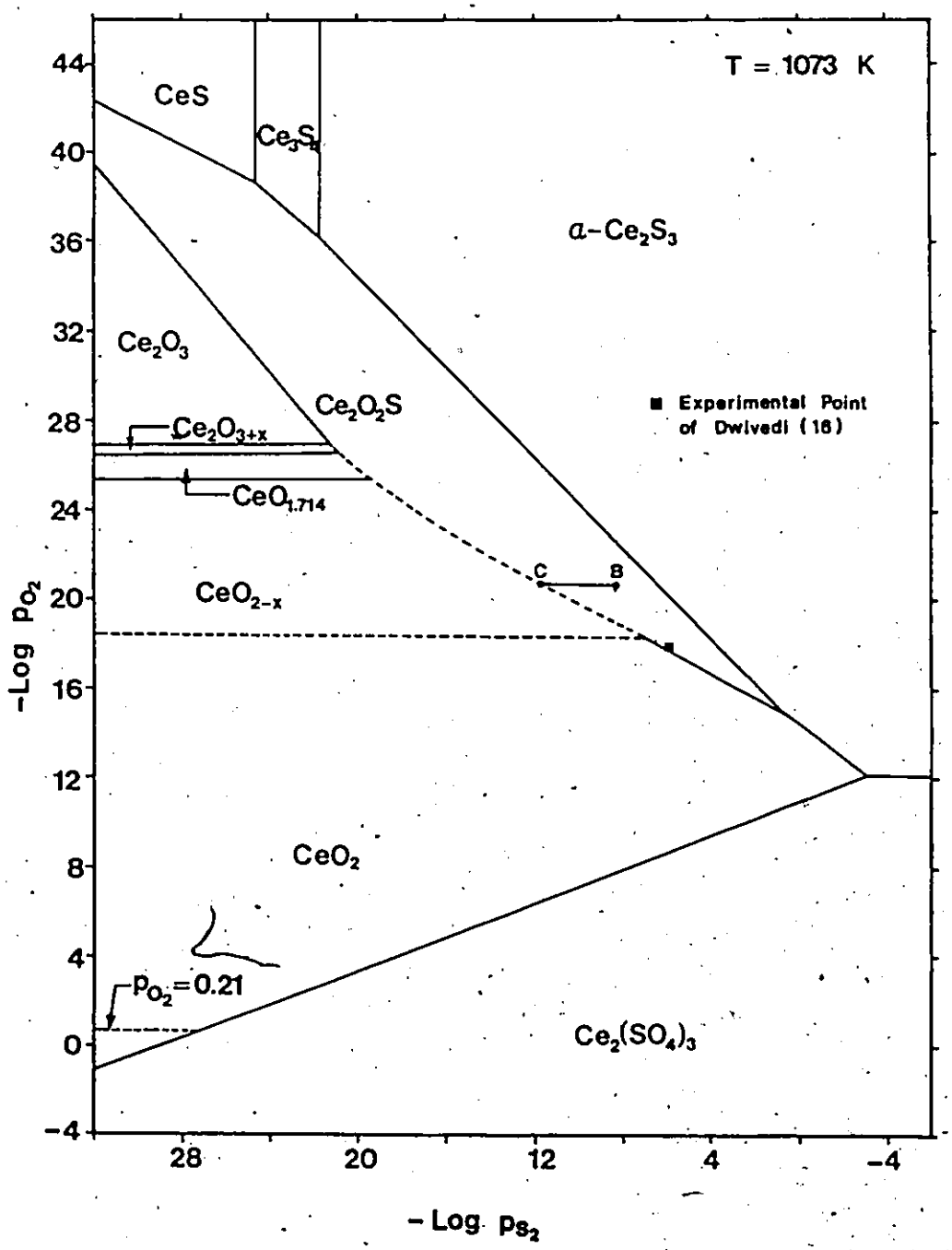

Figure 6.15: The Ce-O-S Phase Stability Diagram at 1073 K.

H_2S occurred in the subsequent desulfurization run; whereas, sorbents reduced overnight desulfurized effectively for 30-40 minutes under the same conditions. In section 3.1.1, it was shown that CeO_{2-x} has a fluorite type framework containing oxygen vacancies. Thus, the reduction step must enhance the reactivity of the cerium oxide sorbent by providing empty sites for the adsorption of sulfur. Since reduction in hydrogen is not very favourable ($K_{1100} = 1.03 \times 10^{-5}$, refer to section 3.3.1), two or three hours is probably not sufficient to convert the CeO_2 to CeO_{2-x}. This was verified by examination of the reduced sorbents; solids reduced for two hours were mainly white, with a small pale blue section at the fixed bed inlet, whereas, solids reduced overnight were deep blue. Westmoreland and Harrison (27) judged cerium oxide to be an unsatisfactory sorbent because it forms a stable unreactive oxide. This study shows that CeO_2, when reduced, is comparatively reactive. Reduction with carbon monoxide should be more favourable ($K_{1100} = 1.04$).

6.2.1.4 Hydrogen Sulfide Removal Efficiency and Adsorption Capacity

The H_2S removal efficiency is based on the gas phase conversion prior to breakthrough and is defined as the fraction or percentage of H_2S removed from the gaseous inlet stream. The exit concentrations, measured in section 6.2.1.2, represent removal efficiencies of 99.98%. It should be noted, however, that a direct comparison of removal efficiencies for different sorbents is valid only for inlet gases having similar oxygen and sulfur partial pressures.

The adsorption capacity, on the other hand, is the fraction or percentage of solid reactant converted at breakthrough[4]. When the solid product has a significantly larger

(4) In this work, the breakthrough point was defined as the time at which C_{H_2S} = 200 ng S/mL or 150 ppm.

molar volume than the solid reactant, the reaction may terminate before 100% conversion is reached, due to pore closure by the solid product, as is the case in this investigation (the density of Ce_2O_2S is 5.99 g/cm^3 compared to 7.2 g/cm^3 for CeO_2). In the absence of pore diffusion control, the maximum theoretical capacity, for a given initial porosity, can be estimated using the changing voidage pore model of Ramachandran and Smith (77). Conversions, smaller than the theoretically predicted values, are obtained when pore diffusion control is predominant because of the sharp gaseous concentration gradients in the pores; reaction rates are consequently increased at the pore mouth, which results in pore closure at earlier times. The porosity of the cerium oxide sorbent was 11.4%; thus, the maximum capacity would be 58% (refer to Appendix 6 for calculations). Experimentally, solid conversions less than 1.0% were obtained, which suggests that pore diffusion is very significant. This conclusion was confirmed by examination of reacted pellets which show a blue inner core of CeO_{2-x} surrounded by a dark green outer layer.

The pore model suggests that a minimum porosity of 18% is required, in the absence of pore diffusion control, to achieve solid conversions of 100% (see Appendix 6). Thus, the next set of experiments utilized a sorbent of 28% porosity.

6.2.1.5 Kinetic Evaluation

In this section, the qualitative effects of temperature, particle size and gas flow rate upon the adsorption capacity and upon the rate of reaction are discussed.

Experiments were carried out with sorbents sintered at 1250°C (ε_p = 0.28, B.E.T. surface area = 0.45 m^2/g, average pore radius = 1.68 x 10^{-5} cm). The simulated coal gas was prepared by blending two gas streams, one containing 91.9% CO/8.1% CO_2, the other 99.0% H_2/1.0% H_2S. The high temperature gaseous composition for a given run (see Table 6.8), was

Table 6.8: High Temperature Inlet Composition of Gas Mixtures.*

Run No.	12	15	16	17	18
Component	Mole Fraction of Component				
CO	0.702	0.702	0.699	0.710	0.701
H_2	0.235	0.235	0.238	0.226	0.236
CO_2	0.0424	0.0424	0.0450	0.0468	0.0452
H_2O	0.0179	0.0179	0.0153	0.0146	0.0153
H_2S	0.00225	0.00225	0.00225	0.00212	0.00224
COS	0.000299	0.000299	0.000300	0.000303	0.000300
S_2	3.76×10^{-8}	3.76×10^{-8}	2.14×10^{-8}	1.91×10^{-8}	2.14×10^{-8}
O_2	7.3×10^{-20}	7.3×10^{-20}	1.74×10^{-21}	1.36×10^{-21}	1.75×10^{-21}

* Calculated by F*A*C*T. Flow rates of the 91.9% CO/8.1% CO_2 and 99.0% H_2/1.0% H_2S gas mixtures were used to estimate the room temperature composition of the coal gas.

calculated by F*A*C*T (refer to Appendix 2), from the respective room temperature gas flow rates multiplied by the appropriate mole fraction of the component. The oxygen partial pressure of the coal gases were plotted on the Ce-O-S phase stability diagram and were shown to be within 0.5 log units of the oxygen potentials of the coal gas used in section 6.2.1.1. The high temperature composition was also used to estimate the molecular diffusivity of H_2S in the gas mixture (Appendix 11).

The experimental conditions and results for five runs are presented in Table 6.9. Figure 6.16 illustrates the corresponding breakthrough curves for four of these runs. Data points, below the FP detector saturation limit, could not be measured for run 15 because the curve was too steep.

As discussed in section 4.2, the slope of the breakthrough curve is related to the kinetic parameters by the following expression:

$$\frac{d\theta}{d\tau} = \beta' X y_b^* = \frac{\beta' k (1 - \varepsilon_v) y_b X}{v_o} \qquad 4.13a$$

where β', the modified effectiveness factor, replaces β in equation 4.13 when external mass transfer effects cannot be neglected.

Rearranging equation 4.13, the kinetic parameter $\beta' k$, is given by:

$$\beta' k = \left(\frac{d\theta}{d\tau}\right) \frac{v_o}{X(1 - \varepsilon_v) y_b} \qquad 6.2.1.1$$

This equation is further manipulated in Appendix 11 to give:

$$\beta' k = \left(\frac{d(C/C_o)}{dt}\right) \frac{\rho_s (1 - \varepsilon_p)}{X C_o} \qquad 6.2.1.2$$

Values of $\beta' k$ can be converted to βk using:

$$\beta k = \left[\frac{1}{\beta' k} - \frac{V_p}{k_f A_p} \right]^{-1} \qquad 4.16$$

where k_f is the mass transfer coefficient obtained from Figure 4.2.

Table 6.9: Experimental Data for Determination of Adsorption Capacities and $\beta' k$ Values ($\varepsilon_p = 0.28$ for all runs).

Run No.	12	15	16	17	18
Particle size (mm)	-0.841/+0.595	-0.297/+0.214	-0.841/+0.595	-0.297/+0.214	-0.841/+0.595
Temperature (°C)	872	872	802	798	803
Gas Flow Rate (mL/min)	94	94	94	99	201
Weight of Bed (g)	19.99	20.00	20.00	20.00	20.02
Room Temp. Inlet H_2S conc. (%)	0.255	0.255	0.255	0.242	0.254
Breakthrough Time (min)	38.3	26.6	47.0	39.1	20.7
Pe	0.402	0.143	0.428	0.169	0.949
k_m (cm/s)	1.92	1.73	1.81	1.62	3.47
Adsorption Capacity (g H_2S/g CeO_2)	6.4×10^{-4}	4.4×10^{-4}	7.8×10^{-4}	6.5×10^{-4}	7.3×10^{-4}
$\beta' k X (s^{-1})$	64.5	> 205	57.5	205	189

Sample calculations are provided in Appendix 11.

Maximum capacity is 9.9×10^{-2} g H_2S/g CeO_2 (at $X = 1$).

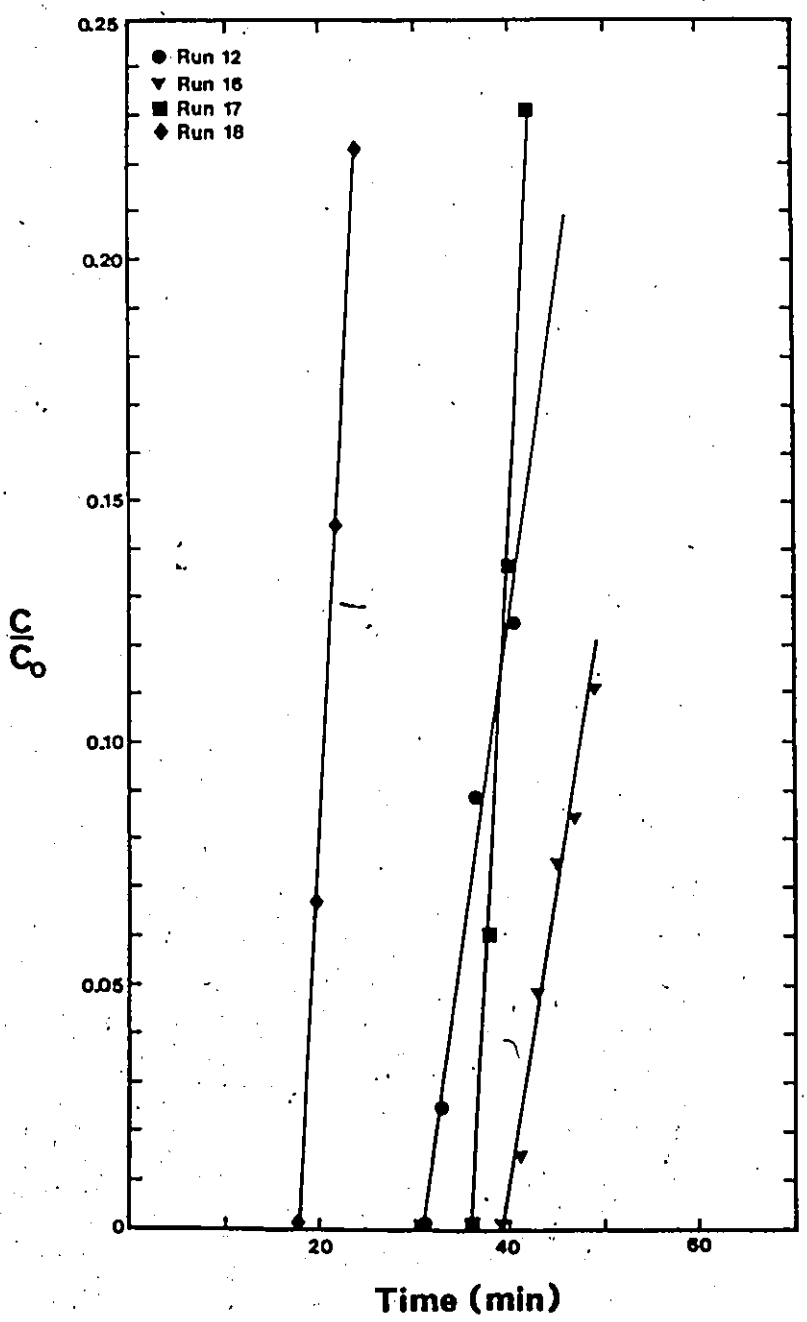

Figure 6.16: Breakthrough Curves for the Determination of the Effects of Temperature, Particle Size and Gas Flow Rate.

Although βk values should be compared rather than $\beta' k$ values, physically meaningful numbers could not be computed. A basic assumption of the constant pattern solution to the grain model equation, is that $0 = X$. Experimentally, breakthrough occurs at solid conversions of 0.004-0.008. Obviously, above these X values, $0 > X$, the model is not valid, and $\beta' k$ values have no physical signficance. Thus, to compute $\beta' k$ from equation 6.2.1.1, a value of X, below the adsorption capacity of the bed, must be selected. However, it was subsequently discovered that X must be greater than $\left|\left(\frac{V_p}{k_f A_p}\right)\left(\frac{d\theta}{dt}\right) v_o\right| / \left|(1-\varepsilon_v) y_b\right|$ in order to obtain a positive value for βk. Therefore, it was decided to compare $\beta' kX$ values for runs 12 through 17 since the k_m values were about the same.

A 2^2 factorial design was used to determine the effects of particle size and temperature (runs 12, 15, 16 and 17). For a constant particle size (runs 12 and 16 or runs 15 and 17) an increase in temperature increases the observed reaction rate and decreases the adsorption capacity. It was shown in section 6.2.1.4, that pore diffusion control is very significant. Thus, a larger reaction rate at the pore mouth would result in pore closure at earlier times, and a smaller adsorption capacity would be obtained.

For a constant temperature, the observed reaction rate significantly increases (as expected) when the particle size is decreased (compare runs 12 and 15 or runs 16 and 17). However, the increase in external surface area did not result in a larger adsorption capacity. Perhaps, the larger kinetic rate constants caused pore closure at earlier times.

The effect of gas flow rate was studied using the larger particle size at 1073 K. Breakthrough curves for high temperatures and small particle sizes were too steep to obtain measurable H_2S concentrations. The $\beta' kX$ values for runs 16 and 18 again illustrate that larger rates of reaction, owing to increased external mass transfer coefficients, results in lower adsorption capacities.

It is not recommended to base an industrial process on unsupported cerium oxide sorbents because of the low adsorption capacities. Although capacities are usually improved for small particles in a fluidized bed, powdered cerium oxides (–325 mesh or < 40 μm) were unsuitable for fluidized bed studies because of poor fluidization characteristics. Future experiments should be directed at improving the solid conversions by the use of an inert support, and obtaining the kinetic parameters for the new sorbent.

6.2.1.6 Analysis of Sulfur Loaded Sorbents

The sulfur loaded sorbent, in the fixed bed reactor, ranged from dark green at the reactor entrance to pale green at the exit. The green product, however, could not be identified by X-ray diffraction because it is amorphous.

TGA/DTA analysis of the darkest green material indicated a weight gain between 285-450°C owing to sulfate formation. Decomposition followed at 670-760°C. Further work is required to determine the possible solid phases (see sections 3.1.2 and 3.1.3) before identification is completed. The thermochemical analysis suggests that regeneration should be conducted above 760°C.

6.2.1.7 Supported Cerium Oxide Sorbents

A sorbent containing 14.3 wt% CeO_2 was prepared by impregnation of fused aluminum oxide (average pore radius = 2×10^{-6} m) with ammonium cerium nitrate (details in section 5.4.3). Examination of the impregnated sorbent, prior to calcination, indicated that the majority of the bright orange $(NH_4)_2$ $[Ce(NO_3)_6]$, was contained in an outer layer surrounding the fused aluminum oxide. Desulfurization conditions are summarized in Table 6.10. Comparison of the behaviour of the supported and unsupported sorbents showed a five-fold improvement in adsorption capacity (see Tables 6.11 and 6.9). Because most of the CeO_2

Table 6.10: Conditions Used for Experiments Using Supported Cerium Oxide Sorbents

Bed Height	12.6 cm
Bed Weight	14.22 g
Percent CeO_2	14.3%
Temperature	890°C

Table 6.11: Summary of Experimental Data for a Supported Cerium Oxide Sorbent

	Fresh Sorbent	Regenerated Sorbent
Flow rate (mL/min)	97	93
Inlet H_2S concentration (%)	0.25	0.28
Outlet H_2S concentration (ng S/mL)	2.7	2.7
Breakthrough time (min)	16.9	13.3
Adsorption Capacity (g H_2S/g CeO_2)	3.1×10^{-3}	2.1×10^{-3}
Percent CeO_2 Conversion	3.1	2.1

is on the external surface of the support, additional improvement in adsorption capacity should be obtained by lowering the percentage of CeO_2 impregnated, to the 1.0% range.

6.2.1.8 Conclusions from the Desulfurization Study

(1) Equilibrium points on the $CeO_{2-x}|Ce_2O_2S$ boundary were established at four temperatures using a gas mixture containing 55.0% CO, 10.8% CO_2, 33.0% H_2 and 1.2%H_2S. The results indicate that the $CeO_{2-x}|Ce_2O_2S$ boundary can be obtained by extending the $Ce_2O_3|Ce_2O_2S$ boundary.

(2) Reduction of CeO_2 to CeO_{2-x} enhances the reactivity of the cerium oxide sorbent by providing empty sites for the adsorption of sulfur.

(3) Low cerium oxide conversions were obtained at breakthrough, owing to pore closure by Ce_2O_2S. Further work should continue with a supported cerium oxide sorbent of about 1 wt%. The constant pattern solution of the grain model can be used to obtain the kinetic parameters for the supported sorbents under conditions similar to those used for the unsupported sorbents.

(4) Regeneration should be carried out above 760°C.

6.2.2 Regeneration

6.2.2.1 Regeneration in Air

Air was passed through the fixed bed, at 1145 K, to regenerate the sulfur loaded sorbent, releasing sulfur as SO_2:

$$Ce_2O_2S(s) + 2O_2(g) = 2\,CeO_2(s) + SO_2(g) \qquad 3.3.13$$

Data from a typical regeneration experiment is illustrated in Figure 6.17. The initial part of the curve shows that the SO_2 concentrations produced by the regeneration reaction are above

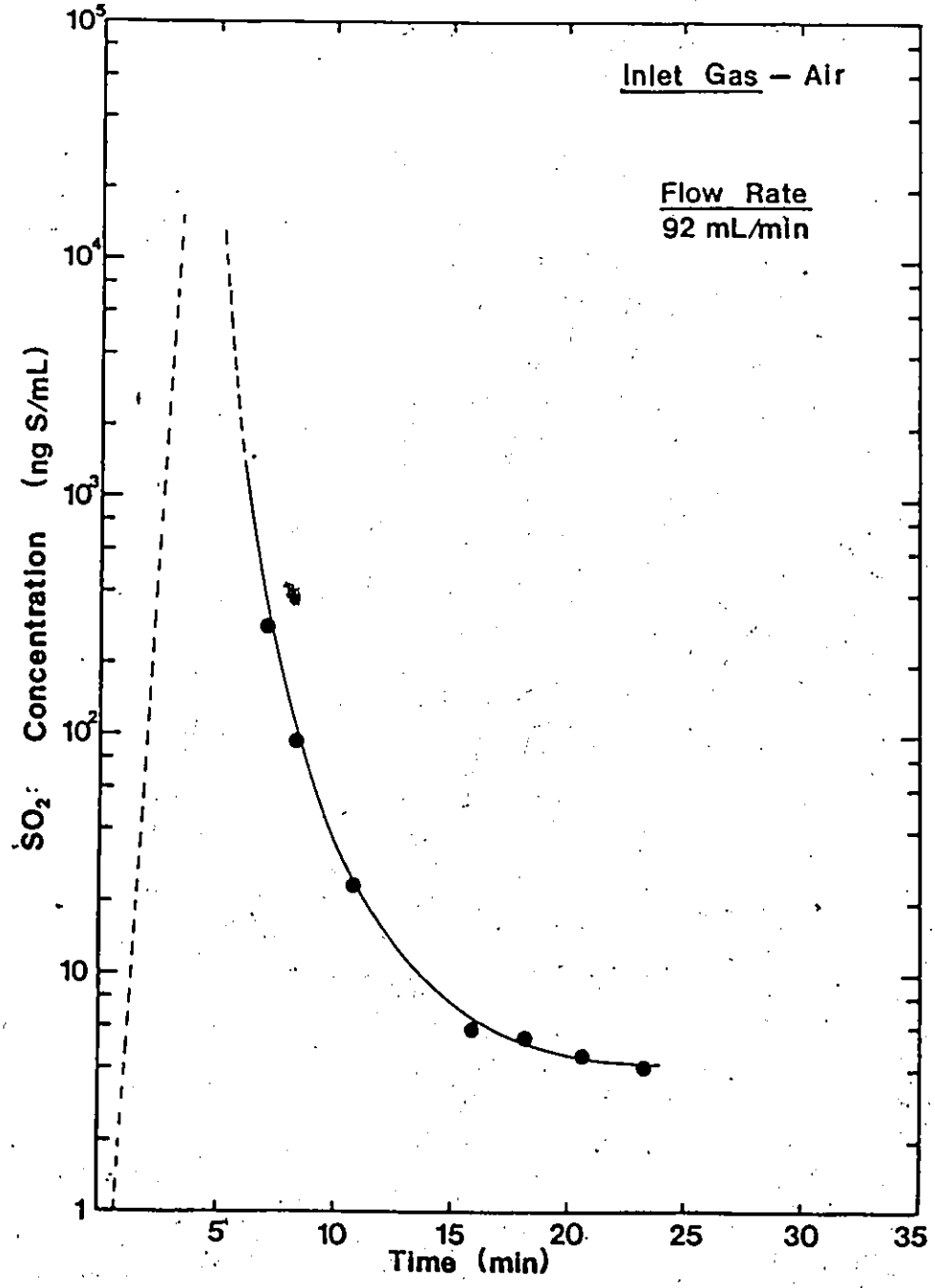

Figure 6.17: Typical Regeneration Curve in Air at 1145 K.

the detectability limit of the gas chromatograph (i.e. greater than 0.1%, see g.c. traces in Appendix 10). Regeneration was complete in about 5 minutes for air flow rates, approximately four times greater than the desulfurization flow rates. Figure 6.10 shows that the regenerated sorbent has 92% of the original adsorption capacity.

6.2.2.2 Reduction of Regenerated Sorbents

To activate the sorbent (see section 6.2.1.3), the regenerated solids were reduced with 5% H_2/95% N_2 before the next desulfurization cycle. Figure 6.18 shows that during this process, an additional release of SO_2 and H_2S occurs. The following reaction scheme explains these observations:

During regeneration in air, the large concentrations of SO_2 increase the sulfur potential of the gas phase, resulting in the formation of cerium sulfate:

$$2\,CeO_2(s) + 3\,SO_2(g) + O_2(g) = Ce_2(SO_4)_3(s) \qquad 6.2.2.1$$

$$\Delta G^\circ = -859.620 + 0.75280\,T\ kJ$$

$$K_{1100} = 31.43$$

Subsequent reduction in hydrogen converts the sulfate to the oxide and oxysulfide, releasing SO_2:

$$Ce_2(SO_4)_3(s) + 2(1+x)H_2(g) = 2CeO_{2-x}(s) + 3SO_2(g) + 2(1+x)H_2O(g) \qquad 6.2.2.2$$

$$Ce_2(SO_4)_3(s) + 6H_2(g) = Ce_2O_2S(s) + 2SO_2(g) + 6H_2O(g) \qquad 6.2.2.3$$

The Ce_2O_2S and H_2O, produced by reactions 6.2.2.2 and 6.2.2.3, react further to form H_2S:

$$Ce_2O_2S(s) + 2(1-x)H_2O(g) = 2CeO_{2-x}(s) + H_2S(g) + (1-2x)H_2(g) \qquad 6.2.2.4$$

The aforementioned reaction scheme, is more viable than an explanation based on the presence of residual Ce_2O_2S, since the latter cannot justify why a maximum in H_2S concentration is reached after the SO_2 concentration begins to decrease.

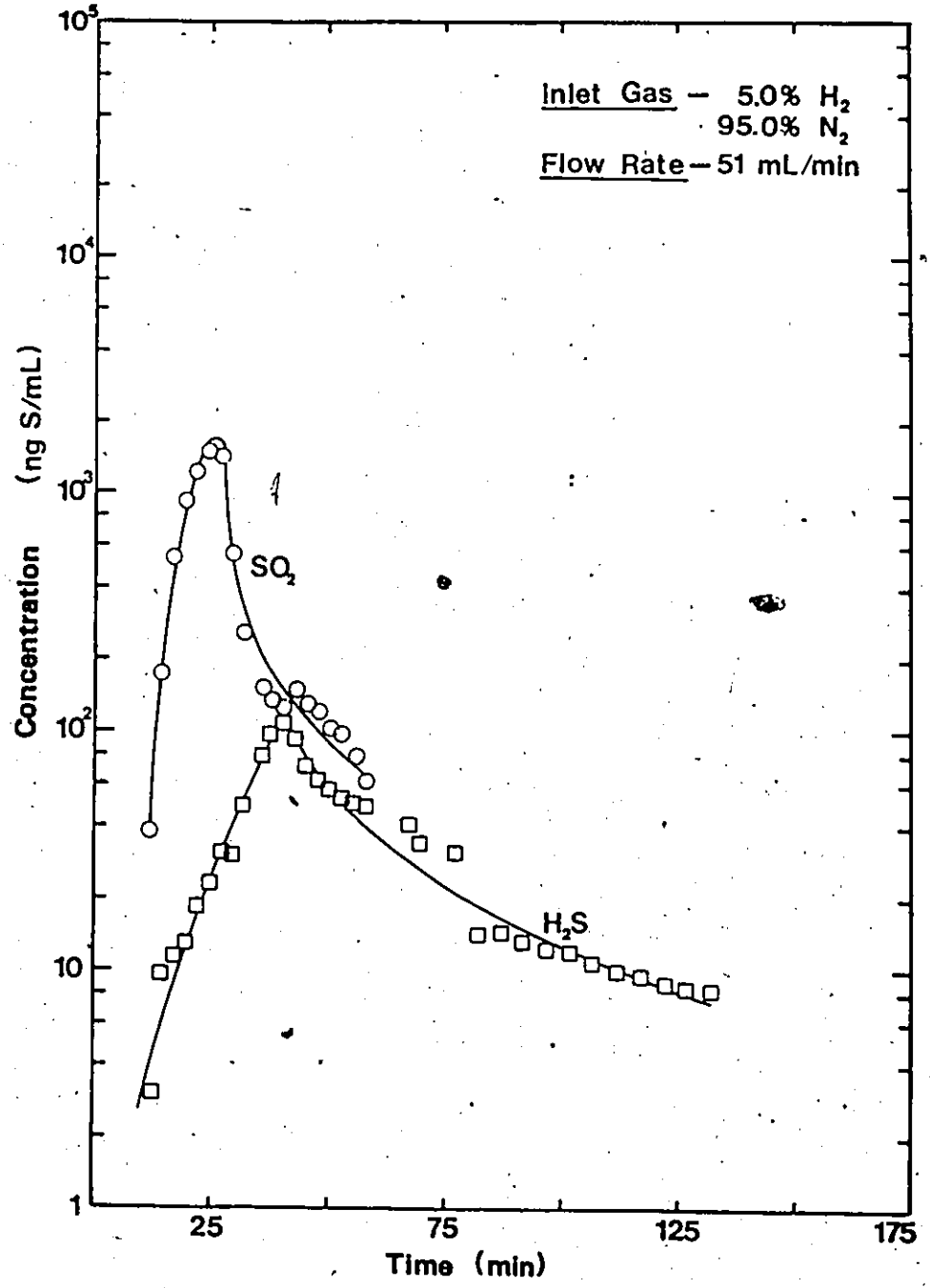

Figure 6.18: Reduction Curve for Regenerated Cerium Oxide Sorbents at 1145 K.

Equations 6.2.2.1-6.2.2.4 can be used to explain the Longo process described in section 2.2.3. In the desulfurization of flue gases, SO_2 reacts with CeO_2 to form $Ce_2(SO_4)_3$ or $CeOSO_4$. The formation of oxysulfate is possible because the process temperatures are lower (500-800°C). During regeneration in hydrogen, Longo noted that SO_2 is produced initially, and after 50% regeneration, H_2S is the major species. The reduction of cerium sulfate explains these observations.

Conclusions from the reduction study of regenerated cerium oxide sorbents can also be applied to the desulfurization/regeneration characteristics of calcined bastnaesite concentrates. Figure 6.19 shows the desulfurization curves obtained by Kay (10) for bastnaesite concentrate 4100. Of particular interest is the decrease in desulfurization efficiency (measured with H_2S Dräeger tubes) at the 20-30 minute mark. Since 41-45% of the concentrate consists of CeO_2, the drop in efficiency can be explained by the formation of $Ce_2(SO_4)_3$ during air regeneration and subsequent reduction by hydrogen in the coal gases.

6.2.2.3 Conclusions from the Regeneration Study

(1) Air can be used to regenerate the sorbent.

(2) A small amount of cerium sulfate is formed during air regeneration, which subsequently releases SO_2 and H_2S during the reduction step. The proposed chemical reactions can be used to explain the regeneration reactions in the Longo process and the initial drop in desulfurization efficiency of regenerated bastnaesite concentrates.

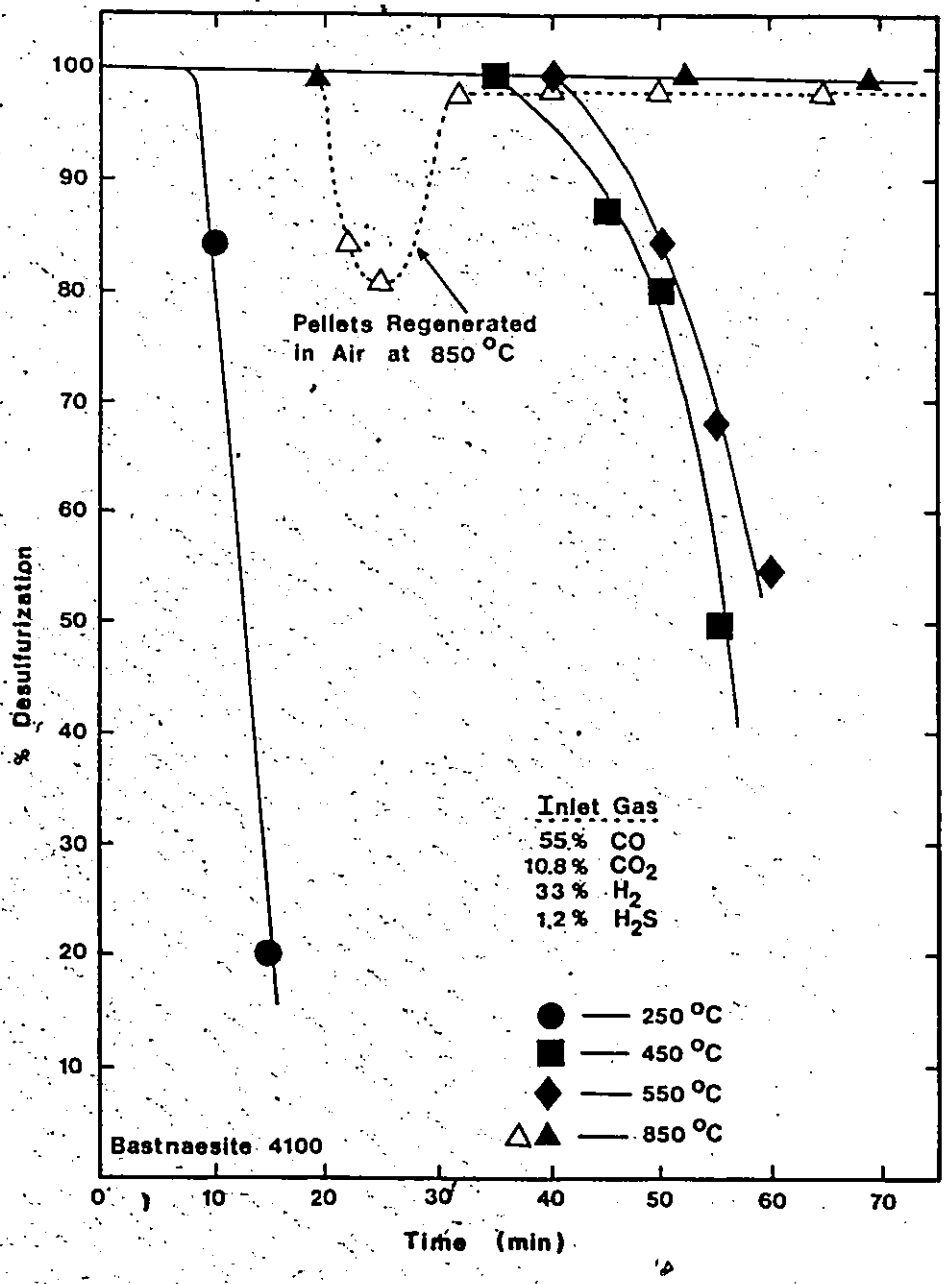

Figure 6.19: Desulfurization Curves for Bastnaesite Concentrate 4100 (10).

6.3 Comparison of the Cerium Oxide, Iron Oxide and Calcium Oxide Desulfurization Processes

The phase stability diagrams for the Fe-O-S, Ce-O-S and Ca-O-S systems are given in Figures 6.20, 6.21 and 6.22, respectively. The diagrams show that:

(1) Cerium oxide sorbents reduce H_2S concentrations to the lowest levels because the CeO_{2-x}/Ce_2O_2S boundary gives the lowest p_{S_2} for a given p_{O_2}.

2) Cerium oxides are regenerated easily because the $Ce_2(SO_4)_3$ phase is comparatively less stable than the iron or calcium sulfates. In section 2.2.2, it was mentioned that calcium oxide sorbents are very difficult to regenerate. The relatively high position of the $CaO/CaSO_4$ boundary shows that the sulfate is difficult to decompose under atmospheric conditions.

(3) Cerium oxide sorbents are not reduced to the metallic phase until very low oxygen partial pressures are reached. In comparison, iron oxide is reduced to metallic iron for $p_{O_2} < 10^{-22}$.

In addition, cerium oxide sorbents can be used up to 1200°C (1473 K) before sintering begins, whereas iron oxides can only be used up to 1033 K. This is an advantage for coal gases leaving a Koppers-Totzek gasifier, where exit temperatures are about 1273 K.

Although cerium oxide sorbents are more expensive than iron oxide sorbents, limestones or dolomites, they are more readily regenerated than calcium oxide sorbents and can be used under conditions which are unfavourable for iron oxide sorbents.

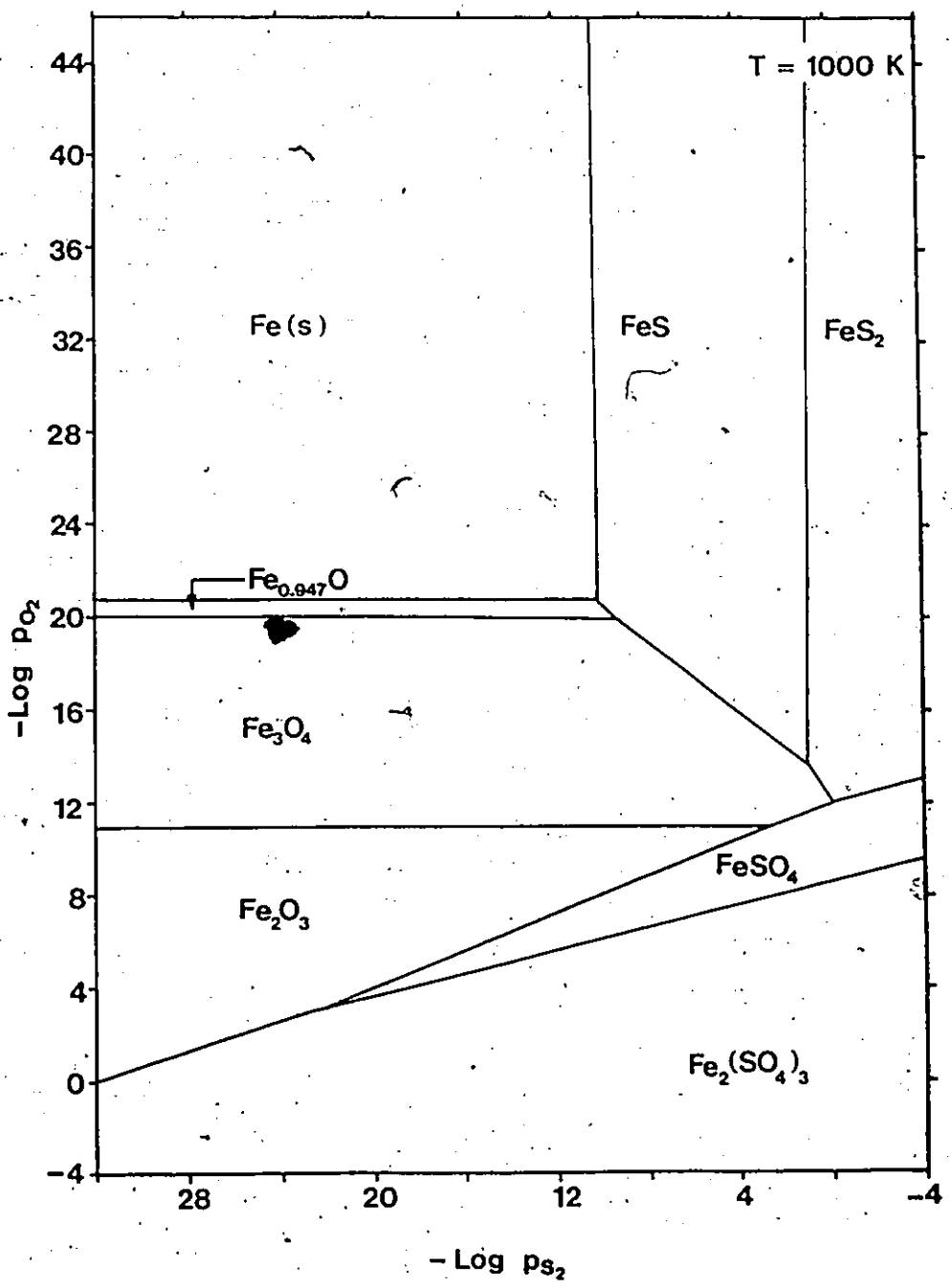

Figure 6.20: The Fe-O-S Phase Stability Diagram at 1000 K (30).

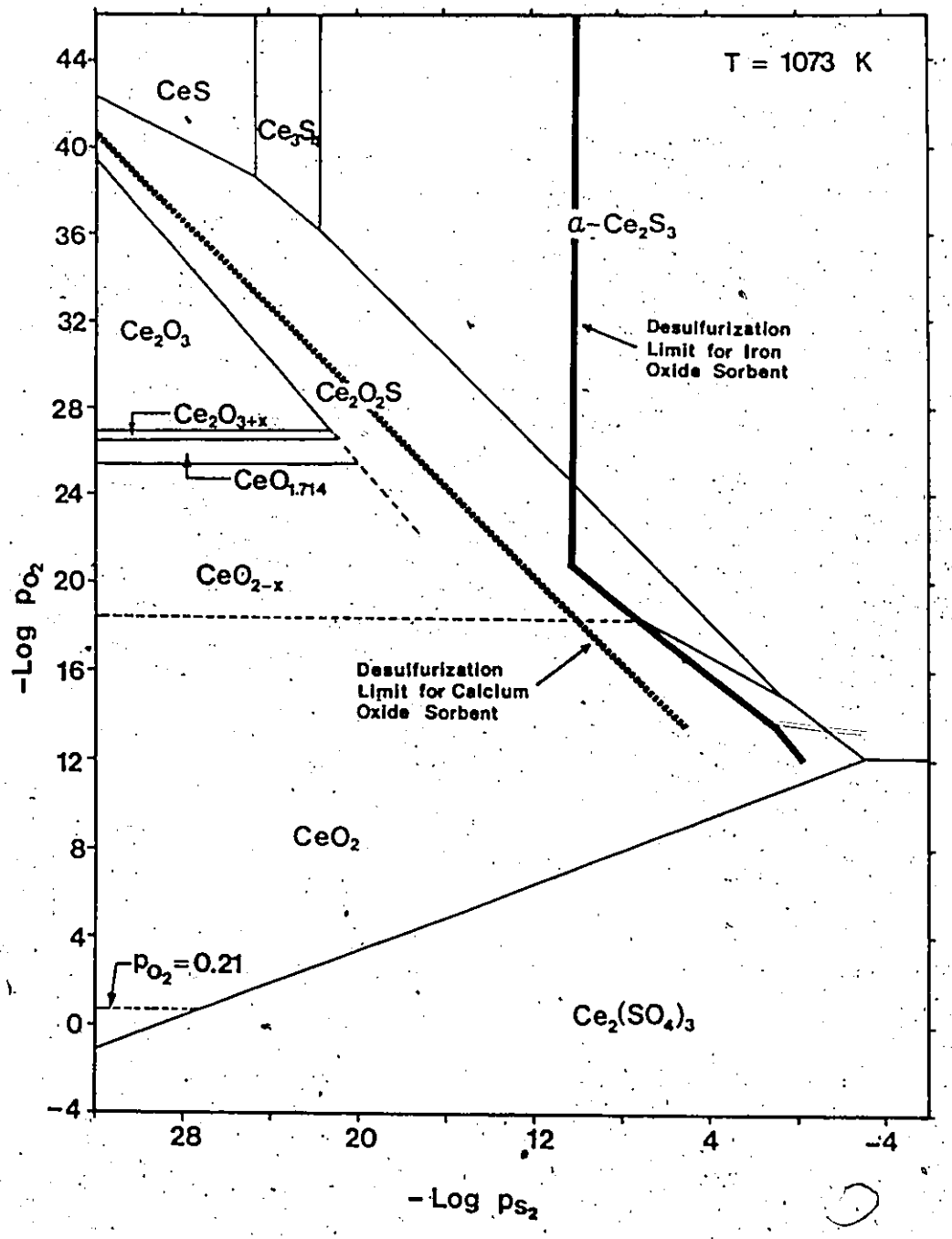

Figure 6.21: The Ce-O-S Phase Stability Diagram at 1073 K.

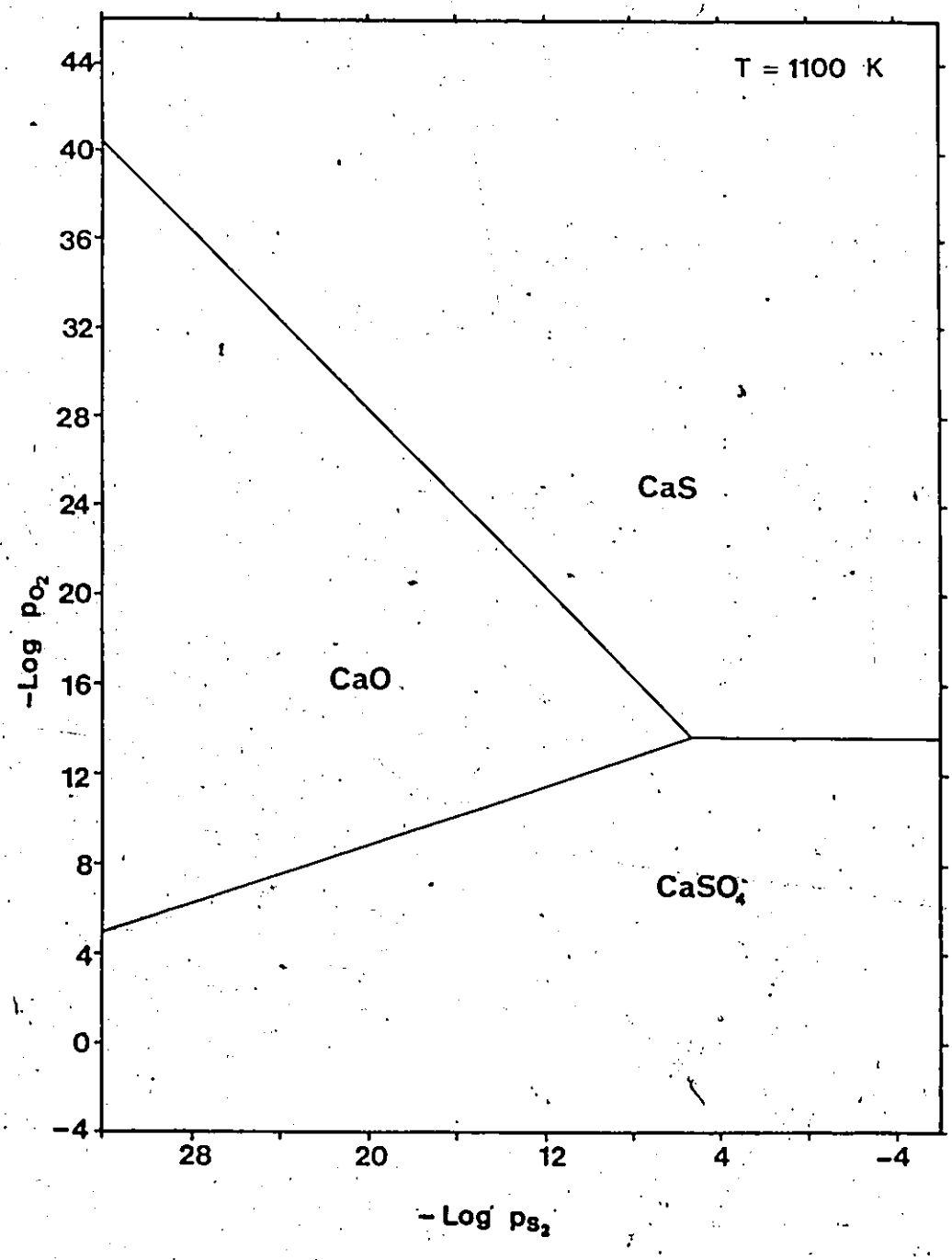

Figure 6.22: The Ca-O-S Phase Stability Diagram at 1100 K (100).

Chapter VII

SUMMARY AND CONCLUSIONS

With reference to the total program diagrammatically presented in Figure 1.1, Chapter 1, the major conclusions of this study are summarized below.

Characterization Studies

Uncalcined bastnaesite concentrates consist of a mixed rare earth hydroxy-fluorocarbonate, $RE(OH)_{1-x}F_xCO_3$ (RE = primarily Ce, La) where $x = 0.56 \pm 0.01$. A solid solution of REOF and CeO_2, with a fluorite type structure, is produced upon calcination. Concentrates can be used up to temperatures of 1000°C without loss in surface area. Further changes in composition are not observed.

Reduction Studies

Cerium forms a range of non-stoichiometric oxides between 800 and 1000°C: CeO_2, CeO_{2-x}, $CeO_{1.714}$, Ce_2O_{3+x} and Ce_2O_3. The formation of the blue oxide, CeO_{2-x}, is favoured in gas mixtures with a CO/CO_2 ratio of ~10/1 (typical of CO/CO_2 ratios in coal gases) within the above temperature range. LaOF is unreactive under reducing conditions; however, calcined bastnaesite concentrates can be readily reduced. The presence of dissolved CeO_2 is believed to be responsible for the reduction characteristics of bastnaesite concentrates, and in carbon monoxide, the quadravalent cerium is fully converted to the Ce^{3+} form.

Pyrohydrolysis Studies

Equilibrium constants for the pyrohydrolysis of LaOF and CeOF were determined to be 1.23×10^{-10} and 2.52×10^{2}, respectively, at 1100K. Thermodynamic calculations indicate that the less stable CeOF phase would have hydrolysed to CeO_2 during calcination, whereas, LaOF does not significantly hydrolyse during calcination, reduction, desulfurization or regeneration. These results provide further quantitative arguments for the existence of a solid solution of $REOF/CeO_2$ in calcined bastnaesite concentrates.

The activation energy for the reaction of bastnaesite concentrate 4100 with steam is 121. ± 15 kJ/mol.

Desulfurization Studies

The Ce-O-S phase stability diagram was completed with the best available data for the various oxide and sulfate phases in the temperature range 800-1023°C. A computer program (72,73) was used in conjunction with the phase stability diagram to predict the solid and gaseous products of reaction for a typical coal gas. The predicted desulfurization reaction is:

$$CeO_{2-x} + H_2S + (1 - 2x)H_2 = Ce_2O_2S + 2(1 - x)H_2O \qquad 3.3.5$$

The position of the CeO_{2-x}/Ce_2O_2S boundary was established at four temperatures for one gas composition. Desulfurization proceeds only with reduced sorbents, which suggests that oxygen vacancies within the solid facilitate the adsorption of sulfur from the gas phase. A fixed bed of cerium oxide sorbent verified the viability of the process by removing 99.98% of the H_2S from a simulated coal gas. The sulfur capacity increased with decreasing temperature, decreasing particle size and with increasing gas velocity. Low adsorption capacites were obtained due to pore closure by Ce_2O_2S and because of significant pore diffusion resistance. Capacities can be increased by using a support.

Regeneration Studies

Regeneration of cerium oxide sorbents, in air, under similar temperatures and pressures, occurs readily with the evolution of SO_2:

$$Ce_2O_2S + O_2 = CeO_2 + SO_2 \qquad 3.3.13$$

Due to the large concentration of SO_2 produced during regeneration, minor quantities of sulfate are formed. In the subsequent reduction cycle, the sulfate decomposes to SO_2 and H_2S, the former reaching a maximum in concentration before the latter. The reduction of the sulfate to the oxysulfide is believed to be responsible for these observations.

$$Ce_2(SO_4)_3 + 2(1 + x)H_2 = 2CeO_{2-x} + 3SO_2 + 2(1 + x)H_2O \qquad 6.2.2.2$$

$$Ce_2(SO_4)_3 + 6H_2 = Ce_2O_2S + 2SO_2 + 6H_2O \qquad 6.2.2.3$$

$$Ce_2O_2S + 2(1 - x)H_2O = 2CeO_{2-x} + H_2S + (1 - 2x)H_2O \qquad 6.2.2.4$$

Solids which are regenerated and reduced can be used effectively for subsequent desulfurization cycles.

Comparison of Desulfurization Processes

Advantages of high temperature desulfurization processes based on cerium oxides over similar technologies based on iron oxides, limestones or dolomites are three-fold:

1) Cerium oxides can be used for the desulfurization of more strongly reducing gases than iron oxides.

2) Cerium oxides are more readily regenerated than calcium oxide based sorbents.

3) Cerium oxide sorbents can be used at higher temperatures than iron oxide sorbents.

7.1 Recommendations for Future Work

To complete the investigation of the desulfurization and regeneration characteristics of bastnaesite concentrates, the following studies are recommended:

Thermodynamic Studies

(1) The free energies of formation of the rare earth thiofluorides should be determined to enable the calculation of the equilibrium constants for the reaction:

$$REOF(s) + H_2S(g) = RESF(s) + H_2O(g) \qquad 6.1.4$$

(2) The stabilities, compositions and thermodynamic properties of the various cerium sulfates and oxysulfates should be resolved. In particular, the free energy of formation of $CeOSO_4$ and its thermal decomposition properties should be determined to complete the Ce-S-O phase stability diagram.

(3) A series of gas mixtures with differing CO/CO_2 gas ratios should be used to determine additional points on the CeO_{2-x}/Ce_2O_2S phase boundary.

Kinetic Studies

(1) Supported cerium oxide sorbents, of about 1 wt%, should be used to generate breakthrough curves. The model presented by Wang (80), can be used to determine the rate constants.

(2) The effect of reduction time upon reactivity and capacity should be determined.

(3) The desulfurization/regeneration characteristics of a fixed bed of LaOF or $LaOF/CeO_2$ solid solutions of varying proportions, should be studied and compared to bastnaesite.

(4) The techniques used in this study could be extended to the desulfurization of oxidizing gas streams containing SO_2 (e.g. flue gases).

(5) The effect of oxygen concentration upon regeneration efficiency should be studied.

REFERENCES

1. Petrie, T.W.; Rhodes, W.J.; C.E.P., V 75, n 6, 73 (1979)
2. Longo, J.M.; U.S. Patent 4,001,375; Jan. 4, 1977.
3. Longo, J.M.; U.S. Patent 4,251,496; Feb. 17, 1981.
4. Wheelock, K.S.; Aldridge, C.L.; U.S. Patent 3,974,256; Aug. 10, 1976.
5. Wheelock, K.S.; Say, G.R.; U.S. Patent 4,002,720; Jan. 11, 1977.
6. Baron, K.; McArthur, D.P.; U.S. Patent 4,311,581; Jan. 19, 1982.
7. Wilson, W.G.; Kay, D.A.R.; U.S. Patent 4,161,400; July 17, 1979.
8. Wilson, W.G.; Kay, D.A.R.; U.S. Patent 4,224,058; Sept. 23, 1980.
9. Ghosh, D.; Kay, D.A.R.; "The Behaviour of Cerium in Liquid Iron Containing Sulfur and Oxygen"; Paper presented at the 12th. Rare Earth Conference, Vail, Colorado, July 1976.
10. Kay, D.A.R.; private communication, "Gaseous Desulfurization Using Rare Earth Oxides", Internal Report, June 1, 1977-Jan. 31, 1978.
11. Kay, D.A.R.; private communication, "Gaseous Desulfurization Using Rare Earth Oxides", Internal Report, Feb. 1-May 31, 1978.
12. Hagopian, C.; "Desulfurization Using Rare Earth Oxides"; B.Sc. Thesis, McMaster University, April 1978.
13. Scepanovic, V.; Kay, D.A.R.; private communication.
14. Giacomelli, G.F.; "Pyrohydrolysis of Rare Earth Ore Concentrates for Desulfurization Purposes"; B.Sc. thesis, McMaster University, April 1980.
15. Hong, Y.; private communication to be published.
16. Dwivedi, R.; "Determination of Thermodynamics of Rare Earth-Oxygen-Sulfur systems at High Temperature"; Ph.D. dissertation, McMaster University, July 1982.
17. Michaels, H.J.; Leonard, H.F.; C.E.P., V 74, n 8, 85 (1978).
18. Howard-Smith, I.; Werner, G.J.; "Coal Conversion Technology"; Noyes Data Corp., N.J. (1976).

19. Kirk-Othmer Encyclopedia of Chemical Technology, V 10, 2nd edition, John Wiley and Sons, Inc., 353 (1966).

20. Jahnig, C.E.; Bertrand, R.R.; C.E.P, V 72, n 8, 51 (1976).

21. Timmins, C.; Gas Eng. Management, V 20, n 2, 81 (1980).

22. Merer, R.D.; Wood, C.E.; CIM Bulletin, 71, June 1978.

23. "Gas Engineers' Handbook", Chapters 3, 7, 9; Industrial Press, N.Y. (1965).

24. Reeve, L.; J. Inst. Fuel, V 31, 319 (1958).

25. Phillipson, J.J.; "Desulfurization", Catalyst Handbook, Wolf, London (1970).

26. Perry and Chilton: Chemical Engineers Handbook.

27. Westmoreland, P.R.; Harrison, D.P.; Environ. Sci. and Technol., V 10, n 7, 659 (1976).

28. Maddox, R.N.; "Gas Conditioning and Processing", Campbell Petroleum Series, Oklahoma, 337 (1974).

29. Mohan, C.P.; "Fuel-Gas Desulfurization at High Temperatures in Fluidized-Beds Using Gasifier Bottoms Ash"; Ph.D. dissertation, University of Kentucky, 1981.

30. Schrodt, J.T.; Mohan, C.P.; AIChE Symposium Series, V 77, n 211, 1 (1981).

31. Schrodt, J.T.; "Hot Gas Desulfurization with Gasifier Ash Sorbents", Proceedings of the Symposium on Potential Health and Environmental Effects of Synthetic Fossil Fuel Technologies, 32, July 1979.

32. Gas Engineers' Handbook, Chapter 8, 95, Industrial Press, N.Y. (1965).

33. O'Neill, E.P.; Keairns, D.L.; AIChE Symposium Series, V 73, n 161, 100 (1977).

34. Hartman, M.; Coughlin, R.W.; Ind Eng. Chem., Process Des. Develop.; V 13, n 3, 248 (1974).

35. Hartman, M.; Coughlin, R.W.; AIChE Journal; V 22, n 3, 490 (1976).

36. Hubble, B.R. et al.; Air Poll. Control Ass. Journal, V 25, n 12, 1256 (1975).

37. Yang, R.T.; Shen, M.S.; AIChE Journal, V 25, n 3, 547 (1979).

38. Nemeth, E.J.; McGreal, J.E.; U.S. Patent 4,212,851, July 1980.

39. Handbook on the Physics and Chemistry of Rare Earths, Volume 3: Non-Metallic Compounds I; K.A. Gschneidner, Jr. and L. Eyring, Editors, North Holland Publ.; Chapter 27 (1979).

40. Sorensen, O.T.; J. Solid State Chem., V 18, 217 (1976).

41. Bevan, D.J.M.; Kordis, J.; J. Inorg. Nucl. Chem.; V 26, 1509 (1964).

42. Gschneidner, K.A., Jr.; Verkade, M.E.; "Selected Cerium Phase Diagrams"; Report No. IS-RIC-7, Rare Earth Information Center, Ames, Iowa (1974).

43. Besançon, P.; J. Solid State Chem., V 7, 232 (1973).

44. Marcon, J.P.; Pascard, R.; J. Inorg. Nucl. Chem., V 28, 2551 (1966).

45. Klinvex, S.H.; Berger, J.A.; U.S. Clearinghouse Fed. Sci. Tech. Inform. AD646011, CFSTI, 90 pp. (1966).

46. Faber, J., Jr.; "X-ray and Neutron Diffraction Studies of the Defect Structure in Nonstoichiometric Cerium Oxide"; Ph.D. dissertation, Marquette University, Milwaukee, Wisconsin (1973).

47. Panlener, R.J., et al.; J. Phys. Chem. Solids, V 36, 1213 (1975).

48. Steele, B.C.H.; Floyd, J.M.; Proc. Brit Ceram. Soc., n 19, 55 (1971).

49. Zachariasen, W.H.; Acta Crystallogr., V 2,. 60 (1949).

50. Wichelhaus, W.; Angew. Chem. Int. Ed. Engl., V 17, n 6, 451 (1978).

51. Guittard, M.; Dugué, J.; C.R. Acad. Sc. Paris, Ser. C., V 287, n 5, 173 (1978).

52. Duval, C.; Anal. Chim. Acta, V 15, 223 (1956).

53. Lóránt, B.; Z. Anal. Chem., V 219, n 3, 256 (1966).

54. Omer, S.S. Al. et al.; Thermochimica Acta, V 49, 259 (1981).

55. Lundgren, G.; Arkiv. Khemi, V 6, 59 (1954).

56. Gillespie, R.J.; Can. J. Chem., V 39, 2336 (1961).

57. Lindgren, G.; Acta Crystallogr., Sect. B., V 32, n 12, 3347 (1976).

58. Trofimov, G.V.; Belokoskov, V.I.; Zh. Neorg. Khim., V 13, n 1, 260 (Russ.), (1968).

59. Trofimov, G.V.; Zh. Neorg. Khim., V 13, n 10, 2831 (Russ.), (1968).

60. Nathans, M.W.; Wendlandt, W.W.; J. Inorg. Nucl. Chem.; V 24, 869 (1962).

61. Gschneidner, K.A.; Kippenhan, N.; McMasters, O.D.; Report No. IS-RIC-6, Rare Earth Information Center, Ames, Iowa.

62. Gschneidner, K.A.; Kippenhan, N.; Report No. IS-RIC-5, Rare Earth Information Center, Ames, Iowa.

63. Vahed, A.; Kay, D.A.R.; Metallurgical Transactions B, V 78, 375 (1976).

64. Barin, I.; Knacke, O.; Kubaschewski, O.; "Thermochemical Properties of Inorganic Substances", V 1, V 2, Supplement (1977).

65. Ulrichson, D.L.; Mahoney, D.J.; Chem. Eng. Sci., V 35, 567 (1980).

66. Williams, H.P.; Winefordner, J.D.; J. Gas Chromatography, V 4, 271 (1966).

67. Stirling, P.H.; Baird, M.H.I.; Proc. ISA Instrumentation Symp., Charleston, W. Va., 115, May 1962.

68. Bruner, F. et al.; Anal. Chem., V 44, n 12, 2070 (1972).

69. Bruner, F. et al.; Anal. Chem., V 45, n 9, 1790 (1973).

70. Bruner, F. et al.; Anal. Chem., V 47, n 1, 141 (1975).

71. Souza, T.L.C.; Bhatia, S.P.; Anal. Chem., V 48, n 14, 2234 (1976).

72. Thompson, W.T.; Bale, C.W.; Pelton, A.D.; Journal of Metals, V 32, n 12, 18 (1980).

73. Thompson W.T.; et. al.; F*A*C*T User Manuals, McGill University/Ecole Polytechnique, Montreal, Quebec, Canada, First Edition, June 1979.

74. Szekely, J.; Evans, J.W.; Sohn, H.Y.; "Gas-Solid Reactions", Academic Press, New York, 1976.

75. Hulburt, H.M.; "Chemical Reaction Engineering Reviews", Chapter 2, p. 26 (Advances in Chemistry Series, 148, ACS), Washington, D.C. (1975).

76. Levenspiel, O.; Chem. Eng. Sci. V 35, p. 1821 (1980).

77. Ramachandran, P.A.; Smith, J.M.; AIChE Journal, V 23, n 3, p. 353 (1977).

78. Evans, J.W.; Song, S.; Ind. Eng. Chem. Process Des. Develop., V 13, n 2, p. 146 (1974).

79. Ranade, M.G.; Evans, J.W.; I&EC, Process Des. Develop., V 19, p. 118 (1980).

80. Wang, M.; "High Temperature Hydrogen Sulfide Removal with an Iron-Oxide-Alumina Sorbent", Ph.D. dissertation, University of California, Berkeley (1980).

81. Fedkiw, P.S.; "Mass Transfer Controlled Reactions in Packed Beds at Low Reynolds Numbers"; Ph.D. dissertation, University of California, Berkeley (1978).

82. Donnay, G.; Donnay, J.D.H.; Am. Mineralogist, V 38, 932 (1953).

83. Kilbourn, B.T.; private communication, November 1983.

84. Glass, J.J.; et al.; Am. Mineralogist, V 43, 460 (1958).

85. Shaw, V.E.; U.S. Bureau of Mines, Rept. Invest. no. 5474 (1959).

86. Haschke, J.M.; J. Solid State Chem., V 12, 115 (1975).

87. Handbook on the Physics and Chemistry of Rare Earths, Volume 3: Non-Metallic Compounds I: Chapter 28; K.A. Gschneidner, Jr., and L. Eyring, Editors, North Holland Publ. (1979).

88. Niihara, K.; Yajima, S.; Bull. Chem. Soc. Japan; V 45, n 1, 20 (1972).

89. Pistorius, C.W.F.T.; J. Less-Common Metals; V 31, 119 (1973).

90. Aumont, R.; et al.; C.R. Acad. Sc. Paris, Ser. C., V 272, 314 (1971).

91. Finkelburg, W.; Stein, A.; J. Chem. Phys., V 18, 1296 (1950).

92. Pannetier, J.; Lucas, J.; C.R. Acad. Sc. Paris, Ser. C., V 268, 604 (1969).

93. Powell, R.H.; Menis, O.; Anal. Chem., V 30, n 9, 1546 (1958).

94. Vogel, A.I.; "A Textbook of Quantitative Inorganic Analysis: Theory and Practice", Longmans, Green and Co., 2nd Edition, 393-395 (1951).

95. Meng, V.V.M.; High Temperature Gaseous Desulfurization Using Bastnaesite Concentrates – Research Proposal, January 1980.

96. "SPADNS Method of Fluorine Determination"; private communication: Hamilton Municipal Labs., Woodward Avenue, Hamilton, Ontario (1980).

97. Schmidt, R.; Hahan, H.; Z. Anorgan. Allgem. Chem., V 373, 168 (1970).

98. Verkhovets, M.N.; Kamarzin, A.A., ; Isv. Sib. Otd. Akad. Nauk SSSR, Ser. Khim Nauk, n 4-6, 125 (1973).

99. Hewlett Packard 5830 A Gas Chromatograph User Manual (1978).

100. Kumar, V.; "Use of Calcia Stabilized Zirconia and β-Iβ"-alumina solid electrolytes in galvanic cells", Ph.D. Thesis, McMaster University (1984).

101. Johnson, G.W.; Sisneros, T.E.; "The Rare-Earths in Modern Science and Technology", Volume 3; McCarthy, Silber and Rhyne, Editors; Plenum Publishing Corp.; p. 525-529 (1982).

APPENDIX I

Sample Thermodynamic Calculations for the Ce-O-S Phase Stability Diagram

Calculation of Free Energy of Formation of $Ce_2(SO_4)_3$

The following thermodynamic values were obtained from Barin, Knacke and Kubaschewski (64).

TABLE A1.1: Enthalpies and Entropies of Relevant Compounds

Compounds	H (1000 K) cal	S (1000 K) cal/K
$Ce_2(SO_4)_3(s)$	-885663	166.176
Ce(s)	6103	26.299
$O_2(g)$	5387	58.167
$S_2(g)$	36775	64.636

For the reaction,

$$2\,Ce(s) + 6\,O_2(g) + 3/2\,S_2(g) = Ce_2(SO_4)_3(s) \qquad A1.1$$

the standard enthalpy and entropy of reaction are given by:

$$\Delta H^\circ_{f,1000} = H(Ce_2(SO_4)_3) - 2\,H(Ce) - 6\,H(O_2) - 3/2\,H(S_2)$$

$$= -885663 - 2(6103) - 6(5387) - 3/2(36775)$$

$$= -985,353.5 \text{ cal/mol}$$

$$\Delta S^\circ_{f,1000} = 166.176 - 2(26.299) - 6(58.167) - 3/2(64.636)$$

$$= -332.378 \text{ cal} \cdot \text{mol}^{-1} \cdot \text{K}^{-1}$$

Therefore,

$$\Delta G^\circ_f = -985{,}354 + 332.38T \text{ cal} \cdot \text{mol}^{-1} \quad (900 - 1071\text{K})$$

or

$$\Delta G^\circ_f = -4122.04 + 1.3904T \text{ KJ} \cdot \text{mol}^{-1} \qquad \text{A1.2}$$

Above 1071 K, equation A1.2 must be modified to account for the transformation of Ce(s) to Ce(ℓ).

$$2\,Ce(\ell) = 2\,Ce(s) \quad \Delta G^\circ_{tr} = -2610 + 2.436T \text{ cal}$$

For

$$2\,Ce(\ell) + 6\,O_2(g) + 3/2\,S_2(g) = Ce_2(SO_4)_3(s) \qquad \text{A1.3}$$

the standard free energy equation becomes

$$\Delta G^\circ = -987{,}964 + 344.81T \text{ cal} \cdot \text{mol}^{-1}$$

or

$$\Delta G^\circ = 4132.95 + 1.3881T \text{ KJ} \cdot \text{mol}^{-1} \quad (1071 - 1273\text{K}) \qquad \text{A1.4}$$

Equations Defining Boundaries

The $CeO_2/Ce_2(SO_4)_3$ phase boundary was calculated as follows:

$$Ce_2(SO_4)_3(s) = 2\,Ce(\ell) + 6O_2(g) + 3/2\,S_2(g) \quad \Delta G^\circ_1 = 987{,}964 - 334.81\,T \text{ cal}$$

$$2\,Ce(\ell) + 2\,O_2(g) = 2\,CeO_2(s) \quad \Delta G^\circ_2 = -519{,}800 + 99.0\,T \text{ cal}$$

Adding the two equations:

$$Ce_2(SO_4)_3(s) = 4\,O_2(g) + 3/2\,S_2(g) + 2\,CeO_2(s)$$

$$\Delta G^\circ_3 = 486{,}164 - 235.81\,T \text{ cal}$$

or

$$\Delta G^\circ_3 = 1958.48 - 0.98648\,T \text{ kJ}$$

$$K = p_{O_2}^{\,4}\, p_{S_2}^{\,3/2} \text{ and } \log K_{eq} = -\Delta G^\circ_3/(2.303\,RT)$$

Thus,

$$4 \log p_{O_2} + 3/2 \log p_{S_2} = (-468164 + 235.81T)/(2.303\,RT)$$

$$\log p_{O_2} = -\frac{3}{8} \log p_{S_2} - \frac{25576.8}{T} + 12.88 \qquad \text{A1.5}$$

The CeO_2/Ce_2O_2S, $Ce_2S_3/Ce_2(SO_4)_3$ and CeO_2/Ce_2S_3 phase boundaries were calculated similarly and are summarized in Table 3.4 (see section 3.1.5).

The boundaries between the cerium oxide phases were determined as described in section 3.1.5. Table A1.2 summarizes the values used in plotting the Ce-O-S diagrams given in Figures 3.2 and 6.12 to 6.15.

TABLE A1.2: Data from Bevan and Kordis (41) used for Ce-O-S Phase Stability Diagrams

	Boundary			
	Ce_2O_3/Ce_2O_{3+x}	$Ce_2O_{3+x}/CeO_{1.714}$	$CeO_{1.714}/CeO_{2-x}$	CeO_{2-x}/CeO_2
T(K)	Values of $-\log p_{O_2}$			
1296	20.31	19.76	19.76	9.69
1244	21.79	21.20	20.88	10.38
1189	23.13	22.64	22.33	13.0
1145	24.67	24.0	23.40	15.0
1073	26.96	26.63	25.56	18.55

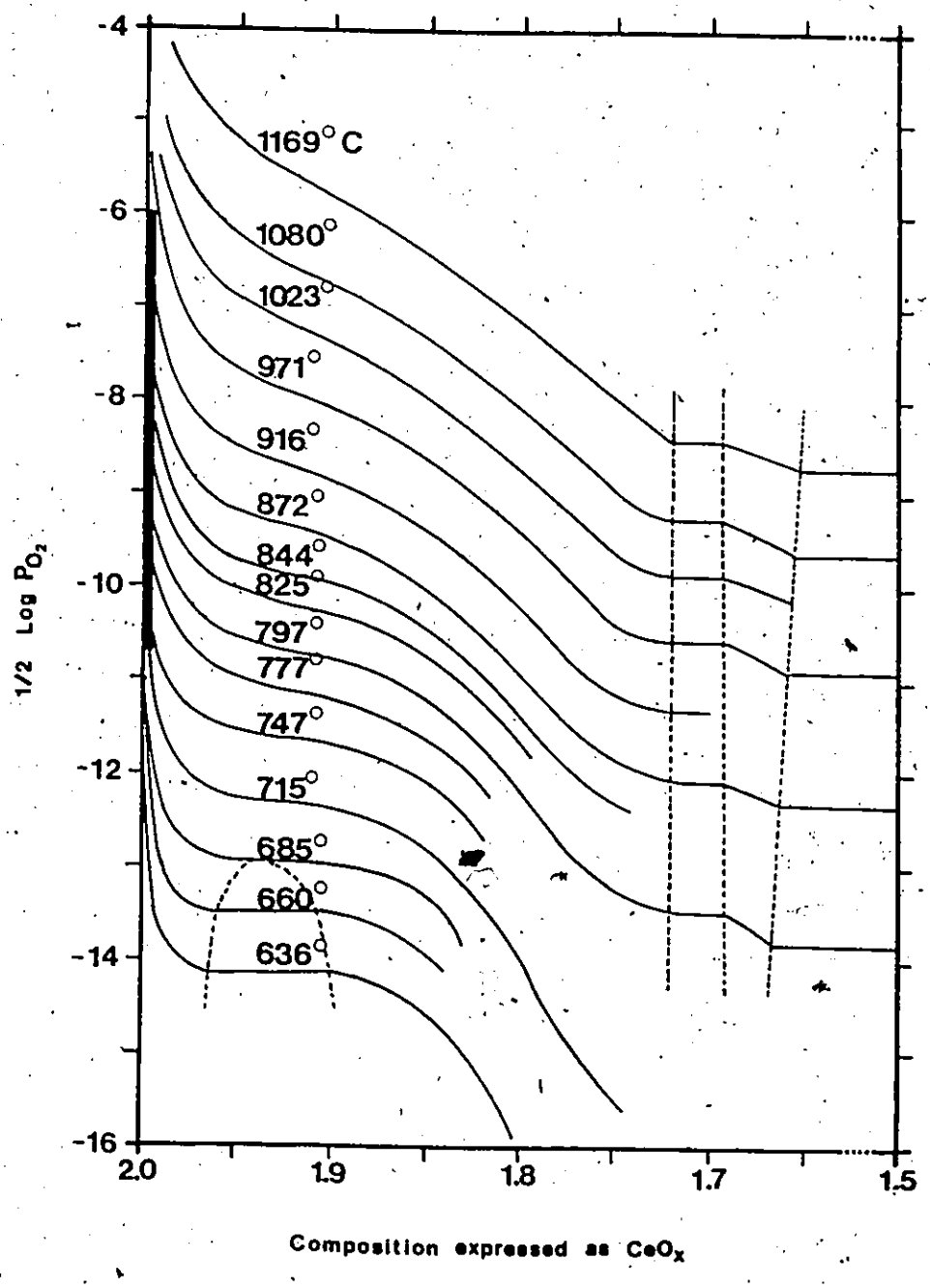

Figure A1.1 The Cerium-Oxygen Phase Diagram of Bevan and Kordis as a Function of Temperature and Oxygen Partial Pressure (41).

APPENDIX 2

Computer Calculations of High Temperature Gaseous Compositions

The F*A*C*T system (72,73) is an on-line interactive computer program that enables users to perform thermodynamic calculations by entering chemical equations and defining variables such as temperature and pressure. The data used in the calculations are automatically retrieved from a large data base. The EQUILIB program of the F*A*C*T system determines the equilibrium concentration of chemical species when specified elements or compounds partially react. The user supplies the reactants in their respective mole fractions at their initial temperature and pressure to a chemical equation. The final temperature and pressure of the unknown products are also specified. The program lists all possible compounds found in the data base and the user specifies which of these species are to be considered in the products. The program then calculates the equilibrium composition by minimizing the Gibbs free energy function for the product group. The equation cannot contain more than 6 reactant compounds nor more than 7 different elements. Reactant mole numbers should be between 0.05 and 500 to avoid losing significant figures. A sample calculation for gas A (see Table 3.7) at 1273 K is given in the computer listing on pages 137-141.

TABLE A2.1: Equilibrium Composition of Gas B at 1145 K and 101.3 kPa

Component	Mole Fraction	Component	Mole Fraction
CO	.591	HCO	$.661 \times 10^{-7}$
H_2	.289	H·	$.360 \times 10^{-7}$
CO_2	$.679 \times 10^{-1}$	SO_2	$.127 \times 10^{-8}$
H_2O	$.420 \times 10^{-1}$	SO·	$.413 \times 10^{-9}$
H_2S	$.101 \times 10^{-1}$	S	$.143 \times 10^{-9}$
COS	$.914 \times 10^{-3}$	S_3	$.554 \times 10^{-10}$
CS_2	$.159 \times 10^{-5}$	HO·	$.272 \times 10^{-10}$
S_2	$.101 \times 10^{-5}$	S_2O	$.127 \times 10^{-10}$
S	$.784 \times 10^{-6}$	S_4	$.497 \times 10^{-15}$
$(HS\cdot)_2$	$.388 \times 10^{-6}$	S_5	$.906 \times 10^{-18}$
CS	$.339 \times 10^{-6}$	O_2	$.265 \times 10^{-18}$
CH_2O	$.192 \times 10^{-6}$	SO_3	$.281 \times 10^{-18}$

```
*MCGILL - MUSIC,  SIGN ON.
/id #deffct
*PASSWORD?
******


*CODE LAST USED 12:36 31JUL81
****ALL SYSTEMS WILL BE DOWN SATURDAY AUGUST 1 FROM NOON TO 9 P.M.
*SIGN ON  FRI JUL 31, 1981  TIME=12:40\ PORT=04C  RESTART=060
*GO
fact
*IN PROGRESS

F*A*C*T SYSTEM, MONTREAL, QUEBEC, CANADA
COPYRIGHT 1979 THERMFACT LTD/LTEE
(MCGILL UNIVERSITY/ECOLE POLYTECHNIQUE)
C.W.BALE, W.T.THOMPSON, AND A.D.PELTON

****** ENTER A PROGRAM NAME OR PRESS "RETURN" TO EXAMINE F*A*C*T LIBRARY
 ******
?
*equilib

EQUILIBRIUM PRODUCT CALCULATION
*******************************

YOU DO (1) OR DO NOT (2) WISH AN EXPLANATION
?
2

****** ENTER REACTANTS ******

?
.011h2s  +  .11c*o2  +  .33h2  +  .55c*o  =
SUBSCRIPTS
?
(t,p)  (t,p)  (t,p)  (t,p)  (t,p)

SPECIFY A VALUE FOR THE PRODUCT TEMPERATURE "T"(K)
?
1273

SPECIFY A VALUE FOR THE PRODUCT PRESSURE "P"(ATM.)
?
1


POSSIBLE PRODUCT COMPOUNDS FOUND IN MAIN TABLE

  1  C*O*S                                  G1  GAS        298.0 K -  1000
.0 K
  2  H2S*O4                                 G1  GAS        298.0 K -  2000
```

.0 K						
3	S2O	G1	GAS	298.0 K -	2000	
.0 K						
4	S*O3	G1	GAS	298.0 K -	2000	
.0 K						
5	S*O2	G1	GAS	298.0 K -	1000	
.0 K						
6	S*O	G1	GAS	298.0 K -	2000	
.0 K						
7	C*S2	G1	GAS	298.0 K -	2000	
.0 K						
8	C*S	G1	GAS	298.0 K -	2000	
.0 K						
9	HZS2	G1	GAS	298.0 K -	1000	
.0 K						
10	HZS	G1	GAS	298.0 K -	1000	
.0 K						
11	S*H	G1	GAS	298.0 K -	2000	
.0 K						
12	S8	G1	GAS	298.0 K -	2000	
.0 K						
13	S7	G1	GAS	298.0 K -	2000	
.0 K						
14	S6	G1	GAS	298.0 K -	2000	
.0 K						
15	S5	G1	GAS	298.0 K -	2000	
.0 K						
16	S4	G1	GAS	298.0 K -	2000	
.0 K						
17	S3	G1	GAS	298.0 K -	2000	
.0 K						
18	S2	G1	GAS	298.0 K -	2000	
.0 K						
19	S	G1	GAS	298.0 K -	2000	
.0 K						
20	H*C*O*O*H	G1	GAS	298.0 K -	1500	
.0 K						
21	C*H3C*H2O*H	G1	GAS	298.0 K -	1500	
.0 K						
22	C2H4O	G1	GAS	298.0 K -	2000	
.0 K						
23	C*H3O*H	G1	GAS	298.0 K -	1000	
.0 K						
24	C*H2O	G1	GAS	298.0 K -	2000	
.0 K						
25	H*C*O	G1	GAS	298.0 K -	2000	
.0 K						
26	C3O2	G1	GAS	298.0 K -	2000	
.0 K						
27	C*O2	G1	GAS	298.0 K -	2500	
.0 K						
28	C*O	G1	GAS	298.0 K -	2500	
.0 K						
29	H2O2	G1	GAS	298.0 K -	1500	
.0 K						
30	H*O2	G1	GAS	298.0 K -	2000	
.0 K						
31	H2O	G1	STEAM	298.0 K -	2500	
.0 K						
32	O*H	G1	GAS	298.0 K -	2000	
.0 K						
33	O3	G1	GAS	298.0 K -	2000	
.0 K						
34	O2	G1	GAS	298.0 K -	3000	
.0 K						
35	O	G1	GAS	298.0 K -	2000	

.0 K					
36	C10H22	C1	GAS	298.0 K -	1500
.0 K					
37	C9H20	C1	GAS	298.0 K -	1500
.0 K					
38	C9H16	C1	GAS	298.0 K -	1500
.0 K					
39	C8H18	C1	GAS	298.0 K -	1500
.0 K					
40	C8H16	C1	GAS	298.0 K -	1500
.0 K					
41	C8H14	C1	GAS	298.0 K -	1500
.0 K					
42	C8H10	C1	O-XYLENE	298.0 K -	1500
.0 K					
43	C8H10	C1	GAS	298.0 K -	1500
.0 K					
44	C7H16	C1	GAS	298.0 K -	1500
.0 K					
45	C7H14	C1	GAS	298.0 K -	1500
.0 K					
46	C7H8	C1	GAS	298.0 K -	1500
.0 K					
47	C6H14	C1	GAS	298.0 K -	1500
.0 K					
48	C6H12	C1	GAS	298.0 K -	1500
.0 K					
49	C6H6	C1	GAS	298.0 K -	1500
.0 K					
50	C5H8	C1	GAS	298.0 K -	1500
.0 K					
51	C4H10	C1	GAS	298.0 K -	1500
.0 K					
52	C4H8	C1	GAS	298.0 K -	1500
.0 K					
53	C4H6	C1	GAS	298.0 K -	1500
.0 K					
54	C3H6	C1	GAS	298.0 K -	1000
.0 K					
55	C3H4	C1	GAS	298.0 K -	1500
.0 K					
56	C2H4	C1	GAS	298.0 K -	1200
.0 K					
57	C2H2	C1	GAS	298.0 K -	2000
.0 K					
58	C2H	C1	GAS	298.0 K -	2000
.0 K					
59	C*H4	C1	GAS	298.0 K -	2000
.0 K					
60	C*H3	C1	GAS	298.0 K -	2000
.0 K					
61	C*H2	C1	GAS	298.0 K -	2000
.0 K					
62	C*H	C1	GAS	298.0 K -	2000
.0 K					
63	C5	C1	GAS	298.0 K -	2000
.0 K					
64	C4	C1	GAS	298.0 K -	2000
.0 K					
65	C3	C1	GAS	298.0 K -	2000
.0 K					
66	C2	C1	GAS	298.0 K -	4000
.0 K					
67	C	C1	GAS	298.0 K -	2000
.0 K					
68	H2	C1	GAS	298.0 K -	3000

```
.0 K
 69  H                              G1  GAS          298.0 K -  6000
.0 K

 70  H2S*O4                         L1  LIQUID       298.0 K -   553
.0 K
 71  H2C*S3                         L1  LIQUID       298.0 K -   331
.0 K
 72  C*S2                           L1  LIQUID       298.0 K -   319
.0 K
 73  S                              L1  LIQUID       440.0 K -   718
.0 K
 74  H*C*O*O*H                      L1  LIQUID       298.0 K -   374
.0 K
 75  C*H3C*H2O*H                    L1  LIQUID       298.0 K -   352
.0 K
 76  C*H3O*H                        L1  LIQUID       298.0 K -   338
.0 K
 77  H2O2                           L1  LIQUID       298.0 K -   431
.0 K
 78  H2O                            L1  WATER        298.0 K -   374
.0 K
 79  C10H22                         L1  LIQUID       298.0 K -   448
.0 K
 80  C9H20                          L1  LIQUID       298.0 K -   424
.0 K
 81  C8H18                          L1  LIQUID       298.0 K -   399
.0 K
 82  C8H16                          L1  LIQUID       298.0 K -   405
.0 K
 83  C8H10                          L1  O-XYLENE     298.0 K -   418
.0 K
 84  C8H10                          L2  ETHYLBENZ.   298.0 K -   409
.0 K
 85  C7H16                          L1  LIQUID       298.0 K -   372
.0 K
 86  C7H14                          L1  LIQUID       298.0 K -   374
.0 K
 87  C7H8                           L1  LIQUID       298.0 K -   384
.0 K
 88  C6H14                          L1  LIQUID       298.0 K -   342
.0 K
 89  C6H12                          L1  LIQUID       298.0 K -   345
.0 K
 90  C6H6                           L1  LIQUID       298.0 K -   353
.0 K

 91  S                              S1  RHOMBIC      298.0 K -   368
.0 K
 92  S                              S2  MONOCLINIC   368.0 K -   388
.0 K
 93  C                              S1  GRAPHITE    1100.0 K -  4673
.0 K
 94  C                              S2  DIAMOND      298.0 K -  1200
.0 K

ENTER CODE NUMBERS OF SPECIES TO BE CONSIDERED (GASES FIRST)
?
27,28,31,5,18,1,68,10,6,3,17,11,9,7,19,69,8,32,16,4,25,15,24,20,34

PRESS "RETURN" WHEN READY FOR OUTPUT
?
+
```

```
COMPUTATION TIME LIMIT WILL BE 32 SERVICE UNITS

XXXXXXXXXXXXXXXXXXXXXXXXXXXXXXXXXXXXXXXXXXXXXXXXXXXXXXXXXXXXXXXX
XXXXXXXX

.011H2S  +  .11C*O2  +  .33H2   +  .55C*O  =
(T,P)  (T,P)  (T,P)  (T,P)

                    1.001  (     .599       C*O
                           +     .280       H2
                           +     .597E-01   C*O2
                           +     .502E-01   H2O
                           +     .100E-01   H2S
                           +     .931E-03   C*O*S
                           +     .724E-05   S2
                           +     .481E-05   S*H
                           +     .202E-05   C*S2
                           +     .101E-05   C*S
                           +     .796E-06   H2S2
                           +     .375E-06   H
                           +     .180E-06   H*C*O
                           +     .165E-06   C*H2O
                           +     .218E-07   S*O2
                           +     .103E-07   S*O
                           +     .389E-08   S
                           +     .689E-09   O*H
                           +     .669E-09   S3
                           +     .279E-09   H*C*O*O*H
                           +     .263E-09   S2O
                           +     .138E-13   S4
                           +     .772E-16   O2
                           +     .297E-16   S*O3
                           +     .154E-16   S5                   )
                                            (1273.0, 1.00    ,G )

        CALCULATIONS ARE BASED ON THE INDICATED NUMBER OF GRAM MOLES

****************************************************************
*******
   (T)      (P)        DELTA H     DELTA G     DELTA V     DELTA S    DE
LTA U
   (K)      (ATM)       (CAL)       (CAL)        (L)       (CAL/K)    (
CAL)
****************************************************************
*******

        SPECIFY  2 PROPERTIES


/depart

XXXXXXXXXXXXXXXXXXXXXXXXXXXXXXXXXXXXXXXXXXXXXXXXXXXXXXXXXXXXXXXX
XXXXXXX
```

APPENDIX 3.

Calibration of the FPD Gas Chromatograph

Procedure:

(1) Detector conditions were adjusted as closely as possible to the recommended values (H_2 50 mL/min, O_2 10 mL/min, air 50 mL/min) and the g.c. was allowed to stabilize at the conditions shown in Figure A3.1. The temperature program mode was used to over-ride the slope compensation program for isothermal runs within the peak processing unit. Otherwise, the integrator failed to process sharp peaks after a ten minute interval.

(2) Valve V-4 (see Figure 5.3) directed the EDF effluent to the gas sampling valve V-5. The nitrogen diluent velocity through the EDF was adjusted to about 100 mL/min.

(3) The sample loop to be calibrated was installed.

(4) The automatic gas sampling valve was programmed to inject EDF effluent at 2.0 minute intervals.

(5) 50 ± 1 µL of C.P. grade H_2S was injected from a 100 µL gas tight syringe into the EDF while simultaneously initiating the chart recorder/peak processor. A magnetic stirrer ensured that EDF contents were mixed effectively.

(6) Calibration runs were repeated using 60 and 70 µL injections. Other experiments varied detector conditions, diluent flow rates, injection times and frequency, and sample loop sizes.

Sample Calculations

Runs - 1, 2, 3

Detector Conditions	H_2 47 mL/min
	O_2 10 mL/min
	Air 45 mL/min
	He 29 mL/min
Sample loop size	0.5 mL
Diluent velocity	105 mL/min
Injection size	50, 60, 70 µL

Run - 4

Detector Conditions	H_2 50 mL/min
	O_2 10 mL/min
	Air 45 mL/min
	He 29 mL/min
Sample loop size	0.5 mL
Diluent velocity	99.0 mL/min
Injection size	50 µL

The initial concentrations, C_i, were calculated using equation 5.3.2. Concentrations of the EDF effluent at times after the initial injection are given by equation 5.3.1.

Example: For a 50 µL injection

$$C_i = \frac{32{,}000}{24.5}\left(\frac{50\ \mu L\ \text{injected}}{215}\right) = 304\ \text{ng S/mL}$$

$$C_{t=1} = (304)\exp[-105(1.0)/215] = 187\ \text{ng S/mL}$$

Table A3.1

Data for Calibration Curve (Concentrations in ng S/mL)

Time (min)	Run 1 $C_i = 304$		Run 2 $C_i = 365$	
	C	Response	C	Response
1.0	187	635,100	223	699,000
3.0	71	358,300	85	412,200
5.0	26	142,200	31	177,000
7.0	10	30,640	11	43,950
9.0	3.8	4,167	4.4	6,596
11.0	1.4	267	1.7	517

Time (min)	Run 3 $C_i = 425$		Run 4 $C_i = 304$	
	C	Response	C	Response
1.0	261	745,200	191	628,600
3.0	98	465,400	75	353,400
5.0	37	211,900	30	164,700
7.0	14	59,860	12	55,410
9.0	5.2	9,714	4.6	14,620
11.0	2.0	1,167	1.8	3,710

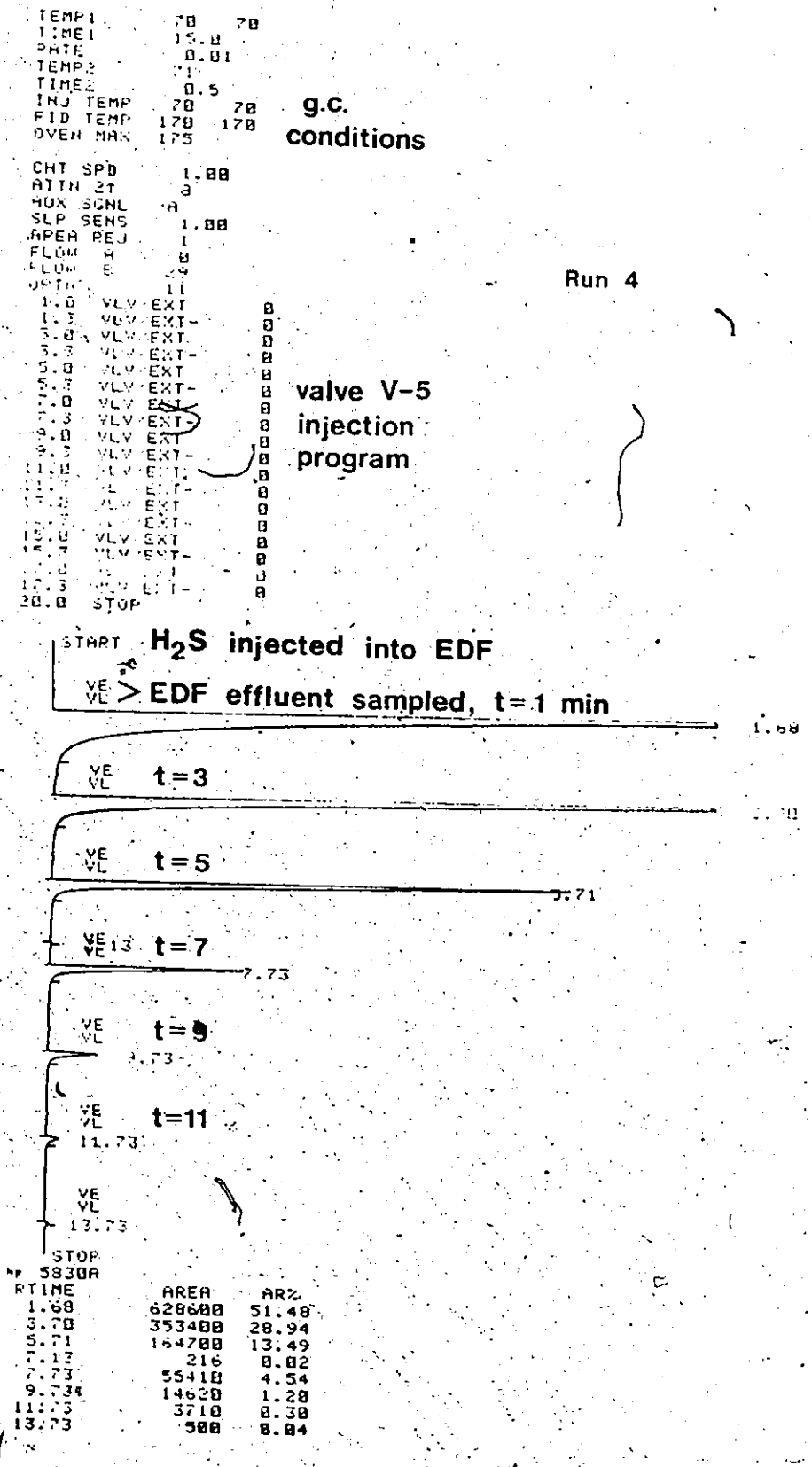

Figure A3.1: Trace from a Calibration Run

APPENDIX 4

Analysis of Bastnaesite Concentrates

Powder X-ray diffraction patterns were obtained on a Philips X-ray diffractometer equipped with a copper K α_1 lamp (λ = 1.54050 Å). Powdered bastnaesite samples (as-received from Molycorp Inc.) were mixed with acetone and a small amount styrene binder using a mortar and pestle. A thin layer of this mixture was mounted on a microscope slide and allowed to dry overnight. X-ray diffraction patterns are listed in Tables A4.1 and A4.2.

Table A4.1

X-ray Diffraction Patterns of Bastnaesite Concentrates 4000 and 4010

		Bastnaesite 4000		Bastnaesite 4010	
d (lit)	I (lit)(84)	d (obs)	I (obs)	d (obs)	I (obs)
				4.95	41
4.881	42	4.88	31	4.87	57
3.56	71	3.58	>100	3.57	100
		3.50	27		
		3.41	17		
		3.30	11	3.32	10
		3.21	12	3.21	10
		3.10	8		
major $CaCO_3$ line		3.02	19		
		2.90	>100	2.90	84
2.879	100	2.87	69	2.88	91
		2.82	8		
		2.78	8		
2.610	1				
		2.53	8		
2.445	9	2.45	20	2.45	16
2.273	3	2.28	7	2.27	9
2.238	3				
2.057	42	2.07	35	2.07	41
		2.05	30	2.06	64
2.016	42	2.03	41	2.03	40
		1.96	12		
1.898	42	1.91	32	1.91	55
		1.89	25	shoulder	
1.783	9	1.80	18	1.80	17
		1.78	11		
		1.69	19	1.68	17
1.674	21	1.67	13	1.67	17
1.629	1				
1.573	15	1.58	11	1.58	17
		1.54	7		
1.481	9	1.48	5	1.48	9
1.439	11	1.45	5	1.45	12
1.347	7	1.35	6	1.35	9
1.298	15	1.31	14	1.31	17
		1.30	10	shoulder	
1.277	7				
1.223	2	1.21	4	1.21	7
1.204	6	1.20	4	1.20	7
1.180	9	1.19	9	1.19	12
1.156	11	1.16	7	1.16	7

Table A4.2

X-ray Diffraction Patterns of Bastnaesite Concentrates 4000 C, 4100, Sintered 4100

		Bastnaesite		Bastnaesite		Bastnaesite 4100	
EuOF	(800°C)	4000 C		4100		Sintered at 1300°C	
d^{lit}	$I/I_o{}^{lit}$	d	I/I_o	d	I/I_o	d	I/I_o
		3.49	29				
		3.39	17				
		3.26	26				
3.19	100	3.18	100	3.21	100	3.20	100
		3.14	49				
$CaCO_3$		3.01	17				
				2.88	9	2.86	6
2.77	30	2.76	26	2.77	27	2.76	36
		2.43	14				
		2.03	9				
1.956	50	1.96	46	1.97	44	1.96	74
		1.93	31				
1.668	35	1.66	29	1.68	27	1.67	57
		1.64	14				
1.597	5			1.60	5	1.60	13
1.383	7					1.38	11
1.269	10			1.28	7	1.27	19
1.237	7					1.24	13
1.119	14					1.13	17
						1.07	15

Table A4.3: Elemental Analysis of Bastnaesite Concentrates –% by weight

Component	Concentrate				Error	Present in Ore as uncalcined/calcined
	Uncalcined		calcined			
	4000	4010	4000C	4100		
Ce	28.10	32.30	31.00	38.70	±1.0	$RE(OH)_{1-x}F_xCO_3/CeO_2$
La	16.30	18.70	18.00	23.80	±0.5	$RE(OH)_{1-x}F_xCO_3/REOF$
Nd	6.30	7.30	7.10	8.10		$RE(OH)_{1-x}F_xCO_3/REOF$
Pr	2.30	2.65	2.55	3.00		$RE(OH)_{1-x}F_xCO_3/REOF$
Sm	0.30	0.35	0.34	0.38		$RE(OH)_{1-x}F_xCO_3/REOF$
Gd	0.14	0.16	0.14	0.19		$RE(OH)_{1-x}F_xCO_3/REOF$
Other	0.05	0.056	0.054	0.060		$RE(OH)_{1-x}F_xCO_3/REOF$
Total RE	53.49	61.52	59.18	74.23		
F	4.15	4.60	4.10	5.00	±0.25	$RE(OH)_{1-x}F_xCO_3/REOF$
CO_2	19.51	20.70	8.48	4.05		$RE(OH)_{1-x}F_xCO_3/CaCO_3$ + residual RE carbonates
Sr	5.70	1.10	7.10	1.20		strontianite
Ca	4.25	0.71	6.70	0.64		calcite
Ba	1.12	0.78	1.03	1.20		barite
Fe	0.43	0.39	0.47	0.39		
Al	0.10	0.08	0.11	0.08		
Mg	0.29	0.17	0.33	0.18		acmite
Na	0.022	0.016	0.025	0.023		
K	0.025	0.027	0.030	0.018		
P	0.46	0.34	0.43	0.56		
Balance (mainly oxygen)	10.45	9.57	12.02	12.43		

The analyses were carried out using DC Argon Plasma Emission Spectroscopy (except F and CO_2) by Globe Metallurgical Laboratories, Ohio, U.S.A. Systems used were the SpectroSpan IV and IIIB (SpectraMetrics, Inc.). The sample preparation involved an acid decomposition procedure developed by Globe Metallurgical. Standards were prepared by combining the pure oxides, in proportions similar to the composition of the sample. Further details of the technique and sample preparation are given in reference 101. The CO_2 content was determined by weight loss upon ignition at 900°C. The fluorine content was determined by a carbonate fusion method (Barringer Magenta Ltd., Rexdale, Ont.).

Table A4.4: Compositional Analysis of Bastnaesite Concentrates

Element	Moles of Element in 100 g				Error
	4000	4010	4000C	4100	
Ce	0.2005	0.2305	0.2212	0.2762	±0.006
La	0.1173	0.1346	0.1296	0.1713	±0.004
Total RE	0.3811	0.4382	0.4216	0.4729	
F	0.2184	0.2421	0.2158	0.2632	±0.013
CO_2	0.4434	0.4705	0.1927	0.0921	
Ca	0.1060	0.0177	0.1672	0.0160	
	Molar Ratios				
F/RE[1]	0.573	0.552	0.512	0.556	
CO_2/(RE + Ca)[2]	0.91	1.03	N/A	N/A	
CO_2/Ca[3]	N/A	N/A	1.15	5.76	
F/(RE-Ce)[4]	1.21	1.17	1.08	1.34	

(1) This gives the value of x in $RE(OH)_{1-x} F_x CO_3$

(2) The carbonate content of uncalcined concentrates is present as $RE(OH)_{1-x} F_x CO_3$ and $CaCO_3$. A theoretical value of 1 should be obtained.

(3) In calcined concentrates the carbonates are mainly present as calcite (since process temperatures used by manufacturer are too low to decompose this mineral). A theoretical value of 1 should be obtained. Larger values indicate the presence of residual rare earth carbonates.

(4) This ratio would be equal to 1.0 if the fluorine was associated with rare earth elements other than cerium. A value greater than one suggests that at least part of the cerium is associated with the fluoride.

Theoretical Weight Losses of Bastnaesite Concentrates by TGA.

From Table 6.2, the typical reactions are:

$$REFCO_3(s) = REOF(s) + CO_2(g) \qquad < 600°C$$

$$RE(OH)CO_3(s) = \tfrac{1}{2} RE_2O_2CO_3(s) + \tfrac{1}{2} CO_2(g) + \tfrac{1}{2} H_2O(g) \qquad < 600°C$$

$$\tfrac{1}{2} RE_2O_2CO_3(s) = \tfrac{1}{2} RE_2O_3(s) + \tfrac{1}{2} CO_2(g) \qquad > 600°C$$

For each mole of $REFCO_3$, one mole of CO_2 is lost. For each mole of $RE(OH)CO_3$, $\frac{1}{2}$ mole of CO_2 and $\frac{1}{2}$ mole of H_2O is lost below 600°C, and a further $\frac{1}{2}$ mole of CO_2 is lost above 600°C.

Sample calculation for concentrate 4000 (basis 100 g).

$$\left(\begin{matrix}\text{Weight loss} \\ < 600°C\end{matrix}\right) = (\text{moles } RE(OH)CO_3)[(\tfrac{1}{2})(MW\ CO_2) + \tfrac{1}{2}(MW\ H_2O)]$$
$$+ (\text{moles } REFCO_3)[(1)(MW\ CO_2)]$$
$$= (1 - 0.573)(0.3811)[\tfrac{1}{2}(44) + \tfrac{1}{2}(17)] + (0.573)(0.3811)(1)(44)$$
$$= 14.57 \text{ g/100 g bastnaesite}$$

$$\left(\begin{matrix}\text{Weight loss} \\ > 600°C\end{matrix}\right) = (\text{moles } RE(OH)CO_3)(\tfrac{1}{2})(MW\ CO_2)$$
$$= (1 - 0.573)(0.3811)(\tfrac{1}{2})(44)$$
$$= 3.58 \text{ g/100 g.}$$

Weight loss contribution from calcite $= (\text{moles Ca})(1)(MW\ CO_2)$

$$= (0.1060)(1)(44)$$
$$= 4.66 \text{ g/100 g.}$$

APPENDIX 5

Phase Relationships of Non-Stoichiometric Cerium Oxide (40)

The non-stoichiometric cerium oxides, CeO_{2-x}, are oxygen-deficient oxides involving single-charged vacancies near the stoichiometric compositions. According to defect theories, the mass action law can be used to express the concentration of defects in terms of temperature and partial pressure of oxygen, if the defects are randomly distributed and non-interacting. These conditions are normally satisfied near stoichimetry, but the mass action law is sometimes extended to slightly greater concentrations. Thus, the deviation from stoichiometric composition, x in CeO_{2-x}, has an oxygen partial pressure dependence of $x \propto p_{O_2}^{-1/s}$, where s depends on the type of predominant defects present in the oxides and the partial free energy is given by:

$$\Delta G_{O_2} = RT \ell n\, p_{O_2} \propto -s\, RT \ell n\, x \qquad \text{A5.1}$$

Equation A5.1 shows that a linear relationship is obtained when $RT \ell n\, p_{O_2}$ is plotted against $\ell n\, x$ at constant temperature if s is constant.

Considering the phase rule criteria for a binary oxide system in equilibrium with a gas phase, the plot gives information about the phase relationships of the system. For example, a horizontal line is observed for a two phase range, since the system will have only one degree of freedom. Vertical lines prove the existence of discrete compounds of a narrow composition range. Lines of intermediate slopes indicate the existence of non-stoichiometric phases or continuous sequences of ordered or partly ordered phases.

APPENDIX 6

Prediction of Maximum Conversion using the Single-Pore Model

Whenever the solid product of reaction has a larger molar volume (ie. smaller density) than the solid reactant, the reaction will eventually terminate owing to pore closure by the solid product. According to the pore model of Ramachandran and Smith (77), the maximum conversion is predicted by the equations

$$(\bar{\eta})_{max} = 1 - \frac{1 - \varepsilon_o \frac{\gamma}{\gamma - 1}}{1 - \varepsilon_o} \qquad \text{A6.1}$$

$$\gamma = \frac{d\,\rho_B\,M_D}{b\,\rho_D\,M_B\,(1-\varepsilon_D)} = \text{ratio of molar volume of product to that of reactant} \qquad \text{A6.2}$$

$$\varepsilon_D \simeq \frac{\varepsilon_f - \varepsilon_o}{1 - \varepsilon_o} \qquad \text{A6.3}$$

where ε_o = initial porosity

b = stoichiometric coefficient of reactant solid

d = stoichiometric coefficient of product solid

ρ_B = density of reactant (g/cm^3)

ρ_D = density of solid product (g/cm^3)

M_B = molecular weight of solid reactant

M_D = molecular weight of solid product

ε_D = porosity of product layer

ε_f = porosity of the completely reacted solid

Two important points must be noted:

(1) The above equation assumes no diffusional resistance in the pore. When concentration gradients exist in the pores the above equation overestimates the maximum conversion for a given initial porosity.

(2) When $\varepsilon_o > (\gamma - 1)/\gamma$, complete conversion is ensured provided there are no concentration gradients in the pore. When concentration gradients exist, a larger porosity is required for complete conversion. For the desulfurization reaction:

$$2\,CeO_{2-x}(s) + H_2S(g) + (1-2x)\,H_2(g) = Ce_2O_2S(s) + 2(1-x)\,H_2O(g) \qquad 3.3.5$$

the following data are substituted into equations A6.1-6.3.

$b = 2$

$d = 1$

$\rho_B \simeq 7.2\ g/cm^3$ for CeO_2

$\rho_D = 5.99\ g/cm^3$

$M_B = 170.3\ g/mol$ (for $CeO_{1.885}$)

$M_D = 344.3\ g/mol$

Assume the product layer has no porosity ie $\varepsilon_D = 0$. Thus,

$$\gamma = \frac{(1)(7.2)(344.3)}{(2)(5.99)(170.3)(1-0)} = 1.22$$

(γ values greater than 1 are indicative of a reduction in porosity upon reaction).

If diffusional resistance is negligible, complete conversion of the solid will occur if the porosity is greater than:

$$\varepsilon_o > \frac{(\gamma-1)}{\gamma} = \frac{1.22-1}{1.22} = 0.18$$

For a pellet of porosity 11.4%, the theoretical maximum conversion would be

$$(\bar{\eta})_{max} = 1 - \frac{1-(0.114)(1.22/0.22)}{1-0.114} = 0.58$$

If the experimentally measured value of the maximum conversion is significantly less than 58%, diffusional resistance in the pore is important.

APPENDIX 7

Reduction Data for Bastnaesite 4100

Analysis of TGA Weight Loss Peaks of Bastnaesite 4100 in Carbon Monoxide

Total weight of sample	128.1 mg
Weight loss 200 - 600°C	2.0 mg
Weight loss 600 - 900°C	3.0 mg

% weight loss from decomposition of fluorocarbonate = 1.60%

% weight loss from reduction = 2.35%

Table A7.1: Predicted weight losses for full and partial reduction of CeO_2.

Reaction	% wt loss
$2\,CeO_2 + CO = Ce_2O_3 + CO_2$	4.6
$CeO_2 + 0.18CO = CeO_{1.82} + 0.18\,CO_2$	1.7

Expected weight loss if entire cerium (+4) content of bastnaesite 4100 is reduced to the cerium (+3) form.

No. of moles of Ce per 100 g of bastnaesite 4100 = 0.2762 ± 0.006 moles (see Table A4.4, Appendix 4)

Molecular weight of CeO_2 = 172.12 g/mol

$$\% \text{ Weight loss} = \left(\frac{4.6\text{g lost}}{100\text{g } CeO_2}\right)\left(\frac{172.12\text{g } CeO_2}{\text{mole } CeO_2}\right)\left(\frac{0.2762 \text{ moles Ce}}{100\text{g Bastnaesite}}\right)(100)$$

$$= 2.19 \pm 0.05\%$$

Enthalpies of Reaction

Table A7.2: Heats of formation calculated at 1000K (64)

Compound	$\Delta H°_f$(kcal/mol)	$\Delta H°_f$(kJ/mol)
CeO_2(s)	-259.619 ± 0.5	-1086.25
$CeO_{1.82}$(s)	-246.113 ± 1.0	-1029.74
Ce_2O_3(s)	-433.608 ± 1.0	-1814.22
CO_2(g)	-94.355 ± 0.03	-394.78
CO(g)	-26.754 ± 0.05	-111.094

$CeO_2(s) + 0.18\,CO(g) = CeO_{1.82}(s) + 0.18\,CO_2(g)$ $\Delta H° = 1.3 \pm 1.5$ kcal

$= 5.44 \pm 6.28$ kJ

$CeO_2(s) + 1/2\,CO(g) = 1/2\,Ce_2O_3(s) + 1/2\,CO_2(g)$ $\Delta H° = 9.01 \pm 1.5$ kcal

$= 37.7 \pm 6.3$ kJ

APPENDIX 8

Determination of Equilibrium Constants for the Hydrolysis Reaction

Table A8.1: Thermodynamic Data required for Hydrolysis Reaction Calculations

Reaction	Standard Free Energy Equation (cal/mol)
$1/2\ H_2(g) + 1/2\ F_2(g) = HF$	$\Delta G_f^\circ = -65247.0 - 0.920T$
$Ce(\ell) + O_2(g) = CeO_2(s)$	$\Delta G_f^\circ = -260581 + 49.82T$
$2La(s) + 3/2\ O_2(g) = La_2O_3(s)$	$(<1134°C)\ \Delta G°_{1100} = -422547 + 64.95T$ $(>1193°C)\ \Delta G°_{1200} = -429665 + 68.59T$
$H_2(g) + 1/2\ O_2(g) = H_2O(g)$	$\Delta G_f^\circ = -59543 + 12.93T$
$La(s) + 1/2\ O_2(g) + 1/2\ F_2(g) = LaOF(s)$	$\Delta G_f^\circ = -292239 + 43.76T$
$Ce(\ell) + 1/2\ O_2(g) + 1/2\ F_2(g) = CeOF(s)$	$\Delta G_f^\circ = -281858 + 35.38T$

Hydrolysis of LaOF (T < 1134 K)

$$2LaOF(s) + H_2O(g) = La_2O_3(s) + 2HF(g)$$

$$\Delta G° = \Delta G_f^\circ(La_2O_3) + 2\Delta G_f^\circ(HF) - 2\Delta G_f^\circ(LaOF) - \Delta G_f^\circ(H_2O)$$

$$= 90980 - 37.34T \text{ cal}$$

$$= 380569 - 156.2\ T\ J$$

At 1100 K $\Delta G° = 49906$ cal

$$K = (p_{HF})^2/(p_{H_2O}) = \exp(-\Delta G°/RT) = 1.23\times10^{-10}$$

If $p_{H_2O} = 1$ atm $\quad p_{HF} = 1.11\times10^{-5}$

If $p_{H_2O} = 0.04$ atm $\quad p_{HF} = 2.22\times10^{-6}$

The equilibrium constant indicates that LaOF is very stable in moist atmospheres.

Hydrolysis of CeOF, T > 1077 K

$$2CeOF(s) + H_2O(g) + 1/2\,O_2(g) = 2CeO_2(s) + 2HF(g)$$

$$\Delta G^\circ = 2\Delta G^\circ(CeO_2) + 2\,\Delta G^\circ(HF) - 2\Delta G^\circ(CeOF) - \Delta G^\circ(H_2O) - 1/2\Delta G^\circ(O_2)$$

$$= -28397 + 14.82\,T \text{ cal}$$

$$= -118785 + 61.99\,T \text{ J}$$

At 1100 K, $\Delta G^\circ = -12095$ cal

$$K = (p_{HF})^2/((p_{H_2O})(p_{O_2})^{1/2}) = \exp(-\Delta G^\circ/RT) = 2.52 \times 10^2$$

The large equilibrium constant indicates that CeOF would readily decompose in air at high temperatures. (eg. $p_{O_2} = .21$, $p_{H_2O} = 0.002 \Rightarrow p_{HF} = 2.31$) However, in a typical coal gas of composition 71% CO, 23% H_2, 4.7% CO_2, 1.5% H_2O, $p_{O_2} = 10^{-20}$ at 1100 K:

$$p_{HF} = [2.52 \times 10^2\,(0.015)\,(10^{-20})^{1/2}]^{1/2}$$

$$= 1.9 \times 10^{-5}$$

Thus, CeOF could exist under desulfurization conditions.

(Partial pressures are given in atmospheres).

APPENDIX 9

Analysis of Kinetic Data for the Pyrohydrolysis of Bastnaesite 4100

The chemical reaction can be represented as

$$2\,REOF(s) + H_2O(g) = RE_2O_3(s) + 2HF(g)$$

If the rate of reaction can be expressed as a first-order reaction, the rate per unit weight of solid, r, is given by:

$$r = -\frac{1}{2} r_{REOF} = -r_{H_2O} = r_{RE_2O_3} = \frac{1}{2} r_{HF} = k\, C_{H_2O} \qquad A9.1$$

The initial slopes of the pyrohydrolysis curves are therefore related to the rate of reaction by:

$$\frac{1}{2} r_{HF} = \frac{1}{2}\left(\frac{\Delta C_{HF}}{\Delta t}\right)_{t\to 0} = k\, C_{H_2O} \qquad A9.2$$

Thus, the rate constant is given by:

$$k = \frac{1}{2}\left(\frac{\Delta C_{HF}}{\Delta t}\right)_{t\to 0} / C_{H_2O} \qquad A9.3$$

where C_{H_2O} can be calculated using the ideal gas law.

Table A9.1: Pyrohydrolysis Kinetic Calculations

T (°C)	1/T (K^{-1})	$(\Delta C_{HF}/\Delta t)_{t\to 0}$	C_{H_2O} (mol/K)	k	$\ell n\ k$
704	1.24×10^{-3}	7.14×10^{-2}	1.25×10^{-2}	2.86	1.05
752	9.75×10^{-4}	2.00×10^{-1}	1.19×10^{-2}	8.42	2.13
868	8.76×10^{-4}	4.00×10^{-1}	1.07×10^{-2}	18.7	2.93
880	8.67×10^{-4}	1.00	1.06×10^{-2}	47.3	3.86

According to the Arrhenius equation:

$$k = k_o \exp(-E_a/RT)$$

Thus, a plot of $\ell n\ k$ versus 1/T gives a slope of $(-E_a/R)$.

From Figure 6.9,

$$\text{slope} = (-E_a/R) = -1.46\times10^{+4}\ K^{-1}$$

$$\therefore \quad E_a = (1.46\times10^{+4}\ K^{-1})(8.314\times10^{-3}\ kJ\cdot K^{-1}\cdot mol^{-1})$$

$$= 121.2\ kJ\cdot mol^{-1}$$

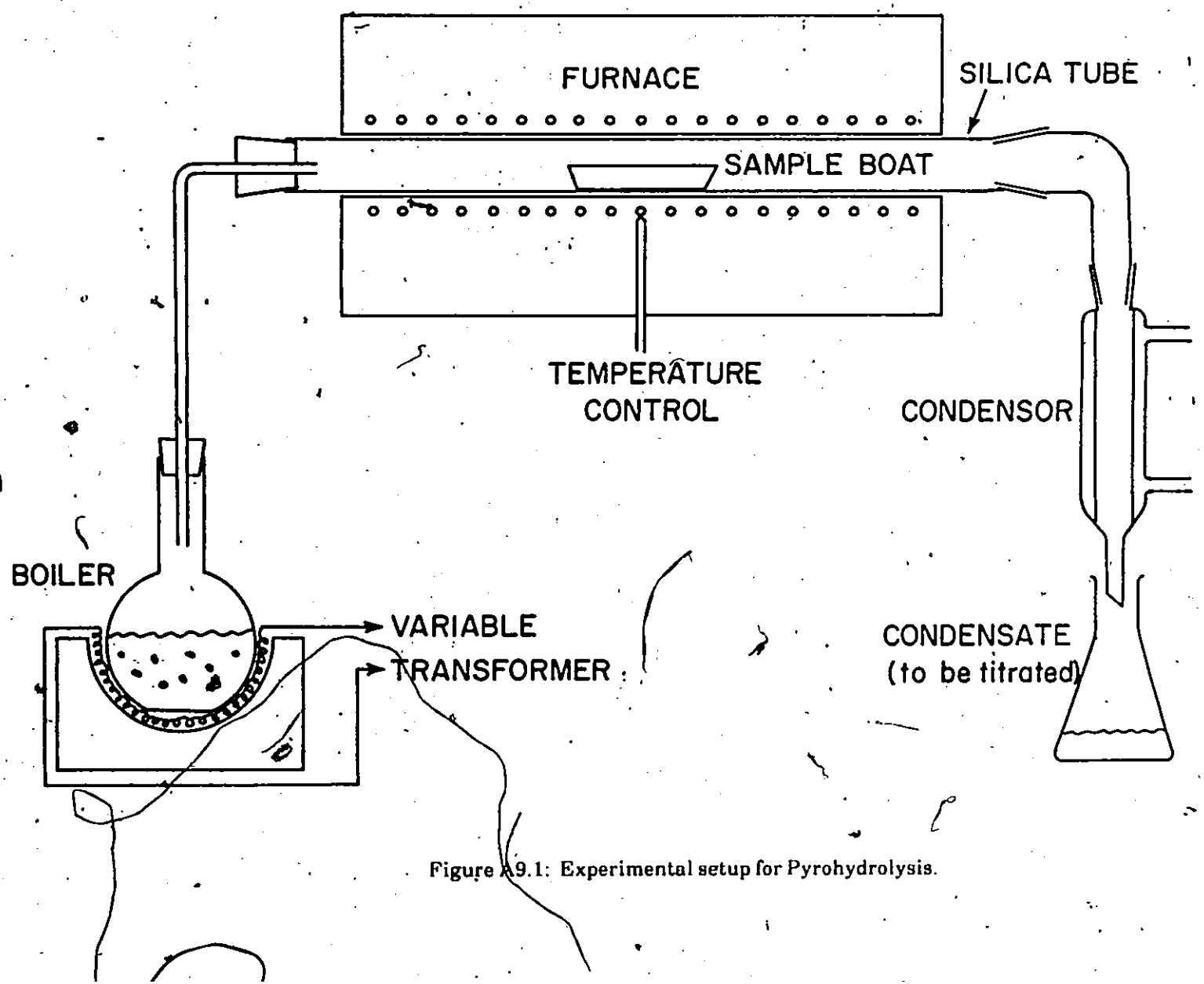

Figure A9.1: Experimental setup for Pyrohydrolysis.

APPENDIX 10

Traces for Desulfurization, Regeneration and Reduction Cycles

Data for Desulfurization Run Illustrated in Figure 6.10.

Unsupported Sorbent		
Particle Size	–0.841/+0.297 mm	(–20/+50 mesh)
Sintering Temperature	1400°C	
Porosity of Sorbent	11.4%	
Weight of Bed (CeO_2)	17.94 g	
Height of Bed	8.2 cm	
Temperature	871°C, 1144 K	
Reduction Time (5% H_2/95% N_2)	19 h 40 min	
Simulated Gas Composition	1.2% H_2S, 10.8% CO_2, 33.0% H_2, 55.0% CO	
Flow Rate	27 mL/min	

Inlet Gas Composition Calculated by F*A*C*T

Species	Mole Fraction
CO	0.591
H_2	0.289
CO_2	0.0679
H_2O	0.0420
H_2S	0.0101

$-\log p_{S_2} = 6.00$

$-\log p_{O_2} = 18.6$

Predicted Solid Reactant, using Figure A1.1 is $CeO_{1.935}$

Typical Desulfurization
G.C. Trace

Desulfurization Experiment

029

FEB 18 1982

```
TEMP1       50    50
TIME1       60.0
RATE         0.01
TEMP2       71
TIME2        0.2
INJ TEMP    50    50
FID TEMP   175   175
OVEN MAX   180

CHT SPD      1.00
ATTN 2↑     10
AUX SGNL    A
SLP SENS     0.10
AREA REJ     1
FLOW  A      0
FLOW  B     24
OPTN        11
  0.1  ZERO
  0.5  VLV/EXT        0
  0.8  VLV/EXT-       0
  5.0  VLV/EXT        0
  5.3  VLV/EXT-       0
  7.5  VLV/EXT        0
  7.8  VLV/EXT-       0
 10.0  VLV/EXT        0
 10.3  VLV/EXT-       0
 12.0  VLV/EXT        0
 12.3  VLV/EXT-       0
 14.0  VLV/EXT        0
 14.3  VLV/EXT-       0
 16.0  VLV/EXT        0
 16.3  VLV/EXT-       0
 18.0  VLV/EXT        0
 18.3  VLV/EXT-       0
 20.0  VLV/EXT        0
 20.3  VLV/EXT-       0
 22.0  VLV/EXT        0
 22.3  VLV/EXT-       0
 24.0  VLV/EXT        0
 24.3  VLV/EXT-       0
 26.0  VLV/EXT        0
 26.3  VLV/EXT-       0
 28.0  VLV/EXT        0
 28.3  VLV/EXT-       0
 30.0  STOP
```

g.c. and integrator settings

valve V-5 injection program

Detector Conditions (mL/min)

H_2	50
O_2	10.5
Air	53

baseline adjustment

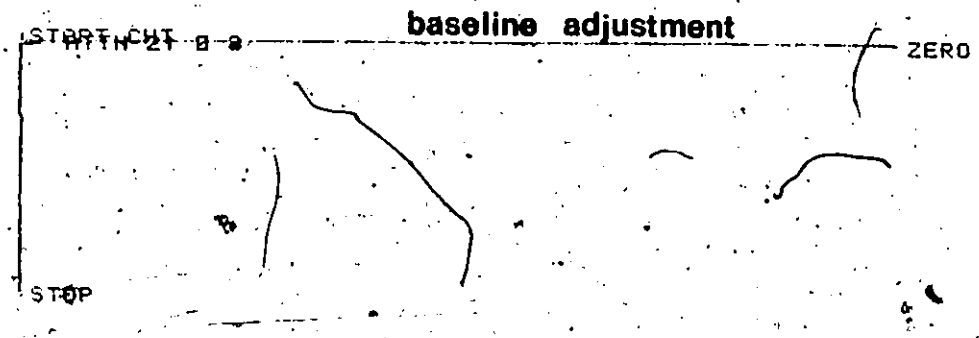

ATTN 2↑ 4
STOPT

Attenuation Change

030

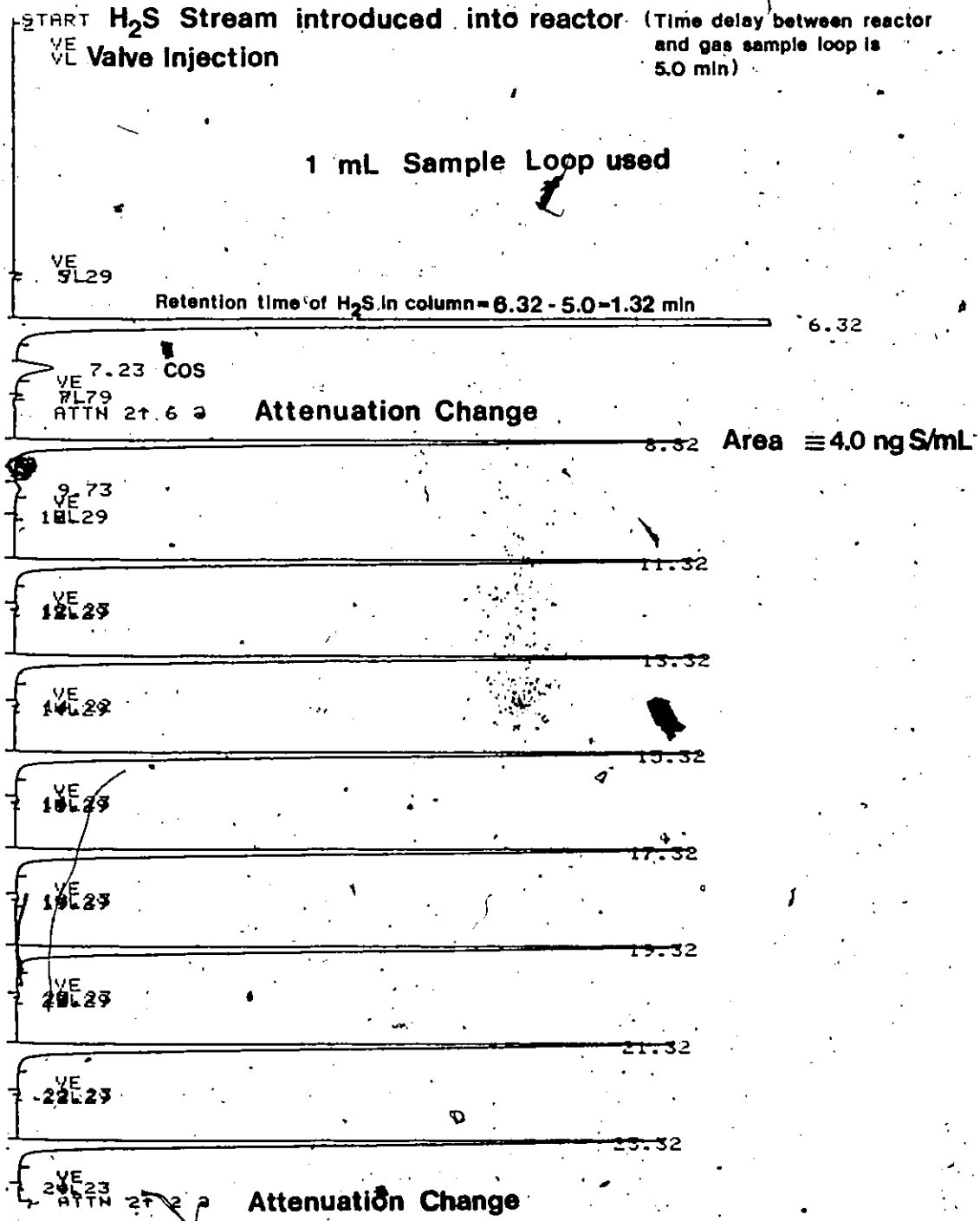
START H_2S Stream introduced into reactor
VE
VL Valve Injection
(Time delay between reactor and gas sample loop is 5.0 min)
1 mL Sample Loop used
VE
9L29
Retention time of H_2S in column = 6.32 - 5.0 = 1.32 min
6.32
7.23 COS
VE
7L79
ATTN 2↑ 6
Attenuation Change
8.32
Area ≡ 4.0 ng S/mL
9.73
VE
10L29
11.32
VE
12L29
13.32
VE
14L29
15.32
VE
16L29
17.32
VE
18L29
19.32
VE
20L29
21.32
VE
22L29
23.32
VE
24L23
ATTN 2↑ 2
Attenuation Change

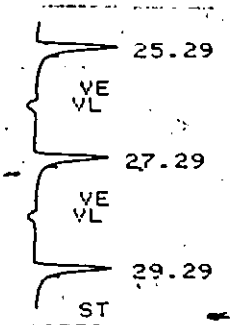

1/16 mL Sample Loop installed

031

Printout of Peak Areas

HP 5830A

RTIME	AREA	AR%
5.29	67	0.01
6.32	44410	9.75
7.23	1081	0.24
7.79	60	0.01
8.82	50260	11.03
9.73	548	0.12
10.29	59	0.01
11.32	51370	11.28
12.23	240	0.05
12.29	44	0.01
13.32	52190	11.46
14.22	264	0.06
14.29	51	0.01
15.32	51880	11.39
16.23	220	0.05
16.29	43	0.01
17.32	51280	11.26
18.23	180	0.04
18.29	35	0.01
19.32	50640	11.12
20.23	138	0.03
20.29	30	0.01
21.32	50050	10.99
22.23	125	0.03
22.29	33	0.01
23.32	49300	10.82
24.23	144	0.03
25.29	314	0.07
27.29	273	0.06
29.29	262	0.06

Printing Time (s)

132.4 s

Peak processor restarted

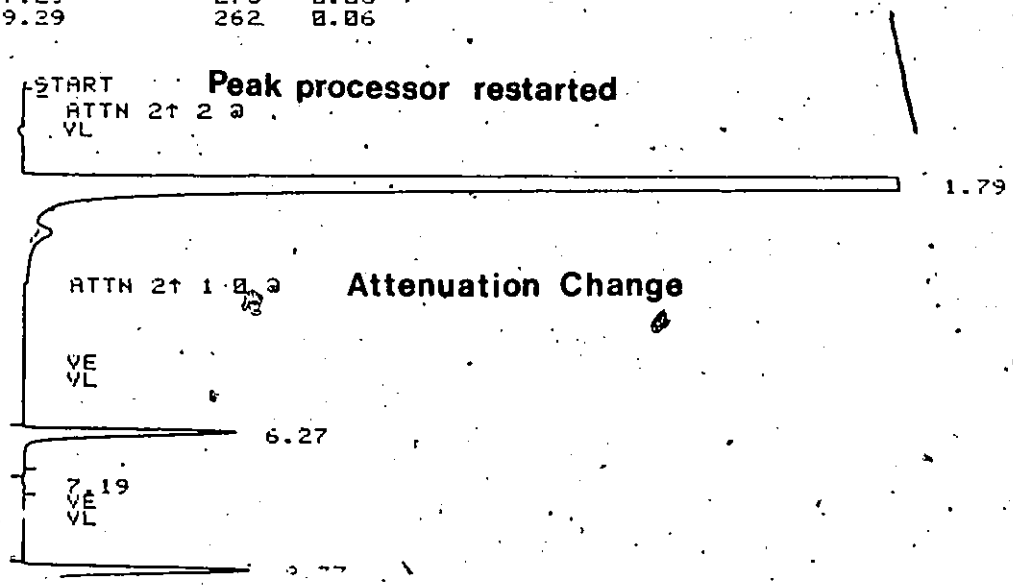

Attenuation Change

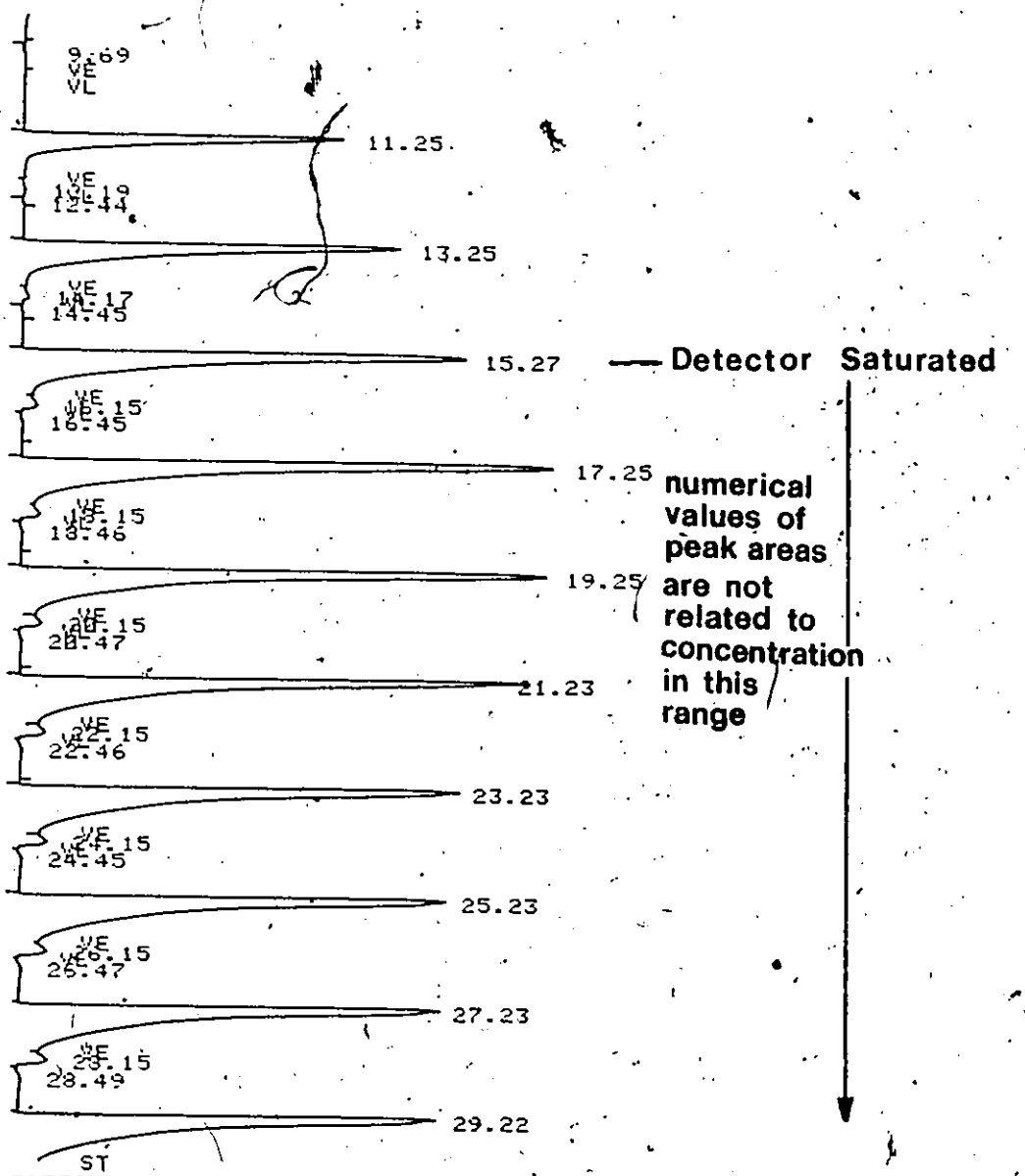

HP 5830A

PTIME	AREA	AR%
1.79	70980	0.60
6.27	271600	2.28
7.19	520	0.00
8.77	295400	2.48
9.69	1319	0.01
11.25	542200	4.55
12.19	3211	0.03
12.44	116	0.00
13.25	789200	6.62
14.17	12480	0.10
14.45	620	0.01
15.27	1083000	9.08
16.15	33810	0.28
16.45	3049	0.03

18.15	39630	0.33
18.46	4029	0.03
19.25	1245000	10.44
20.15	44060	0.37
20.47	5784	0.05
21.23	1214000	10.18
22.15	52520	0.44
22.46	7810	0.07
23.23	1176000	9.86
24.15	56320	0.47
24.45	12180	0.10
25.23	1180000	9.89
26.15	57500	0.48
26.47	13380	0.11
27.23	1184000	9.93
28.15	59820	0.50
28.49	14320	0.12
29.22	1187000	9.95

START

Feb 18/82

034

Nitrogen Flush after Desulfurization

1 mL Sample Loop

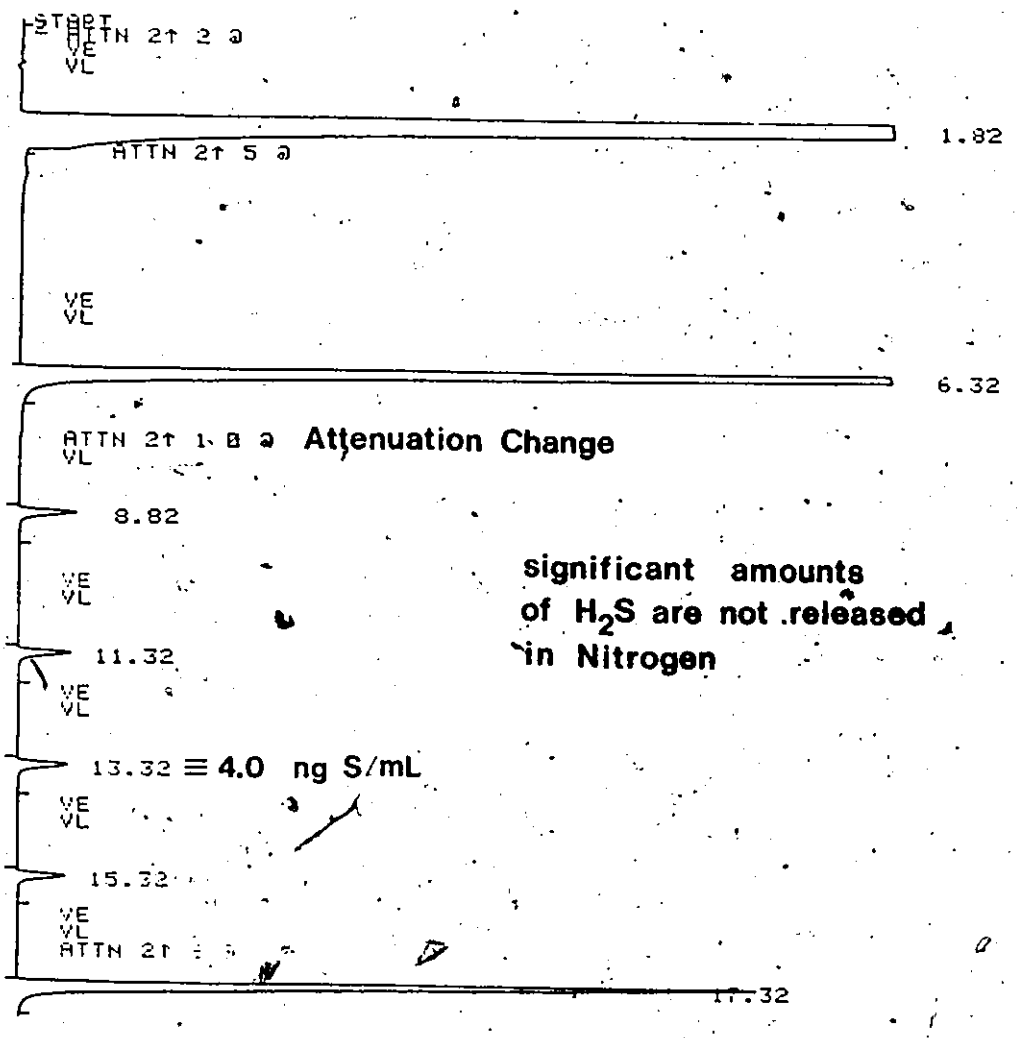

significant amounts of H_2S are not released in Nitrogen

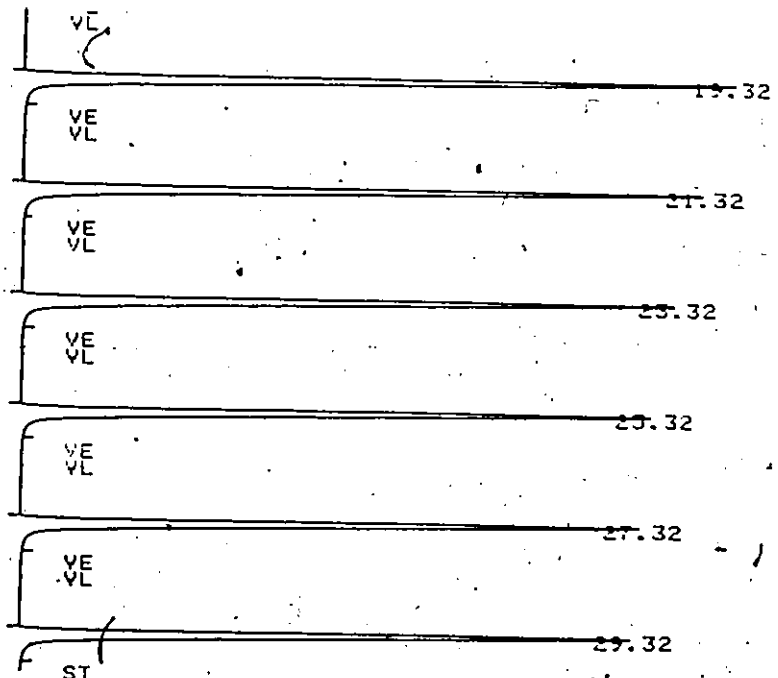

hp 5830A

RTIME	AREA	AR%
1.82	97960	13.75
6.32	71040	9.97
8.82	63810	8.96
11.32	59220	8.31
13.32	55660	7.81
15.32	53380	7.49
17.32	49790	6.99
19.32	47840	6.72
21.32	45600	6.40
23.32	43690	6.13
25.32	42100	5.91
27.32	41420	5.81
29.32	40830	5.73

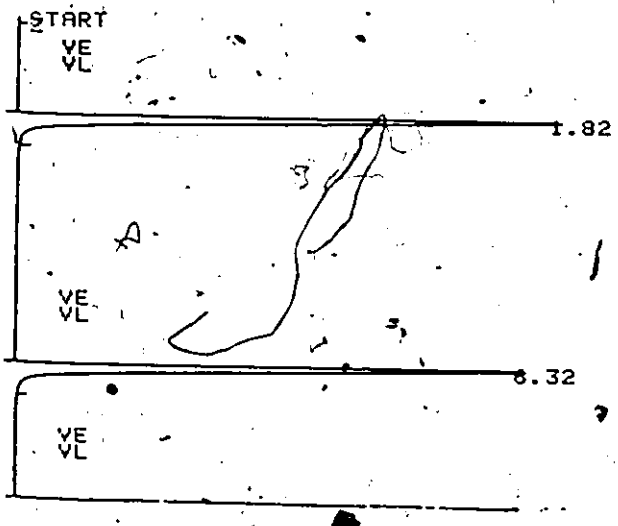

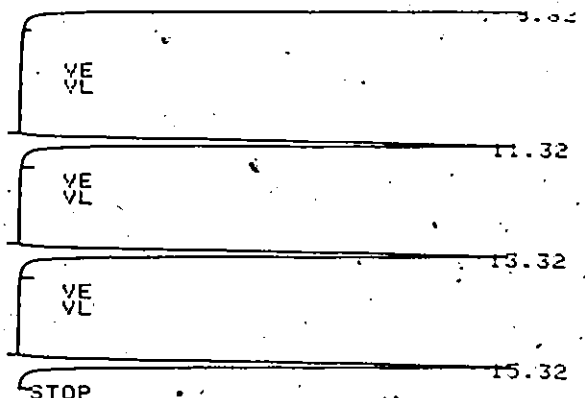

** 5830A

RTIME	AREA	AR%
1.82	35940	17.94
6.32	33600	16.77
8.82	33300	16.62
11.32	32730	16.34
13.32	32310	16.13
15.32	32470	16.21

Typical Regeneration
G.C. Trace

FEB 23 1982

095

```
TEMP1        70    70
TIME1        95.0
RATE          0.01
TEMP2        71
TIME2         0.2
INJ TEMP     70    70
FID TEMP    175   175
OVEN MAX    180

CHT SPD       1.00
ATTN 2↑       6
AUX SGNL      A
SLP SENS      0.10
AREA REJ      1
FLOW  A       0
FLOW  B      24
OPTN         11
  0.5   VLV/EXT        0
  0.8   VLV/EXT-       0
  2.5   VLV/EXT        0
  2.8   VLV/EXT-       0
  5.0   VLV/EXT        0
  5.3   VLV/EXT-       0
  7.5   VLV/EXT        0

  7.8   VLV/EXT-       0

 10.0   VLV/EXT        0
 10.3   VLV/EXT-       0
 12.5   VLV/EXT        0
 12.8   VLV/EXT-       0
 15.0   VLV/EXT        0
 15.3   VLV/EXT-       0
 17.5   VLV/EXT        0
 17.8   VLV/EXT-       0
 20.0   VLV/EXT        0
 20.3   VLV/EXT-       0
 22.5   VLV/EXT        0
 22.8   VLV/EXT-       0
 25.0   VLV/EXT        0
 25.3   VLV/EXT-       0
 27.5   VLV/EXT        0
 27.8   VLV/EXT-       0
 30.0   VLV/EXT        0
 30.3   VLV/EXT-       0
 32.5   VLV/EXT        0
 32.8   VLV/EXT-       0
 35.0   VLV/EXT        0
 35.3   VLV/EXT-       0
 37.5   STOP
```

g.c. and integrator settings

Regeneration in Air

valve injection program

START Air introduced into reactor

1/16 mL Sample Loop used

VE
VL
(Time delay between reactor and sample loop = 1.7 min)

1.34

ATTN 2↑ 8 0 Attenuation change and baseline adjustment

VE
VL

H_2S

3.34

ATTN 2↑ 4 0 Attenuation Change

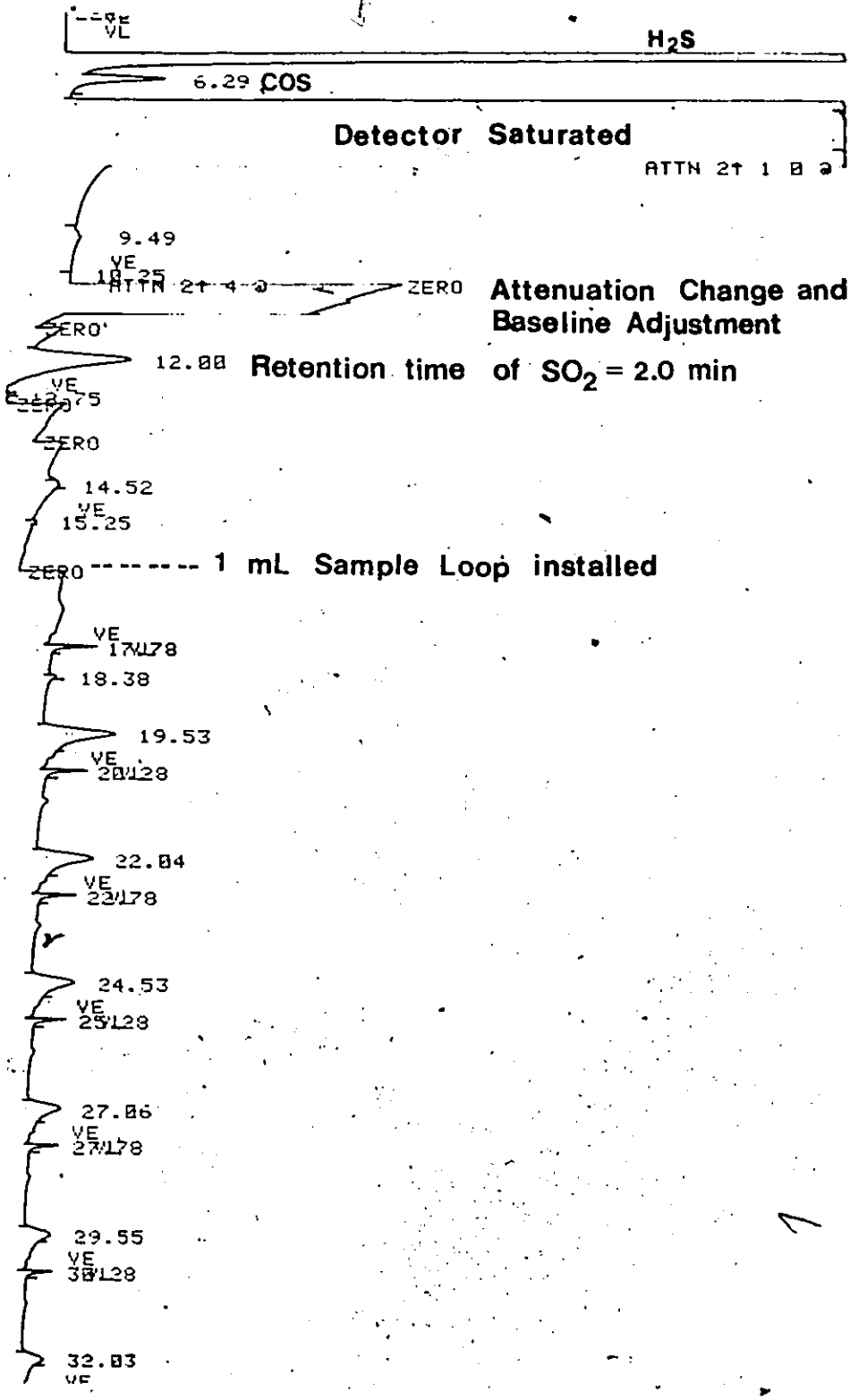

960.

Attenuation Change and Baseline Adjustment

Retention time of SO_2 = 2.0 min

1 mL Sample Loop installed

34.53
VE
35128

37.05
ST

HP 5830A

Printout of Peak Areas

RTIME	AREA	AR%
1.34	464	0.02
3.34	2050	0.08
5.83	124500	4.82
6.29	2273	0.09
6.81	495500	19.19
6.95	184800	7.16
7.07	1216000	47.10
7.75	450800	17.46
9.49	76140	2.95
10.25	12200	0.47
12.00	5650	0.22
12.75	63	0.00
14.52	171	0.01
15.25	47	0.00
17.78	479	0.02
18.38	65	0.00
19.53	2597	0.10
20.28	429	0.02
22.04	2070	0.08
22.78	370	0.01
24.53	1379	0.05
25.28	319	0.01
27.06	999	0.04
27.78	277	0.01
29.55	497	0.02
30.28	244	0.01
32.03	373	0.01
32.78	223	0.01
34.53	171	0.01
35.28	211	0.01
37.05	131	0.01

Detector Saturated

HP 5830A

Nitrogen Flush
After Regeneration

FEB 23 1982

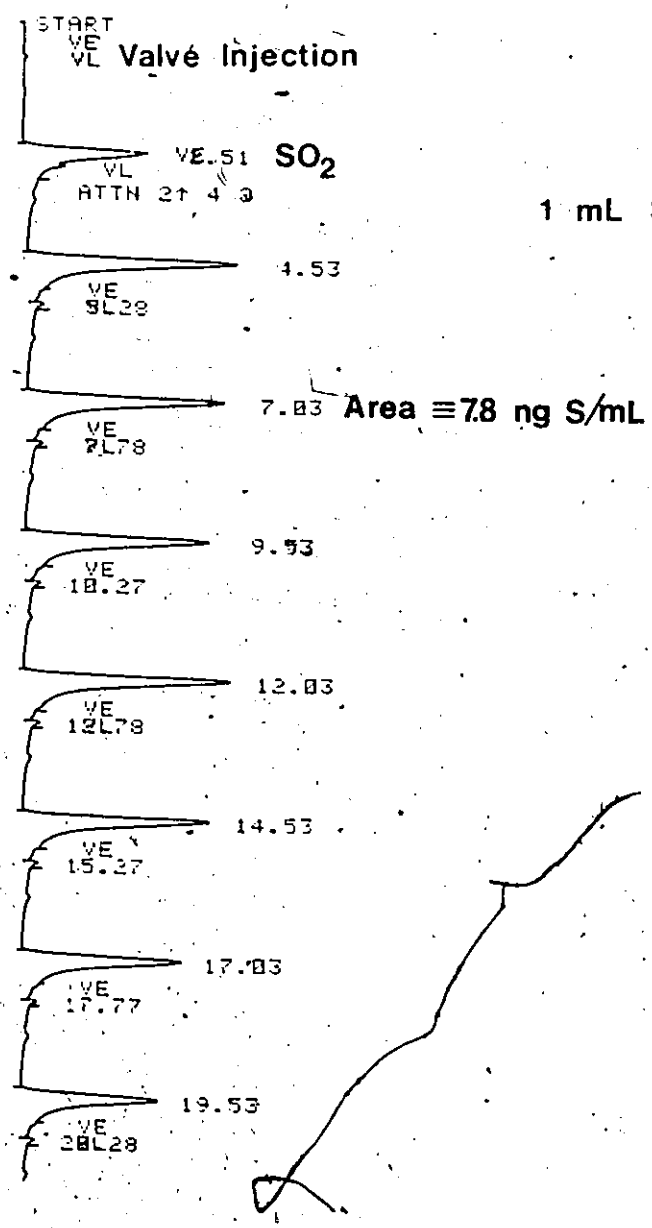

1 mL Sample Loop

Area ≡ 7.8 ng S/mL

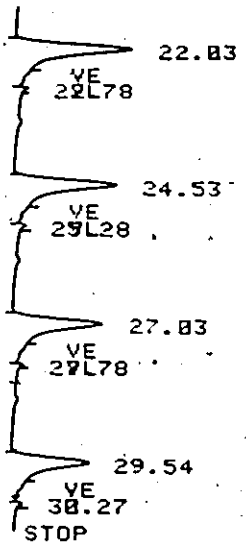

5830A

RTIME	AREA	AR%
2.51	4119	7.06
4.53	6552	11.23
5.28	89	0.15
7.83	6540	11.21
7.78	79	0.14
9.53	5809	9.96
10.27	82	0.14
12.83	6914	11.85
12.78	90	0.15
14.53	6037	10.35
15.27	88	0.15
17.83	5027	8.62
17.77	79	0.14
19.53	4364	7.48
20.28	85	0.15
22.83	3676	6.30
22.78	80	0.14
24.53	3323	5.70
25.28	76	0.13
27.83	2754	4.72
27.78	57	0.10
29.54	2349	4.03
30.27	62	0.11

Typical Reduction G.C. Trace
Regenerated Sorbent

Reduction Cycle

FEB 23 1982

100

g.c. and integrator settings

```
TEMP1        70    70
TIME1        95.0
RATE          8.01
TEMP2        71
TIME2         8.2
INJ TEMP     70    70
FID TEMP    175   175
OVEN MAX    180

CHT SPD       1.00
ATTN 2^       4
AUX SGNL      A
SLP SENS      0.10
AREA REJ      1
FLOW  A       8
FLOW  B      24
OPTN         11
```

1/16 mL Sample Loop

valve injection program

```
 0.5  VLV/EXT      0
 7.8  VLV/EXT-     0
      VLV/EXT      0
      VLV/EXT-     0
 2.0  VLV EXT      0
 2.3  VLV/EXT-     0
 5.5  VLV/EXT      0
 5.8  VLV/EXT-     0
10.0  VLV/EXT      0
10.3  VLV/EXT-     0
12.5  VLV/EXT      0
12.8  VLV/EXT-     0
15.0  VLV/EXT      0
15.3  VLV/EXT-     0
17.5  VLV/EXT      0
17.8  VLV/EXT-     0
20.0  VLV/EXT      0
20.3  VLV/EXT-     0
22.5  VLV/EXT      0
22.8  VLV/EXT-     0
25.0  VLV/EXT      0
25.3  VLV/EXT-     0
27.5  VLV/EXT      0
27.8  VLV/EXT-     0
30.0  VLV/EXT      0
30.3  VLV/EXT-     0
32.5  VLV/EXT      0
32.8  VLV/EXT-     0
35.0  VLV/EXT      0
35.3  VLV/EXT-     0
37.5  STOP
```

5.0% H_2 in nitrogen introduced to reactor

Valve Injection

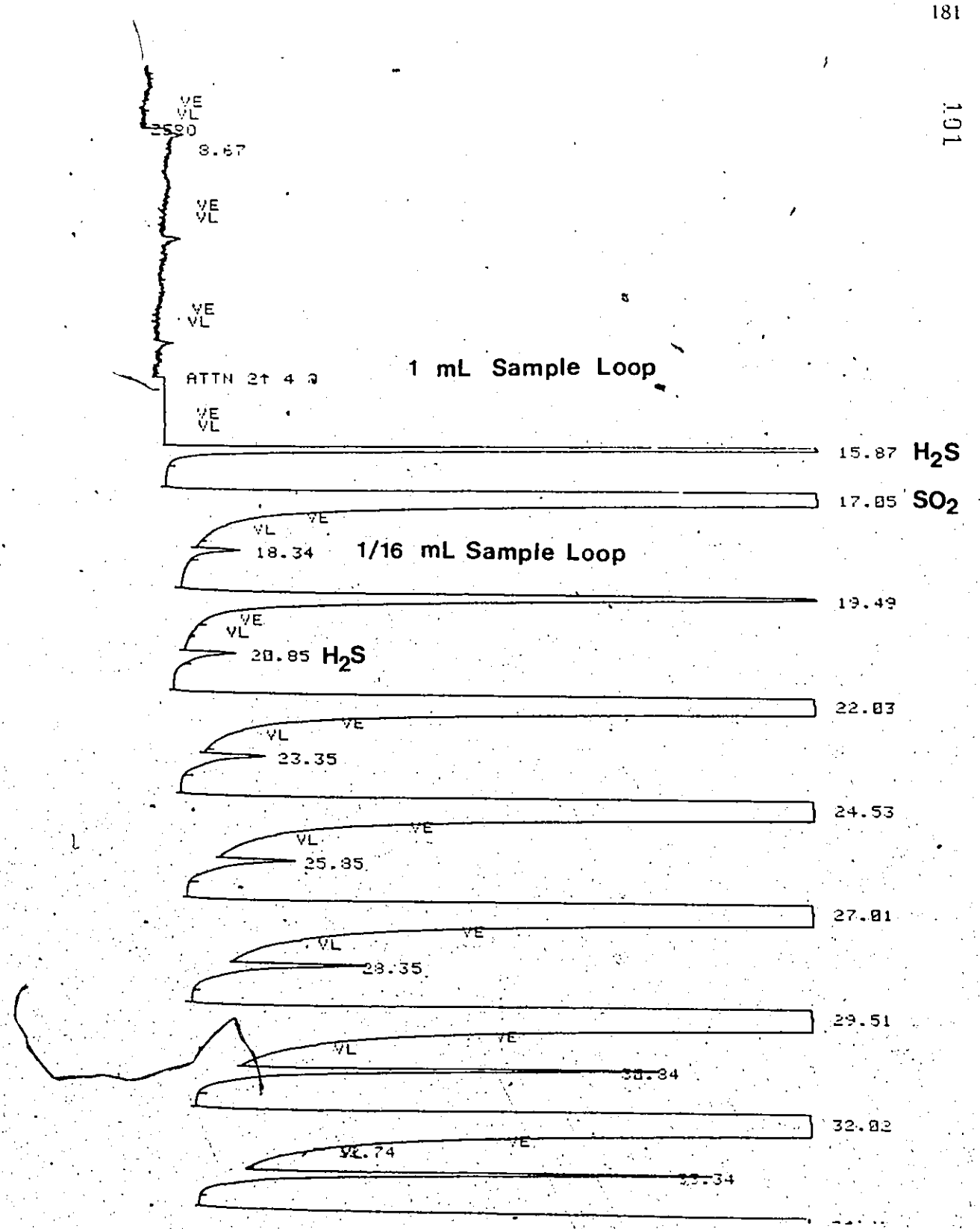
VE
VL
2580
8.67
VE
VL
VE
VL
ATTN 2↑ 4 3
1 mL Sample Loop
VE
VL
15.87 H_2S
17.85 SO_2
VL
VE
18.34
1/16 mL Sample Loop
19.49
VE
VL
20.85 H_2S
22.03
VL
VE
23.35
24.53
VL
VE
25.35
27.01
VL
VE
28.35
29.51
VL
VE
30.84
32.02
VL
VE
34.74
35.34

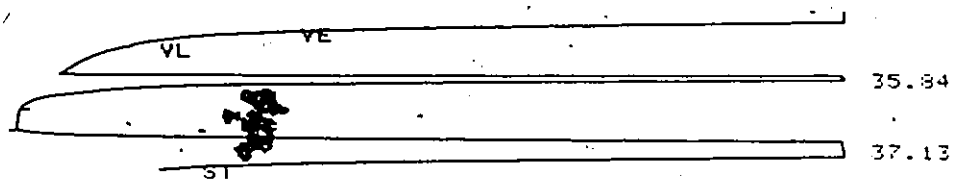

* 5830A

RTIME	AREA	AR%
15.87	26520	1.12
17.05	204500	8.66
18.34	920	0.04
19.49	28000	1.19
20.85	1279	0.05
22.03	190600	8.07
23.35	1782	0.08
24.53	316800	13.41
25.85	4030	0.17
27.01	396900	16.81
28.35	5876	0.25
29.51	442900	18.75
30.84	11740	0.50
32.02	428900	18.16
32.74	3515	0.15
33.34	9796	0.41
34.57	195600	8.28
35.84	25680	1.09
37.13	66320	2.81

Printing Time (s)

~ in 25.2 s

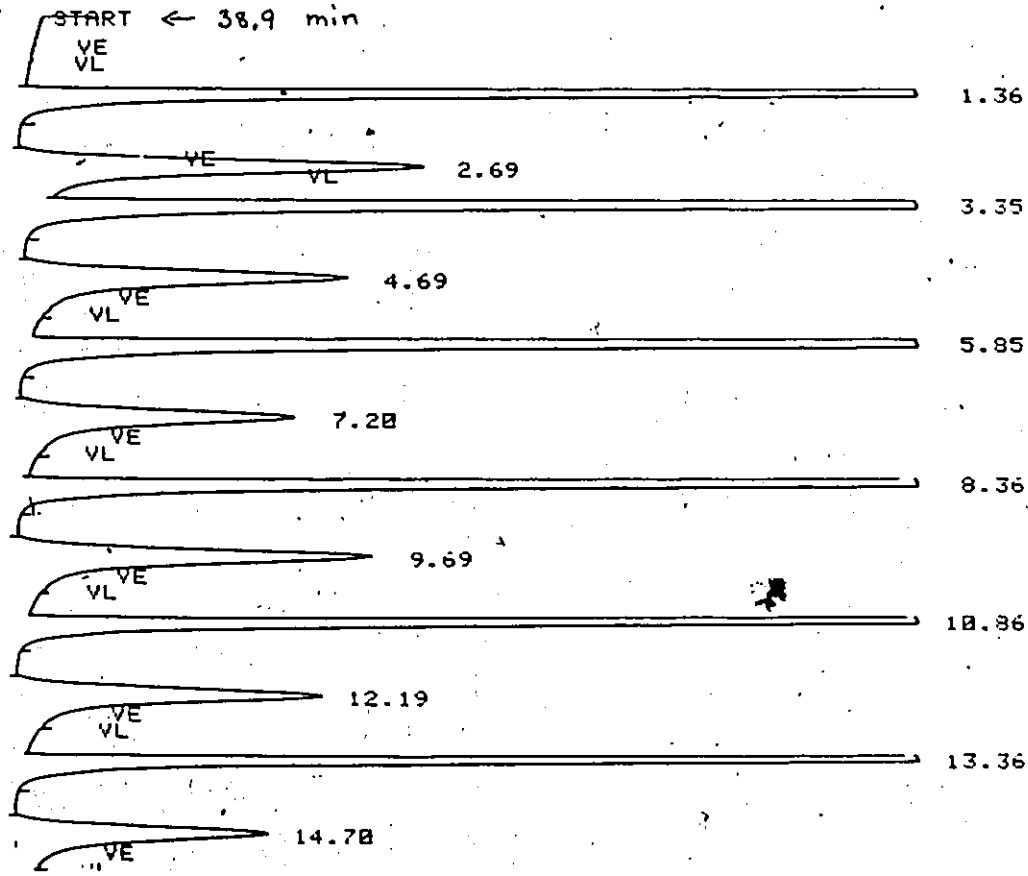

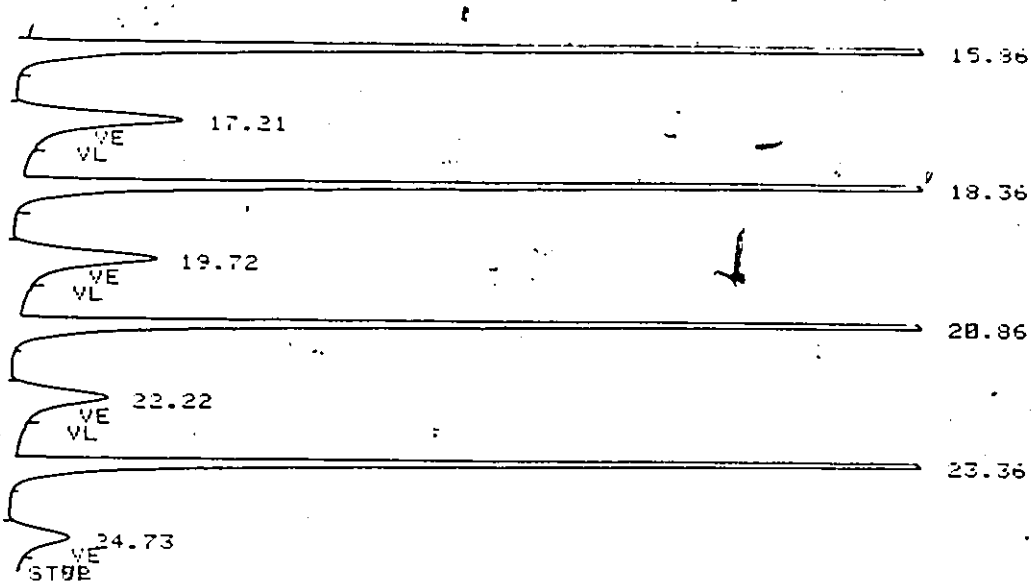

** 5830A

RTIME	AREA	AR%
1.36	61140	9.64
2.69	19150	3.02
3.35	84600	13.34
4.69	15030	2.37
5.85	94040	14.83
7.20	12620	1.99
8.36	77080	12.15
9.69	15740	2.48
10.96	49250	7.76
12.19	13330	2.10
13.36	40550	6.39
14.70	11240	1.77
15.86	35490	5.59
17.21	7410	1.17
18.36	31130	4.91
19.72	6235	0.98
20.86	28570	4.50
22.22	4086	0.64
23.36	25270	3.98
24.73	2361	0.37

```
DELETE TIME TBL
VLV/EXT 0 MIN? . 5 @
VLV/EXT 0 - MIN? . 8 @
VLV/EXT 0 MIN? 5 . 0 @
VLV/EXT 0 - MIN? 5 . 3 @
VLV/EXT 0 MIN? 1 0 . 0 @
VLV/EXT 0 - MIN? 1 0 . 3 @
VLV/EXT 0 MIN? 1 5 . 0 @
VLV/EXT 0 - MIN? 1 5 . 3 @
VLV/EXT 0 MIN? 2 0 . 0 @
VLV/EXT 0 - MIN? 2 0 . 3 @
VLV/EXT 0 MIN? 2 5 . 0 @
VLV/EXT 0 - MIN? 2 5 . 3 @
VLV/EXT 0 MIN? 3 0 . 0 @
VLV/EXT 0 - MIN? 3 0 . 3 @
VLV/EXT 0 MIN? 3 5 . 0 @
VLV/EXT 0 - MIN? 3 5 . 3 @
VLV/EXT 0 MIN? 4 0 . 0 @
VLV/EXT 0 - MIN? 4 0 . 3 @
VLV/EXT 0 MIN? 4 5 . 0 @
```

Valve V-5 injection timetable is reprogrammed

104

```
VLV/EXT 0 MIN? 5 0 . 0 0
VLV/EXT 0 - MIN? 5 0 . 3 0
VLV/EXT 0 MIN? 5 5 . 0 0
VLV/EXT 0 - MIN? 5 5 . 3 0
STOP MIN? 6 0 . 0 0

  0.5  VLV/EXT      0
  0.8  VLV/EXT-     0
  5.0  VLV/EXT      0
  5.3  VLV/EXT-     0
 10.0  VLV/EXT      0
 10.3  VLV/EXT-     0
 15.0  VLV/EXT      0
 15.3  VLV/EXT-     0
 20.0  VLV/EXT      0
 20.3  VLV/EXT-     0
 25.0  VLV/EXT      0
 25.3  VLV/EXT-     0
 30.0  VLV/EXT      0
 30.3  VLV/EXT-     0
 35.0  VLV/EXT      0
 35.3  VLV/EXT-     0
 40.0  VLV/EXT      0
 40.3  VLV/EXT-     0
 45.0  VLV/EXT      0
 45.3  VLV/EXT-     0
 50.0  VLV/EXT      0
 50.3  VLV/EXT-     0
 55.0  VLV/EXT      0
 55.3  VLV/EXT-     0
 60.0  STOP
```

ff 5 min 40.4 sec

```
CHT SPD . 5 0
```

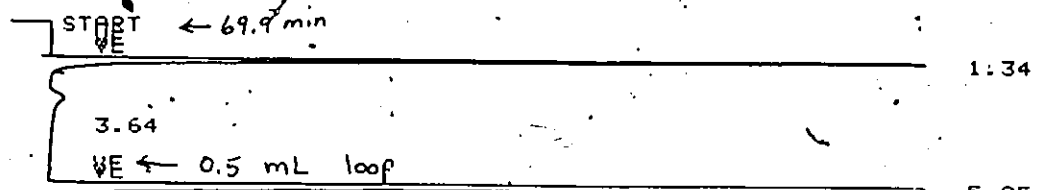

9.18 + 69.9 = 79.08 min.

```
* 5830A
 RTIME        AREA     AR%
  1.34       17800    8.76
  5.85      185300   91.24
```

off for 30 sec.

```
CHT SPD . 2 5 0
 CHT SPD      0.25
```

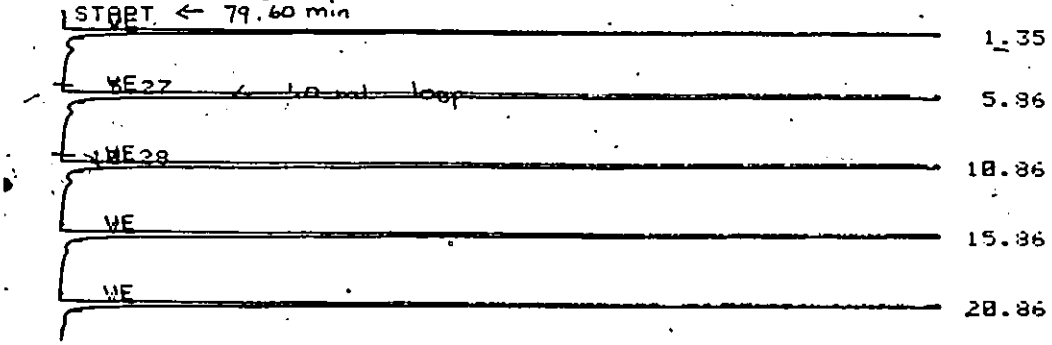

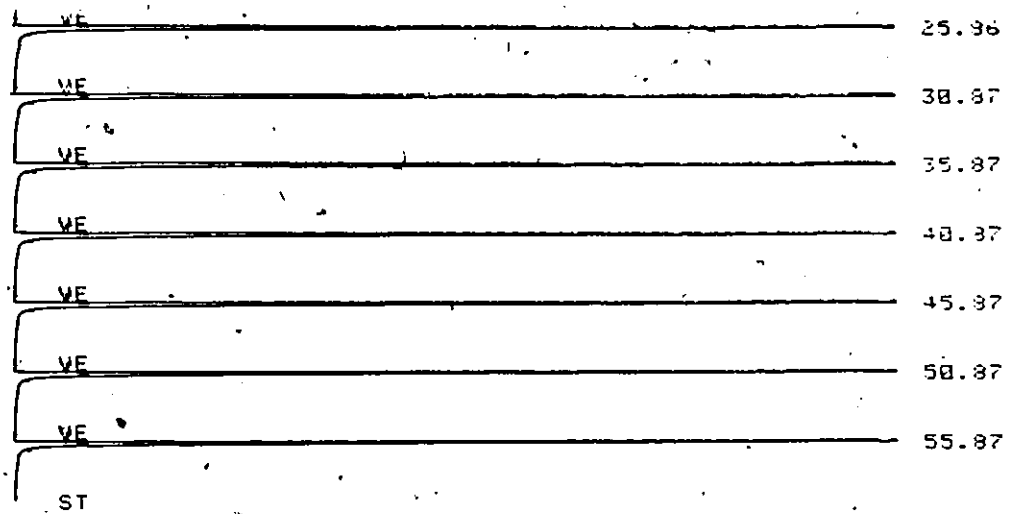

105

ST
5830A

RTIME	AREA	AR%
1.35	173900	6.85
5.27	26	0.00
5.86	293500	11.56
10.28	22	0.00
10.86	277700	10.94
15.86	259200	10.21
20.86	242100	9.53
25.86	225800	8.89
30.87	210800	8.30
35.87	196700	7.75
40.87	183400	7.22
45.87	168700	6.64
50.87	158100	6.23
55.87	149500	5.89

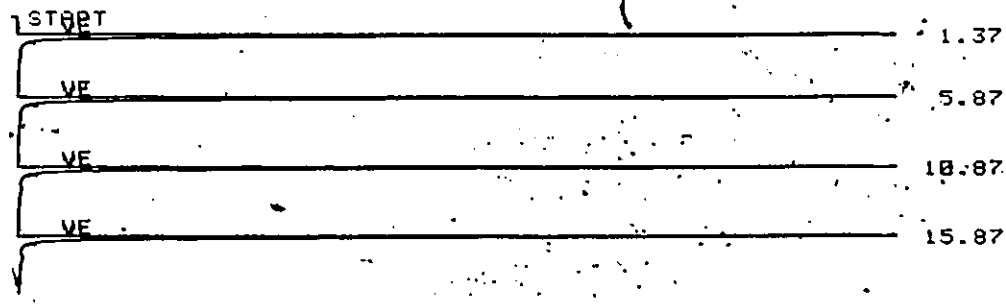

APPENDIX 11

Calculation of β'k, D_f and Adsorption Capacity

Calculation of β'k Values

In section 6.2.1.5, it was shown that:

$$\beta' k = \left(\frac{d\theta}{dt} \right) \frac{v_o}{X(1 - \varepsilon_v)y_b} \qquad 6.2.1.1$$

where

$$\theta = C/C_o$$

$$t = \frac{t^*}{y_b} = \frac{C_o t v_o}{\rho_s(1 - \varepsilon_v)y_b} \qquad 4.12, 4.5a, 4.6a$$

$$\rho_s = \rho_s(1 - \varepsilon_p)$$

Substituting for t and ρ_s in equation 6.2.1.1, the equation reduces to:

$$\beta' k = \left(\frac{d\theta}{dt} \right) \frac{\rho_s(1 - \varepsilon_p)}{C_o X} \qquad 6.2.1.2$$

The values of $(d\theta/dt)$ were determined by linear regression using the data points given in Table A11.1. Refer to Figure 6.16 for breakthrough curves.

Table A11.1: Data for Breakthrough Curves Illustrated in Figure 6.16

Run #12

t (min)	C/C_o
30.6	0.0009
32.6	0.0244
36.6	0.0889
40.6	0.1244

slope = 0.01276

Correlation coefficient = 0.9926

Run #16

t (min)	C/C_o
39.0	0.0009
41.0	0.0151
43.0	0.0489
45.0	0.0756
47.0	0.0844
49.0	0.1111

slope = 0.01138

Correlation coefficient = 0.9844

Run #17

t (min)	C/C_o
36.1	0.0009
38.1	0.0613
40.1	0.1368
42.1	0.2311

slope = 0.03831

Correlation coefficient = 0.9951

Run #18

t (min)	C/C_o
17.7	0.0009
19.7	0.0670
21.7	0.1451
23.7	0.2232

slope = 0.03725

Correlation coefficient = 0.9992

Thus, for run 12, the values of $\varepsilon_p = 0.28$, $C_o = 1.00 \times 10^{-7}$ moles H_2S/mL, $\rho'_s = (7.2\ g/cm^3)/(170.3\ g/mol\ CeO_x)$, $(d\theta/dt) = (0.01267\ min^{-1})/(60\ s/min)$ are substituted into equation 6.2.1.2.

Calculation of Adsorption Capacity

The breakthrough time can be defined at any convenient value. For this study, the breakthrough time was chosen to be the time corresponding to an exit H_2S concentration of 200 ng S/mL (150 ppm) since EPA standards require source concentrations to be less than this value. Since the breakthrough curves were very steep, the adsorption capacity, as g H_2S/g CeO_2, can be approximated by the expression:

$$A = \frac{\dot{Q}\, C_o\, t_{C=200}\, (MW\ H_2S)}{\text{wt. of fixed bed}} \qquad A11.1$$

Calculation of Molecular Diffusivity

For a multicomponent mixture, the H_2S diffusivity is given by

$$D_{H_2S-m} = \frac{1 - y_{H_2S}}{\left(\frac{y_{H_2}}{D_{H_2-H_2S}}\right) + \left(\frac{y_{CO}}{D_{CO-H_2S}}\right) + \left(\frac{y_{CO_2}}{D_{CO_2-H_2S}}\right) + \left(\frac{y_{H_2O}}{D_{H_2O-H_2S}}\right)} \qquad A11.2$$

where y is the mole fraction of a component and the binary coefficients are given by

$$D_{AB} = \frac{BT^{3/2}\left|\left(\frac{1}{M_A}\right)+\left(\frac{1}{M_B}\right)\right|^{1/2}}{P\, r_{AB}\, I_D} \qquad \text{A11.3}$$

$$B = \left(10.85 - 2.50\left(\frac{1}{M_A}\right)+\left(\frac{1}{M_B}\right)^{1/2}\right) \times 10^{-4} \qquad \text{A11.4}$$

$r_{AB} = \frac{r_A + r_B}{2}$ = collision diameter in A (tabulated in reference 26)

M_A, M_B = molecular weights of A or B

P = pressure in atm

T = absolute temperature, K

I_D = collision integral obtained from correlations of $\left(\frac{\varepsilon}{k}\right)_{AB}$ (graphs available in reference 26)

where

$$\left(\frac{\varepsilon}{k}\right)_{AB} = \sqrt{\left(\frac{\varepsilon}{k}\right)_A \left(\frac{\varepsilon}{k}\right)_B}$$

and

$\left(\frac{\varepsilon}{k}\right)_A$ is a characteristic number for a given component and is obtained from standard tables (26).

If (ε/k) is unknown, estimates can be obtained from

$$\left(\frac{\varepsilon}{k}\right) = 0.77\, T_c = 1.15\, T_b = 1.92\, T_m \qquad \text{A11.5}$$

where

T_c = critical temp., K

T_b = boiling temp., K

T_m = melting temp., K

The diffusivity was used to calculate the Peclet number $Pe = v_o d_p / D_L$

APPENDIX 12

Constant-Pattern Solution for the Grain Model

(taken from reference 80)

In the constant pattern case, the shape of the reaction front (X versus y^*, as in Figure A 12.1) is unchanging as it moves through the bed. Therefore, the slope of the reaction front at any given extent of reaction is independent of time, and is only a function of the particular value of X:

$$\left(\frac{\partial X}{\partial y^*}\right)_{t^*} = \frac{dX}{dy^*} = f_1(X) \qquad A12.1$$

Furthermore, all parts of the reaction front must move through the bed at the same constant velocity u:

$$\left(\frac{\partial y^*}{\partial t^*}\right)_X = u \text{ (independent of } X, t^*) \qquad A12.2$$

When the leading edge of the reaction front reaches the end of the bed (dimensionless length y_b^*), breakthrough commences. The shape of the breakthrough curve, $\theta = f_2(t^*)$, can be calculated when all of the following have been determined:

1) the shape of the reaction front, $f_1(X)$ (equation A12.1)

2) the velocity of the reaction front, u (equation A12.2)

3) the relationship between 0 and X

Using the chain rule and the constant-velocity condition (equation A12.2) yields:

$$\left(\frac{\partial X}{\partial t^*}\right)_{y^*} = -\left(\frac{\partial y^*}{\partial t^*}\right)_X \cdot \left(\frac{\partial X}{\partial y^*}\right)_{t^*} = -u\left(\frac{\partial X}{\partial y}\right)_{t^*} \qquad A12.3$$

The differential mass balance equation for a fixed-bed reactor (see Chapter IV) is:

$$\left(\frac{\partial \theta}{\partial y^*}\right)_{t^*} = \frac{dX}{dt^*} = \theta\beta \qquad 4.3$$

Combining equations A12.3 and 4.3 gives the following relationship between 0 and X.

$$\left(\frac{\partial 0}{\partial y^*}\right)_{t^*} = u\left(\frac{\partial X}{\partial y^*}\right)_{t^*} \qquad \text{A12.4}$$

This can be integrated with the boundary condition

$$X = 1 \text{ and } 0 = 1 \text{ at } y^* = 0, t^* > 0$$

$$0 - 1 = u(X - 1) \qquad \text{A12.5}$$

Since X and 0 have the same limits (0 to 1)

$$u = 1 \qquad \text{A12.6}$$

$$0 = X \qquad \text{A12.7}$$

Now the shape of the reaction front, $f_1(X)$ can be determined from equations A12.3 and 4.3:

$$f_1(X) = -\frac{\partial X}{\partial y^*} = -\frac{1}{u}\left(\frac{dX}{dt^*}\right) = -\frac{1}{u}(0\beta) = -\beta X \qquad \text{A12.8}$$

The shape of the breakthrough curve (0 versus t^*) is defined by the following equation:

$$\frac{d0}{dt^*} = \frac{dX}{dt^*} = \beta 0 = \beta X \qquad \text{A12.9}$$

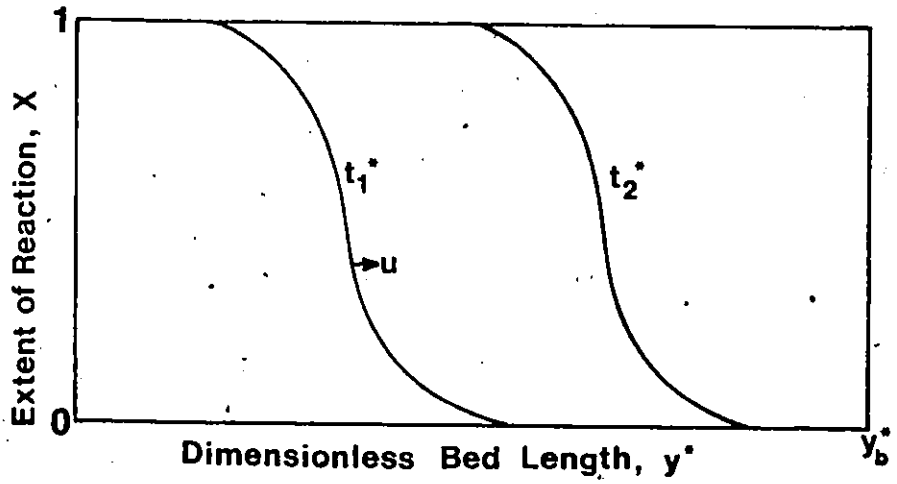

Figure A12.1 Constant Pattern Reaction Front

APPENDIX 13

Grain Model Equations

The following example is given for a spherical pellet consisting of spherical grains (refer to Figure A13.1)

Kinetic Equations for the Grains

Within the porous pellet, each grain reacts according to the shrinking core model. It is assumed that the reacted layer surrounding each grain represents no diffusional resistanee. Thus, the rate of reaction per unit surface area of unreacted core, for a first order reaction, is given by:

$$-\frac{1}{4\pi r_c^2}\frac{dN_B}{dt} = \frac{-b}{4\pi r_c^2}\frac{dN_A}{dt} = b\,k\,C_A \qquad A13.1$$

where r = length coordinate for the grain

r_g = radius of grain

r_c = radius to the reaction interface in grain

b = stoichiometric coefficient associated with solid reactant B (refer to eqn. 4.1)

N_B = number of moles of B, the solid reactant

N_A = number of moles of A, the gaseous reactant

k = first order intrinsic chemical rate constant for the surface reaction in the grain

C_A = gaseous concentration of A at the reaction interface

t = time.

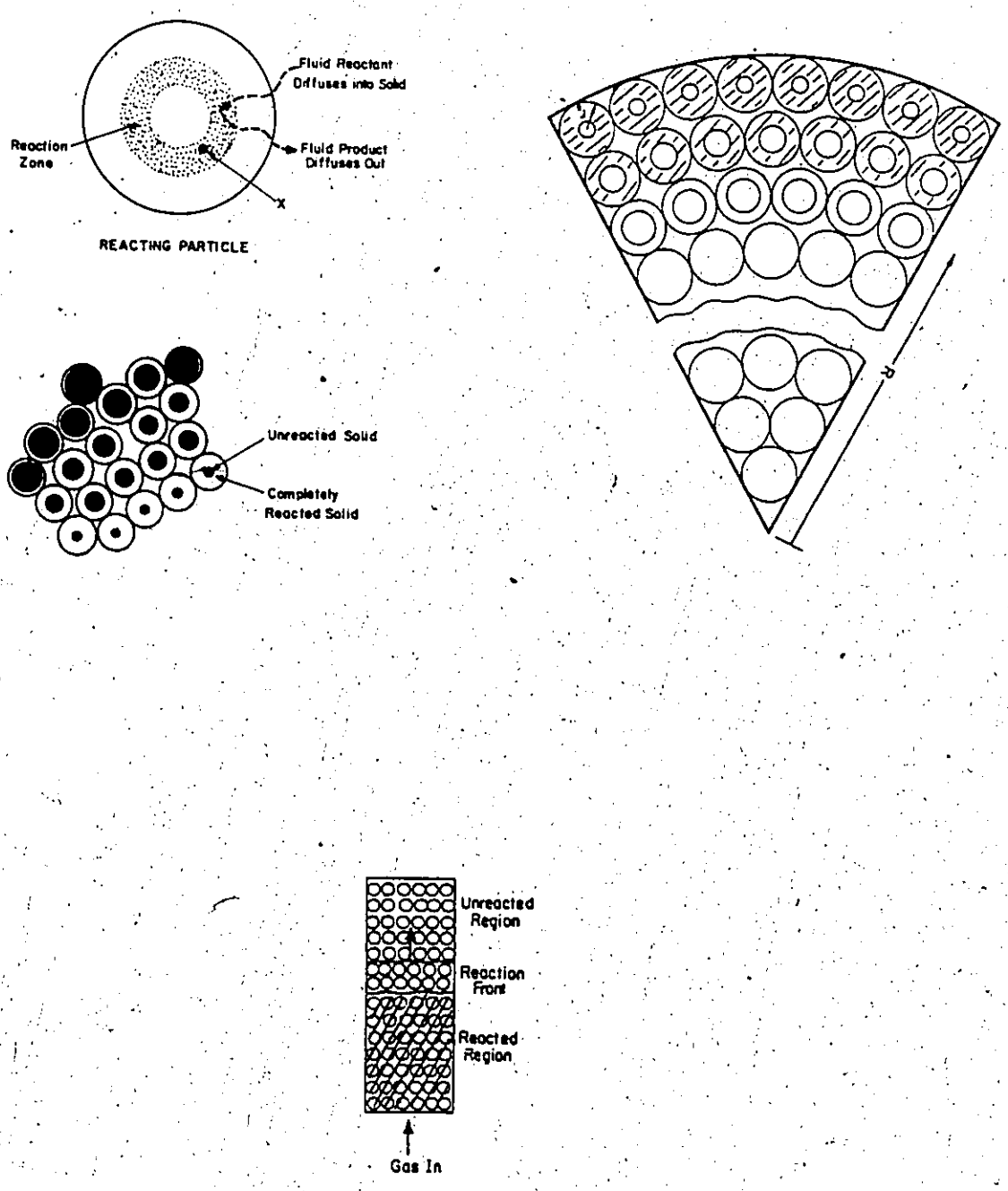

Figure A13.1: Schematic diagrams of a spherical grain, a spherical pellet consisting of spherical grains, and a fixed bed reactor.

Since the reaction is not diffusion limited, the concentration of A at the reaction interface, C_A, is equal to the gaseous concentration at the grain surface i.e. C_A is constant from $r = r_g$ to $r = r_c$. In terms of the shrinking radius, the moles of solid reactant, B, is given by:

$$-d(N_B) = -b\,d(N_A) = -\rho_s\,d(V) = -\rho_s\,d\left(\frac{4}{3}\pi r_c^3\right) = -4\pi\rho_s r_c^2\,d r_c \qquad A13.2$$

Thus, equation A13.1 becomes

$$\frac{d r_c}{dt} = -\frac{b k}{\rho_s} C_A \qquad A13.3$$

where ρ_s = true molar density of the solid.

The initial condition is:

$$\text{at } t=0, \quad r_c = r_g \text{ for all R} \qquad A13.4$$

R = length coordinate of the pellet.

At any time after reaction commences, the concentration at the surface of the grain is a function of radial position within the pellet,

$$\text{i.e. for } t>0, \quad C_A = C_A(R) \quad \text{at } r = r_g \text{ (to } r = r_c) \qquad A13.5$$

Kinetic Equations for a Single Pellet

The differential mass balance equation 4.2 (see chapter 4) is applicable. The following assumptions are made:

(a) The system is quasi-steady state.

(2) Bulk flow within the porous matrix is negligible.

Thus, equation 4.2 becomes:

$$D_e \nabla^2 C_A - R_A = 0 \qquad A13.6$$

where D_e = effective diffusivity of gaseous reactant in the porous matrix.

R_A = local rate of consumption of A (a function of position in pellet)

For a spherical pellet equation A13.6 becomes

$$\frac{D_e}{R^2}\frac{\partial}{\partial R}\left(R^2\frac{\partial C_A}{\partial R}\right) - R_A = 0 \qquad \text{A13.7}$$

The relationship between the local consumption of A and the local rate of reaction for grains of any shape, is given by:

$$R_A = (1-\varepsilon_p)\, k\, C_A \frac{A_g}{V_g}\left(\frac{A_g r_c}{V_g F_g}\right)^{F_g - 1} \qquad \text{A13.8}$$

where ε_p = pellet porosity

A_g = external surface area of grain

V_g = volume of grain

F_g = shape factor of the grain

For spherical grains, $F_g = 3$ and $F_g V_g / A_g = r_g$. To obtain the solution for the concentration profile in a single pellet, equation A13.7 together with equation A13.8 are integrated numerically over the radius of the pellet (see reference 74). The boundary conditions require that the concentration profile is a continuous function i.e.

$$\frac{\partial C_A}{\partial R} = 0 \quad \text{at } R = 0 \qquad \text{A13.9}$$

and that the reactant concentration is maintained at C_{A_0} at the outer surface of the pellet (since it was assumed that external mass transfer is negligible).

$$C_A = C_{A_0} \quad \text{at } R = R_p \quad t > 0 \qquad \text{A13.10}$$

The initial condition requires

$$C_A = C_{A_0} \quad \text{at } t = 0 \quad \text{for } R = R_p \qquad \text{A13.11}$$

Equation A13.6 can be rewritten in dimensionless form:

$$\nabla^{*2}\psi - \sigma^2 \psi \xi^{F_g - 1} = 0 \qquad \text{A13.12}$$

where

$$\psi = \frac{C_A}{C_{A_0}} \qquad = \text{dimensionless concentration within the pellet}$$

$$\xi = \frac{A_g r_c}{F_g V_g}$$ = dimensionless position of reaction front in the grain

and

$$\hat{\theta} = \frac{F_p V_p}{A_p} \sqrt{\frac{(1-\varepsilon_p) k A_g}{D_e V_g}} \qquad A13.13$$

F_p = shape factor for the pellet

V_p = volume of pellet

A_p = external surface area of the pellet.

$\hat{\theta}$ is a parameter which has a role akin to that of the Thiele modulus in heterogeneous catalysis. The length coordinate of the operator is defined as η, where

$$\eta = \frac{A_p R}{F_p V_p}$$

The rate of reaction within an individual grain in the pellet is given by:

$$\frac{d\xi}{dt^*} = -\psi \qquad A13.14$$

where

$$t^* = \left(\frac{b k C_{A_0}}{\rho_s} \frac{A_g}{F_g V_g} \right) t$$ = dimensionless time

The overall extent of reaction X, is given by:

$$X = \frac{\int_0^1 \eta^{F_p - 1} (1 - \xi^{F_g}) d\eta}{\int_0^1 \eta^{(F_p - 1)} d\eta} \qquad A13.15$$

Kinetic Equations for the Fixed Bed

A schematic diagram of the reactor is given in Figure A13.1. Three additional dimensionless variables need to be defined:

$$\theta = \frac{C_{A_0}}{\overline{C}_{A_0}}$$ = dimensionless gaseous concentration external to the pellet

where

C_{A_0} = external concentration of A at position y in bed

$\bar{C}_{A_0}$ = concentration of A at reactor inlet
= C_0 in Chapter 4

$\kappa = \frac{k}{\bar{k}}$ = rate constant which is a function of position of bed

where

k = local rate of chemical reaction

$\bar{k}$ = rate of reaction at reactor inlet

Redefine the dimensionless time as

$$t^* = \left(\frac{b\, \bar{k}\, \bar{C}_{A_0}\, A_g}{\rho_s F_g V_g} \right) t \qquad \text{A13.16}$$

Then the rate of reaction of an individual grain in the pellet is given by

$$\frac{\partial \xi}{\partial t^*} = \frac{k}{\bar{k}} \frac{C_{A_0}}{\bar{C}_{A_0}} \frac{C_A}{C_{A_0}} \qquad \text{A13.17}$$

$$= \kappa\, \theta\, \psi$$

The overall rate of the pellet is given by

$$\frac{dX}{dt^*} = \frac{d}{dt^*} \left(\frac{\int_0^1 \eta^{F_p - 1} (1 - \xi^{F_g})\, d\eta}{\int_0^1 \eta^{(F_p - 1)}\, d\eta} \right)$$

$$= \frac{\int_0^1 \eta^{F_p - 1} F_g \xi^{F_g} \psi\, d\eta}{\int_0^1 \eta^{F_p - 1}\, d\eta} \qquad \text{A13.18}$$

which becomes

$$\frac{\partial X}{\partial t^*} = \kappa \theta\, \beta \qquad \text{A13.19}$$

β is the effectiveness factor and depends on 0 and κ through the dependence of X on 0 and κ. For a fixed $\hat{\sigma}$ and X, β will be the same.

Gas flow through the bed will be assumed to be plug flow. The additional assumptions are:

(1) The bed is of constant cross section.

(2) Pellet properties are uniform along the bed.

(3) The dispersive and diffusive mass transport in the direction of flow is negligible.

(4) Mass transfer between the gas and the external surface of the pellet represents a negligible resistance.

(5) The quasi-steady state assumption is applicable.

(6) One mole of gaseous reactant yields one mole of gaseous product.

Thus the material balance on the gaseous reactant yields:

$$-v_o \frac{\partial \theta}{\partial y} = \frac{(1-\varepsilon_p)(1-\varepsilon_v)}{b} \rho_s \frac{\partial X}{\partial t} \qquad \text{A13.20}$$

If a dimensionless position is defined as

$$y^* = \frac{\bar{k} A_g \bar{C}_{A_o}}{v_o F_g V_g} (1-\varepsilon_p)(1-\varepsilon_v) y$$

Equation A13.20 becomes

$$\frac{\partial \theta}{\partial y^*} = \frac{\partial X}{\partial t^*} = \kappa \theta \beta \qquad \text{A13.21}$$

$\kappa\beta \equiv \beta$ In Chapter 4